UNIVERSITÉ CATHOLIQUE DE LOUVAIN
Faculté des Sciences Appliquées
CERMIN

Experimental study of 2D hole systems: coherent transport in quantum dots and magnetothermopower

Dissertation présentée en vue de l'obtention du grade de
Docteur en Sciences Appliquées
par

Sébastien Faniel

Promoteur:
Prof. Vincent Bayot

Décembre 2007

UNIVERSITÉ CATHOLIQUE DE LOUVAIN
Faculté des Sciences Appliquées
CERMIN

Experimental study of 2D hole systems: coherent transport in quantum dots and magnetothermopower

Dissertation présentée en vue de l'obtention du grade de
Docteur en Sciences Appliquées
par

Sébastien Faniel

Membres du jury:

Prof. Vincent Bayot, promoteur
Prof. Jean-Paul Issi
Dr. Sorin Melinte
Prof. Luc Piraux
Prof. Jean-Claude Portal
Prof. Mansour Shayegan
Prof. Luc Vandendorpe, président

Décembre 2007

Abstract

Two-dimensional (2D) carrier systems built from semiconductor heterostructures have been at the center of a wide variety of experimental and theoretical research over the past decades. The quality improvement of GaAs/AlGaAs systems has allowed the observation of several peculiar ground states stabilized by the subtle interplay between carrier-carrier interaction, disorder and magnetic field. More recently, 2D systems in semiconductor heterostructures have also been used as a prime substrate for further confinement of the carriers to mesoscopic systems of major interest for the emerging fields of quantum computing and spintronics. This thesis addresses both magnetotransport measurements in hole open quantum dots (QDs) and thermopower studies of 2D holes in (311)A GaAs heterostructures.

In the first part of this thesis, we describe the fabrication process for hole GaAs open QDs and investigate their magnetotransport properties at very low temperature T. Below 500 mK, the magnetoconductance of the open QDs exhibits clear signatures of coherent transport, namely magnetoconductance fluctuations and weak anti-localization. From these effects, we extract a T dependence for the dephasing time τ_ϕ, together with an upper limit for the spin-orbit scattering time τ_{so} using the random matrix theory. Both τ_ϕ and τ_{so} are found to be much smaller than for electrons in similar systems.

In the second part of this work, we report low-T thermopower measurements in the parallel magnetic field-induced metal-insulator transition (MIT) of 2D GaAs hole heterojunctions with different interface-dependent mobilities. When the magnetic field is increased, the diffusion thermopower S^d decreases across the MIT. The reduction of S^d is more pronounced for the lower mobility sample where it reverses its sign. This behaviour indicates that the system does not undergo any ground state modification through the MIT but rather that the parallel magnetic field induces a dramatic change of the dominant hole scattering mechanisms.

Finally, the last part of this thesis is devoted to the thermopower study of the insulating phase (IP) observed in 2D GaAs bilayer hole

systems around the total Landau level filling factor $\nu = 1$. Our measurements show that S^d diverges with decreasing T in the IP. This divergence of S^d at low T indicates the opening of an energy gap in the system's ground state and suggests the formation of a pinned bilayer hole Wigner crystal around $\nu = 1$.

Remerciements

> Beaucoup remercier signifie secrètement demander davantage.
>
> *Proverbe anglais*

Quand vient le temps des remerciements, cela ne signifie qu'une chose : ça y est, c'est terminé! C'est la fin d'une époque (d'une longue, très longue époque). Étrangement, bien que le terme du doctorat procure une satisfaction incomparable, cette dernière est toutefois teintée d'une certaine mélancolie, voire presque déjà de nostalgie. La période qui se termine est, en effet, aussi l'une des plus fascinante qui soit. Je me dois donc, ici, de remercier tous ceux qui ont croisé mon chemin au cours de cette thèse, et qui ont, de quelque manière que ce soit, contribué à l'achèvement de ce travail.

Je voudrais tout d'abord remercier Vincent, mon promoteur de thèse. C'est grâce à lui que j'ai découvert, au cours de mon mémoire de fin d'étude, d'abord, puis tout au long de ce doctorat, le monde attrayant de la physique expérimentale et son principe fondamental, le pragmatisme. Il a su m'aiguiller, au moyen de conseils avisés, au cours de ce long périple, et stimuler ma motivation pendant les périodes les plus creuses.

Je suis aussi très reconnaissant envers Sorin qui a été l'initiateur de certains des virages nécessaires qui ont ponctué ma thèse. Avec lui, j'ai appris la rigueur de l'écriture et de la présentation scientifique. Je le remercie aussi tout particulièrement pour le temps qu'il a passé à relire ce manuscrit.

Sans la fructueuse collaboration qui nous lie au groupe de recherche du Prof. Mansour Shayegan, rien de ce qui est présenté dans ce texte n'aurait été possible. Je remercie donc Mansour et tout son groupe de nous avoir fourni leurs indispensables échantillons, ainsi que pour toutes les discussions scientifiques stimulantes que nous avons pu partager.

J'en viens maintenant à mes collègues, et amis, du groupe basse température (et électronique organique). Je ne peux m'empêcher de

commencer par remercier Cédric avec qui j'ai fait mes débuts en chambres propres (la lithographie sur le Jeol, c'était vraiment quelque chose). C'est aussi avec lui que j'ai partagé mes premières nuits blanches au laboratoire, soit pour des expériences au "fridge", soit pour préparer des transparents. Ces dernières étapes étant généralement jalonnées de brefs passages au Brasse-Temps, histoire de se remonter le moral. Cédric est également l'auteur de ce merveilleux programme d'acquisition qu'est *Nanofreeze*, et qui m'a permis, ainsi qu'à bien d'autres, d'effectuer des mesures dans confort informatique inégalable. Après Cédric, j'en viens tout naturellement à Benoît. Lui aussi a guidé mes premiers pas en tant que doctorant, et a constitué un modèle constant de sérénité en toutes situations. Il est aussi l'initiateur de l'utilisation de la musique du bonding[1], technique qui a certainement sauvé la vie de pas mal d'échantillons. Par la suite, de nouveaux chercheurs sont venus renforcer notre groupe de recherche. En suivant leur ordre chronologique d'appartion, je commencerai par Loïk et Alex (dit *le moldave*). Tout deux ont apporté une joie et une convivialité[2] qui ont contribué à renforcer la bonne entente au sein du groupe. Je dois également les remercier pour l'aide expérimentale qu'ils m'ont apportée, ainsi que pour la multitude de réunions techniques qui se sont terminées au "bar de la vie" tard dans la nuit. Un peu plus tard, d'autres gais lurons sont venus contribuer à la bonne humeur générale : Cristi, Dana, Pierre-Olivier, Gusti et Liviu que je dois remercier personnellement pour m'avoir épaulé au cours des mesures de pouvoir thermoélectrique dans le "fridge".

Une grande partie de ce travail a été réalisée au sein des chambres propres de l'UCL. Je remercie donc tous les techniciens et les chercheurs qui m'y ont apporté une aide précieuse et ont partagé ce ridicule déguisement, nécessaire à l'obtention d'échantillons propres. Parmi eux, je remercie plus particulièrement André, David, Christian, Bohdan, Pierrot, Miloud ainsi que Xiaohui et Nicolas.

Ma gratitude va aussi à tous les membres du PCPM, anciens ou actuels. Cela a été en réel plaisir de travailler dans l'ambiance familiale qui y règne. Parmi les gens que j'ai côtoyés au PCPM, je voudrais particulièrement remercier Sadia, Jean-Michel, qui m'a tiré de pas mal de faux pas informatiques, les secrétaires Brigitte et Viviane ainsi que les techniciens Guy, Luc et Raphaël pour le support technique.

Au cours cette période de thèse, j'ai tissé des liens d'amitié avec bien d'autres chercheurs, croisés au PCPM ou dans d'autres laboratoires. L'amitié est, à mon sens, une condition indispensable à la survie

[1] Don't worry, be happy.

[2] Comme disait un de mes professeur en humanité : boire seul, c'est de l'alcoolisme, boire à plusieurs, c'est de la convivialité.

d'un doctorant. Je ne pourrai malheureusement pas énumérer tout le monde ici (ma thèse a été trop longue), mes ces joyeux trolleurs se reconnaîtront certainement. Je voudrais, toutefois, adresser un remerciement particulier à Laurent, Hanako, Matthieu, Armando, Jean-Michel, Sadia, Sylvain, Yann-Michel, Mariam, Michaël, Joaquin, Greg, Arnaud, Sami, Stéphane, Anne et Simon pour avoir égayé cette époque mémorable.

J'adresse également ma gratitude au membres du jury Vincent Bayot, Jean-Paul Issi, Sorin Melinte, Luc Piraux, Jean-Claude Portal, Mansour Shayegan et Luc Vandendorpe pour avoir pris le temps de soigneusement lire ce manuscrit et pour avoir apporté les commentaires constructifs qui m'ont permis d'en améliorer la qualité.

Finalement, je voudrais remercier mes parents, mes grand-parents et mes frères qui ont toujours été à mes côtés et m'ont soutenu tout au long de cette aventure. C'est en grande partie grâce à eux que j'ai pu tenir pendant les périodes les plus difficiles, et que ce travail a pu être mené à son terme.

Contents

Symbols and abbreviations

$\delta g^{WL/WAL}$	Weak (anti)-localization correction to the conductivity
Δ	Mean level spacing
$\delta(x)$	Delta function
Δ_{SAS}	Gap between the two lowest, symmetric and antisymmetric, double quantum well subbands
κ_l	Lattice thermal conductivity
Λ	Phonon mean free path
λ_F	Fermi wavelength
μ	Carrier mobility
μ_B	Bohr magneton
ν	Landau level filling factor
ω_c	Cyclotron frequency
ρ	Longitudinal resistivity
ρ_{xx}	Longitudinal resistivity of a 2D system subject to a perpendicular magnetic field
ρ_{xy}	Hall resistivity of a 2D system subject to a perpendicular magnetic field
σ	Conductivity
τ_0	Elastic relaxation time
τ_ϕ	Dephasing time
τ_d	Dwell-time
τ_m	Momentum relaxation time
τ_p'	Phonon relaxation time excluding carrier-phonon scattering
$\tau_{\phi N}$	Small energy transfer electron-electron scattering mechanism (Nyquist)
τ_{ee}	Large energy transfer electron-electron scattering mechanism
τ_{erg}	Ergodic time
τ_{pe}	Phonon relaxation time due to scattering from carriers only

τ_{so}	Spin-orbit scattering time
$\vartheta(x)$	Step function
$^1\Delta$	Excitation gap at $\nu = 1$
A	Area of a QD or a quantum ring
B	Magnetic field
$B_\parallel$	Parallel magnetic field
C	Specific heat
$cov(E, E')$	Conductance correlator function
D	Diffusion coefficient
$D(E)$	2D density of states as function of E
E	Energy
e	Electron charge
E_μ	Mobility gap
E_A	Activation energy
E_c	Conduction band energy
E_F	Fermi energy
E_g	Band gap
E_v	Valence band energy
E_Z	Zeeman energy
$f(E, E_F)$	Fermi-Dirac distribution
g	Conductance
g^*	Effective Landé factor
$h, \hbar$	Planck constant
I	Electrical current
K	Dielectric constant
k	Carrier wave vector
k_B	Boltzmann constant
k_F	Fermi wave vector
l_ϕ	Phase coherence length
l_B	Magnetic length
l_m	Mean free path
L_z	Specimen dimension in the confinement direction
m^*	Effective mass
m_e	Free electron mass
n_{2D}	Electron sheet density
p	Hole sheet density
q	Carrier charge
R	Resistance
r_c	Cyclotron radius
r_s	Ratio of the Coulomb energy to the Fermi energy
S	Longitudinal thermopower, Seebeck coefficient
s	Spin quantum number

S^d	Diffusion thermopower
S^g	Phonon-drag thermopower
S_{xx}	Longitudinal thermopower of a 2D system subject to a perpendicular magnetic field
S_{yx}	Transverse thermopower of a 2D system subject to a perpendicular magnetic field
T	Temperature
T_m	Melting temperature
V	Voltage
v_F	Fermi velocity
v_s	Sound velocity
$var(g)$	Variance of the MCFs
$\mathbf{A}$	Magnetic vector potential
$\mathbf{p}$	Canonical momentum operator
$\mathbf{q}$	Average phonon wavevector
1D	One-dimensional
2D	Two-dimensional
2DES	Two-dimensional electron system
2DHS	Two-dimensional hole system
BIA	Bulk inversion asymmetry
CB	Conduction band
DOS	Density of states
FET	Field-effect transistor
FFT	Fast Fourier transform
GE	General electric
HH	Heavy holes
HHh	Heavier heavy holes
HHl	Lighter heavy holes
IP	Insulating phase
LH	Light holes
LL	Landau level
MBE	Molecular beam epitaxy
MC	Mixing chamber
MCFs	Magnetoconductance fluctuations
MIT	Metal-insulator transition
MOSFET	Metal-oxide-semiconductor field-effect transistor
PMMA	Polymethyl methacrylate
QD	Quantum dot
QHE	Quantum Hall effect
QHS	Quantum Hall State
QPC	Quantum point contact
RMT	Random matrix theory

SdH	Shubnikov-de Haas
SEM	Scanning electron microscope
SIA	Structure inversion asymmetry
SO	Split-off band
VRH	Variable range hopping
WAL	Weak anti-localization
WL	Weak localization

List of Figures

List of Tables

Preface

> Le commencement de toutes les sciences, c'est
> l'étonnement de ce que les choses sont ce qu'elles sont.
>
> *Aristote*

The confinement of electrons in two-dimensions has been the source of a vast number of discoveries in recent physics [49]. The most famous among these is certainly the integer quantum Hall effect (QHE) stemming from the quantification of the electron energy levels [160]. However, while the integer QHE can be simply understood by single-particle considerations, the ability of two-dimensional (2D) systems to exhibit rich physics finds its main origin in the major role played by the electron-electron interaction [49]. The prominent role of electron-electron interaction, allowed by the quality improvement of the 2D semiconductor structures, and its interplay with the disorder and the magnetic field B, led to the observation of many peculiar many-body ground states and quasi-particles, such as composite fermions [87, 101], skyrmions [29], Bose-Einstein condensate of excitons [57] or 2D Wigner crystals [18, 81]. Today, after almost thirty years of intensive researh and surprising findings, 2D semiconductor structures remain among the most attracting systems to investigate strongly correlated electrons.

Concomitantly, 2D electron systems were also sorely developped for industrial applications, mainly through the Si metal-oxide-semiconductor field-effect transistor which is currently the most used microelectronic device. Up to now, the improvement of electronic devices has mostly been realized by a reduction of the systems' size. Thanks to the high resolution provided by novel lithographic techniques, it is possible to fabricate devices with dimensions comparable to the electron characteristic lengths. At such mesoscopic scales, new transport regimes are entered, making well-known macroscopic transport laws no longer applicable [50]. Within this context, a clear understanding of the electrons' properties in mesoscopic, confined systems is of first importance for the development of new technological challenges such as quantum computing [14] or

spintronics [162, 204, 214].

This thesis aims to study several aspects of 2D holes confined in (311)A GaAs heterostructures. The choice of these systems was motivated by several reasons. Two-dimensional holes confined to GaAs heterostructures display a stronger spin-orbit interaction than electrons leading to a much more complex band structure and a zero-B spin-splitting, that is of particular interest for the field of spintronics, where the control of the carrier's spin is of major importance. Moreover, 2D GaAs holes present a larger effective mass making carrier-carrier interaction stronger than in GaAs electron systems with similar densities. Finally, hole quantum dots (QDs) are particularly difficult to be controlled experimentally and their realization is still a technological challenge.

Our main findings are the following. First, starting from a 2D GaAs quantum well, we further confine the 2D holes to quasi zero-dimensional mesoscopic structures, namely open QDs. Such devices constitute perfectly suitable tools to investigate the transport properties of carriers in the ballistic and coherent regimes. Second, we address the long-standing problem of the metal-insulator transition (MIT) in two-dimensions. In particular, we investigate the parallel magnetic field $B_{\parallel}$-induced MIT using thermopower measurements, that provide many complementary pieces of informations to those given by more conventional experimental studies. Finally, using our precious thermopower tool, we also study the ground state of the insulating phase (IP) observed around the many-body quantum Hall state at total Landau level filling factor $\nu = 1$. The manuscript is organized in six chapters.

Chapter 1 provides a simple introduction to 2D GaAs heterostructures. It first presents the general fabrication technique, together with some particular recipes, that are used to generate high-mobility 2D electron systems (2DESs). Then, it describes the properties of non-interacting 2DESs. This includes the system's ground state at $B = 0$ and in a perpendicular B, as well as the striking behavior of the longitudinal and Hall resistivities of non-interacting 2DESs subjected to a perpendicular B: the integer QHE. The chapter ends with the more specific description of (311)A GaAs 2D hole systems that are under scrutiny in this work.

Chapter 2 introduces the main mesoscopic transport regimes, namely the ballistic and coherent transport. Then, it describes the open QD mesoscopic structure where both these transport regime coexist. After a presentation of the magnetotransport properties of open QDs, we show the main results of the random matrix theory (RMT) that allows the extraction of carrier scattering time like the dephasing time τ_ϕ or the spin-orbit scattering time τ_{so} from the observed coherent effects. To

conclude the chapter, we present the behavior of τ_ϕ in 2DESs and in open electron QDs.

In Chapter 3, we report on experimental results obtained from GaAs open hole QDs. First, we describe in detail the fabrication process used to produce our samples and the experimental system employed to obtain our low-T magnetotransport measurements. Second, we show the magnetotransport results obtained in both single hole QDs and in arrays of hole QDs that present clear signatures of coherent effects such as magnetoconductance fluctuations (MCFs) and weak anti-localization (WAL) below 500 mK. From an analysis of the WAL effect using the extended RMT, we determine that our QDs are in the strong spin-orbit interaction regime, independent on the symmetry of vertical confining potential. This indicates that the bulk inversion asymmetry contribution to the spin-orbit interaction is sufficient to generate this strong spin-orbit interaction regime. Moreover, from the MCFs and the WAL, we extract a T-dependence for the hole τ_ϕ using the extended RMT. The evolution of the obtained τ_ϕ for holes is similar to that reported for electrons, however its absolute value is found to be approximately one order of magnitude smaller.

We briefly recall, in Chapter 4, the essential concepts to understand thermopower S in two-dimensions. The two mechanisms that contribute to the thermopower in GaAs heterostructures, the diffusion thermopower S^d and the phonon-drag thermopower S^g, are presented. We describe, in particular, the behavior of the diffusion thermopower S^d for various 2D ground states, including a degenerate carrier gas, an energy gap, a mobility gap and a Coulomb gap. At the end of the chapter, we present the samples' preparation and the measurement technique we employed to study thermopower below 500 mK.

Chapter 5 is devoted to the study of the $B_\parallel$-induced MIT observed in (311)A GaAs heterojunctions. The metallic evolution of the resistivity with T in low carrier density 2D systems have attracted much interest over the past decades since they were expected theoretically to solely behave as insulators. In this chapter, we use thermopower measurements, that provides valuable informations on both the system's ground state and the scattering mechanisms, to investigate the metallic regime and the transition to an insulating behavior driven by $B_\parallel$. We study two samples with different interface-dependent mobilities. The diffusion thermopower decreases across the MIT. The reduction of S^d is more important for the lower mobility sample where it reverses its sign. The behavior of S^d suggests that the systems does not undergo any ground state modification: the 2D systems behave as a degenerate hole gas both in the metallic and in the insulating states. Instead, our results rather

indicate that at the MIT, $B_{\|}$ induces a dramatic change of interface roughness and intersubband scattering mechanisms.

Finally, in Chapter 6 we study the thermopower in GaAs bilayer hole systems. When subjected to a perpendicular B, strongly interacting bilayer hole systems with weak interlayer tunneling exhibit a many-body quantum Hall state (QHS) at $\nu = 1$. This state in flanked with a reentrant IP when the densities of the two layers are equal. The IP observed in bilayer systems around $\nu = 1$ is reminiscent of that observed in GaAs 2D electron single-layers [49, 81, 104] around the fractional QHS at $\nu = \frac{1}{5}$ and electron bilayers [126] in the vicinity of total filling factor $\nu = \frac{1}{2}$, as well as in dilute, single-layer, GaAs 2D hole systems [171] near $\nu = \frac{1}{3}$, which were attributed to the formation of pinned Wigner crystals. It was suggested in Ref. [187] that the IP observed in bilayer hole systems could signal the formation of a bilayer Wigner crystal, stabilized at such high ν by strong Landau level mixing due to higher effective mass of holes, and by the interlayer Coulomb interaction in the bilayer system. The diffusion thermopower is an unique tool to study IP's in 2D systems as it can distinguish between a mobility gap (disorder-induced IP) and an energy gap (Wigner crystal). Our measurements show that S^d diverges in the reentrant IP's when T is decreased. It indicates the opening of an energy gap in the system's ground state and suggests the formation of a pinned bilayer Wigner crystal near $\nu = 1$.

Chapter 1

Two-dimensional carrier systems

> Ne me dites pas que ce problème est difficile. S'il n'était pas difficile, ce ne serait pas un problème.
>
> *Ferdinand Foch*

1.1 Introduction

Two-dimensional (2D) systems are generally produced by confining carriers at the interface of two different materials. Up to now, several methods have been developed to realize such confinement including helium surfaces [83], semiconductor field-effect transistors (FETs) and heterostructures [12, 35, 51, 52], as well as novel systems like noble-metal surfaces [33], organic FETs [61, 79, 210] and graphene [144, 145]. The most popular among these are FETs and heterostructures. These two different techniques have led to the realization of 2D carrier systems with a large range of carrier densities and mobilities. Since their discovery, they have generated much interest both for electronic applications and fundamental reseach. In particular, Si-MOSFETs, made of a three-layered structure combining a doped Si substrate covered with an insulating layer SiO_2 and a metallic gate, provide a high quality, low cost transistor that became the most used device in the electronic industry. On the other hand, the extremely clean 2D carrier systems produced in III-V heterostructures have allowed the carrier-carrier interaction to become a prominent parameter, leading to the observation of new quantum phases.

The systems investigated in this work were produced from 2D p-type GaAs/AlGaAs heterostrutures. This chapter will then briefly review the fabrication process as well as the general properties of GaAs/AlGaAs heterostrutures and will finally provide more specific description of 2D GaAs hole systems.

1.2 The GaAs/AlGaAs Heterostructure

1.2.1 Materials

$Al_xGa_{1-x}As$ based semiconductors combine Al and Ga atoms from the group IIIa with As atoms originating from the group Va. Together, they alloy as GaAs, AlAs or $Al_xGa_{1-x}As$ with a zinc-blende cristallographic structure (Fig. 1.1(c)). Important features of these compounds are the following:

- The lattice parameter a of the binary compounds are 5.6533 Å for GaAs and 5.6611 Å for AlAs at room temperature T. When alloyed in the ternary form $Al_xGa_{1-x}As$, the lattice parameter follows the Vegard's law and increases linearly with the Al fraction x (upper panel of Fig. 1.1(b)) [51].

- As illustrated in Fig. 1.1(a), at room temperature, GaAs has a direct band gap $E_g = 1.42$ eV at Γ points while AlAs presents an indirect band gap $E_g = 2.17$ eV with a maximum at Γ points for the highest valence band and a minimum at X points for the lowest conduction band. For the ternary compound $Al_xGa_{1-x}As$, the evolution as a function of x of the energy gaps between the maximum in the highest valence band at Γ points and the minima of the lowest conduction band at Γ, X and L points is shown in the lower panel of Fig. 1.1(b). This compound undergoes a direct to indirect band gap transition when x becomes larger than ~ 0.45 [3].

- The lowest conduction band $6c$ is always non-degenerate while the highest valence band $8c$ is three-fold degenerate at Γ points if spin-orbit interaction is neglected.

1.2.2 Heterostructures

Even though it's the most used device in electronic industry, the Si-MOSFET does not provide the cleanest 2D carrier systems. The carrier mobility in these devices suffers from two major limitations. First, as the

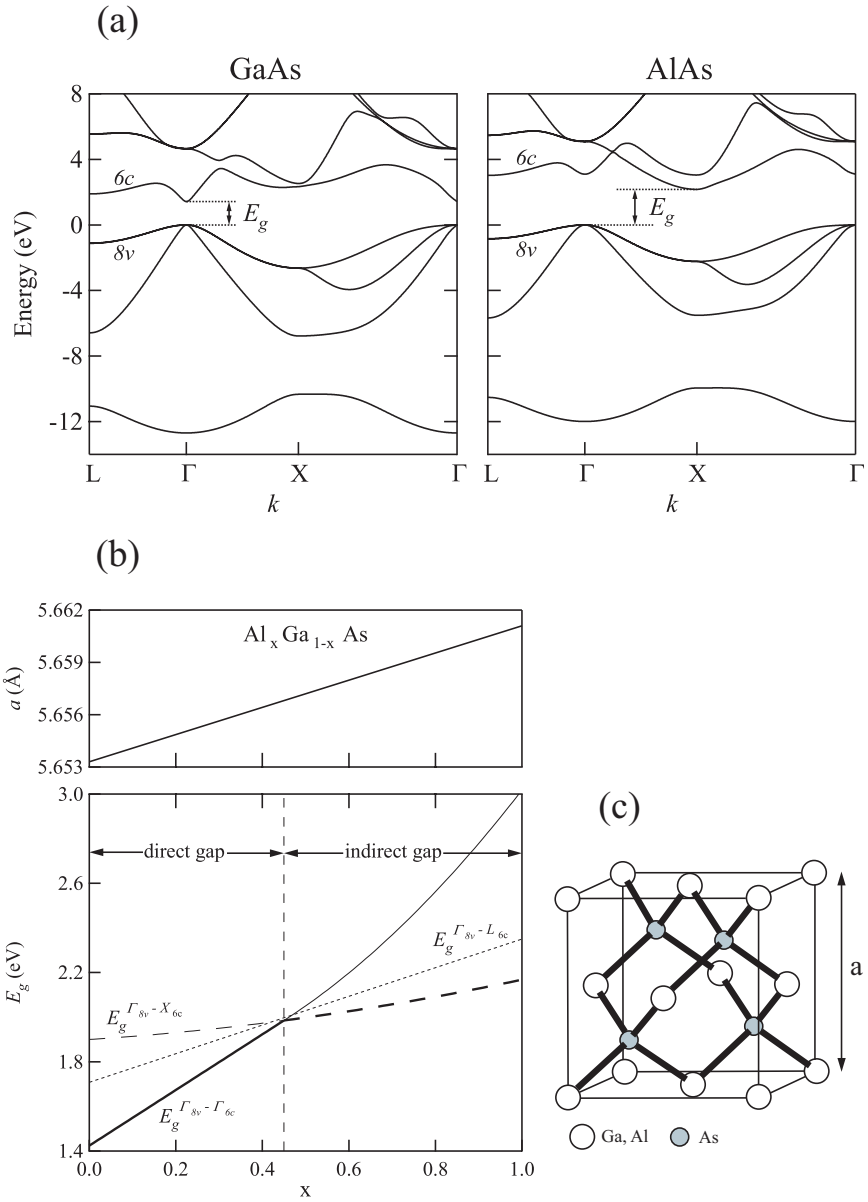

Figure 1.1: (a) Band structure of bulk GaAs and AlAs without spin-orbit interaction (courtesy of P. Boulange). (b) Evolution as a function of x of the lattice parameter a (upper panel) and the band gaps (lower panel) for the $Al_xGa_{1-x}As$ alloy. (c) Zinc-blende structure of the GaAs, AlAs and $Al_xGa_{1-x}As$ crystals.

carriers are confined in the doped Si, scattering by the dopants is important. Secondly, the strongly disordered interface between the crystalline Si and the amorphous SiO_2 generates a large interface roughness scattering. These limitations are naturally circumvented in GaAs/AlGaAs heterostructures that provide very high-mobility 2D carrier systems at low T. Figure 1.2 shows the T-dependence of the mobility for various 2D GaAs heterostructures and also illustrates the improvement of the systems' mobility over a period of 10 years. In this section, the fabrication and the properties of 2D GaAs/AlGaAs heterostructures will be presented. The case for a n-type system is used as an illustration.

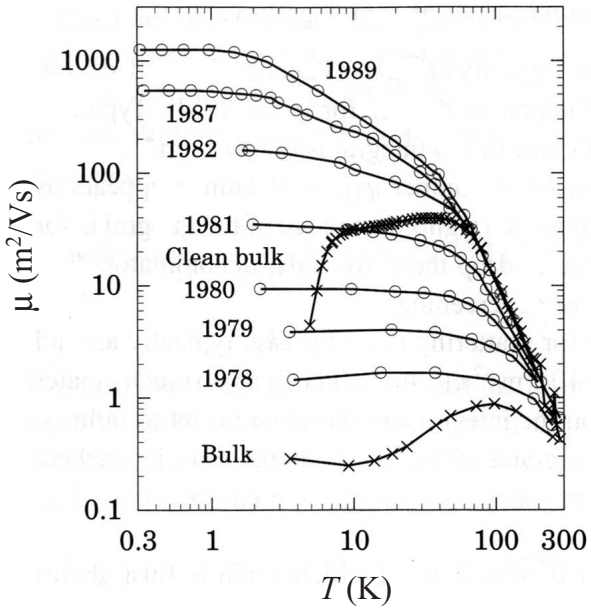

Figure 1.2: Temperature dependence of the mobility for various 2D GaAs heterostrutures, showing how the electron mobility has been enhanced over 10 years (from Ref. [51]).

Two-dimensional electron systems (2DES) in GaAs/AlGaAs heterostructure are built by contacting an n-doped AlGaAs layer and a layer of intrinsic GaAs (see Fig. 1.3). In order to maintain the alignment of the Fermi energies in the two materials, the electrons given by the dopant atoms (generally Si) from the AlGaAs layer move to the conduction band of the GaAs layer. The electrons leave behind positively charged ions. This generate an internal electric field that bends the conduction band and leads to the formation a confining potential at the interface of the

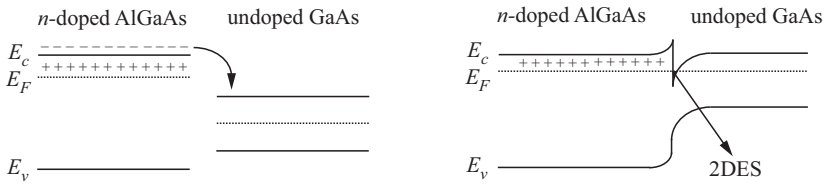

Figure 1.3: Schematic representation of the formation of a 2DES at the interface of a doped AlGaAs layer with an undoped GaAs layer (E_c is the conduction band energy, E_v is the valence band energy). The dotted line shows the Fermi energy E_F.

two materials. Electrons are then trapped inside the GaAs layer at the interface with the AlGaAs layer. The fabrication of such semiconductor heterostructures has been allowed by the development, in the early 70s, of the molecular beam epitaxy (MBE) [38]. The MBE technique achieves the growth of monocrystalline multiple-layer structures with an atomic scale control of layer thickness, composition and doping profile.

Contrary to the case of the Si-MOSFET, the electrons and the dopant atoms in heterostructures are spatially separated: consequently, scattering by the dopants is strongly reduced. Moreover, as stated above, the GaAs and AlGaAs layers are perfectly lattice matched. As a result, the interface between these two materials is weakly disordered and interface roughness scattering is small. Finally, a third reason for the high mobility of GaAs heterostructure is the low effective mass[1] m^* of electrons in these structures. As the electrons are confined in the GaAs layer, the relevant effective mass in 2D GaAs/AlGaAs heterostructures is the isotropic effective mass of bulk GaAs $m^* = 0.067\ m_e$, where m_e is the free electron mass. For comparison, the effective mass in Si is anisotropic and has the following values: $m^* = 0.97\ m_e$ along the [100] crystallographic direction, while $m^* = 0.19\ m_e$ along the [010] and [001] crystallographic directions.

Beyond the above mentioned reasons for the high electron mobility of GaAs/AlGaAs heterostructures, several fabrication recipes have been applied to further improve the quality of the 2DES [127]:

- An undoped layer of AlGaAs is generally inserted between the

[1] While moving in a solid, electrons experience the periodic potential of the crystal lattice. The effect of this potential can simply be introduced in the Schröedinger equation by replacing the free electron mass m_e by an effective value m^*. The value of m^* is given by the curvature of the dispersion relation relating the energy of the carrier to the wave vector.

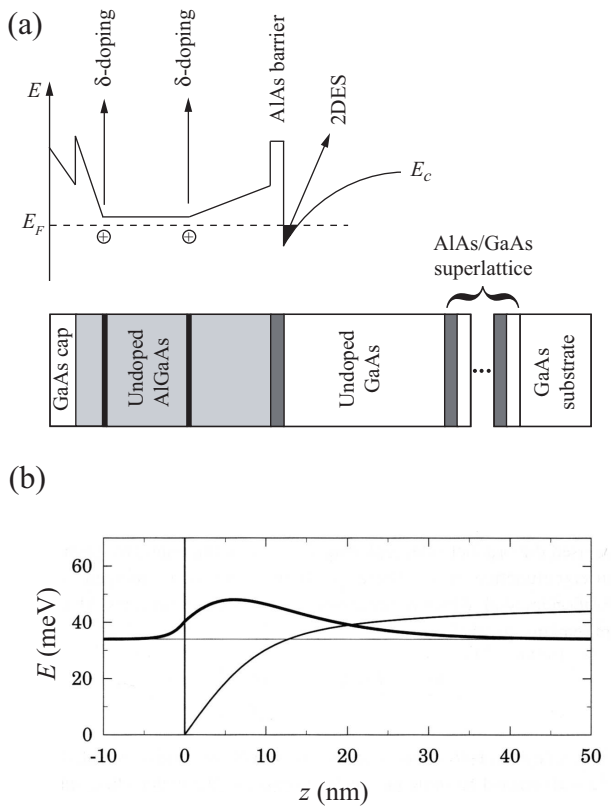

Figure 1.4: (a) Illustration of the growth sequence of a high mobility GaAs/AlGaAs heterostructure with the corresponding conduction band energy E_c. The dashed line shows the Fermi energy E_F. (b) Realistic potential well and wave function for a GaAs/AlGaAs heterojunction determined by self-consistent Hartree calculation (from Ref. [51]).

GaAs and the doped AlGaAs layers. This layer, called *spacer*, increases the spatial separation between the carriers and the dopants and, as a result, decreases remote ions scattering.

- A narrow AlAs barrier can be inserted between the GaAs layer and the spacer in order to increase the confinement of the electronic wavefunction in the GaAs layer. As the penetration of the electronic wavefunction in the spacer is strongly decreased and AlGaAs is replaced by an AlAs layer with no alloy disorder at the interface, alloy scattering experienced by the electrons in the 2D system is reduced.

- The potential fluctuations at the interface due to remote ionized dopants can be minimized if the thickness of the doping region is reduced to zero. The doped AlGaAs layer is then replaced by undoped AlGaAs and a very narrow layer of dopants. This technique is known as *δ-doping*.

- The doping region provides charges both for the 2DES and to passivate the surface states of the GaAs cap layer. By using a second δ-doped layer placed closer to the sample's surface in order to passivate these surface states, it is possible to increase the 2D system's mobility. Indeed, the additional dopants that passivate the surface states are far away from the confining interface and do not contribute to remote ion scattering in the 2DES.

- Some impurities are also introduced by the substrate itself. In order to avoid the diffusion of these impurities to the region where the 2DES is formed, during the growth process, an AlAs/GaAs *gettering* superlattice is grown first. In such a superlattice, the migrating impurities are trapped at the AlAs/GaAs and GaAs/AlAs interfaces.

A more complete schematic representation of the growth sequence of a n-type GaAs/AlGaAs heterostructure with the corresponding band structure is shown in Fig. 1.4(a). Such systems formed at single GaAs/AlGaAs interfaces are called *heterojunctions* and provide 2D electrons confined to a roughly triangular confining potential (the actual shape of the potential well of a GaAs/AlGaAs heterojunction is shown in Fig. 1.4(b)). In a different type of structure, referred to as a *quantum well*, the GaAs layer is sandwiched between two layers of AlGaAs. In this case, dopants are sometimes used on both sides of the 2DES. In order to fabricate 2DESs with comparable densities, larger spacers can be used in

the case of the quantum wells. As a consequence, remote ion scattering is reduced and, as long as the second interface does not increase interface roughness scattering, the electron mobility is improved. Moreover, one important property of the quantum wells is that they provide structures where electrons are trapped to square confining potentials. The symmetry of such confining potential is of great interest in studies of systems where spin-orbit interaction plays an important role (see Section 1.4.3).

1.3 Non-interacting 2D electron system

1.3.1 Case for zero magnetic field

In the most simplified approach, a 2DES can be described as a Fermi gas. In such a picture, the interaction between electrons is neglected. Let's consider an electron in a material with an isotropic effective mass. This electron is free to move along the x and y directions but is subject to a confining potential $V(z)$ along the z direction. If there is no disorder, such a system is described by the Schöedinger equation in the following form:

$$\left[-\frac{\hbar^2}{2m^*}\nabla^2 + V(z)\right]\psi(x,y,z) = E\psi(x,y,z), \tag{1.1}$$

where $\hbar$ is the Planck constant, E is the energy and $\psi(x,y,z)$ is the wave function. As there is no potential along x and y, the motion of the electron along these directions can be described by plane waves. On the other hand, along the z direction, the electron experiences the confining potential and its energy is quantified into discrete level ε_m that are solutions of the one-dimensional Schröedinger equation:

$$\left[-\frac{\hbar^2}{2m^*}\frac{d^2}{dz^2} + V(z)\right]u_m(z) = \varepsilon_m u_m(z), \tag{1.2}$$

where $m = 0, 1, 2, ...$ is a positive integer and $u_m(z)$ are the wave functions corresponding to each quantum number m. If $V(z)$ is an infinite square quantum well:

$$V(z) = \begin{cases} \infty & \text{for } |z| \geq w/2 \\ 0 & \text{for } |z| < w/2 \end{cases},$$

where w is the width of the quantum well, then ε_m is given by

$$\varepsilon_m = \frac{\hbar^2\pi^2(m+1)^2}{2m^*w^2}, \tag{1.3}$$

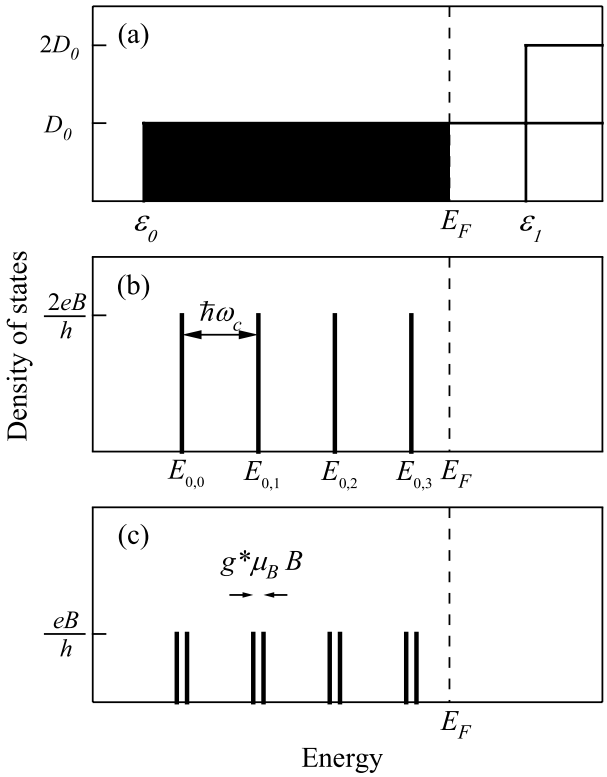

Figure 1.5: Density of states of a 2DES for (a) $B = 0$, (b) $B \neq 0$ (no spin) and (c) $B \neq 0$ (with spin).

The total energy of the electron in the 2D system writes as

$$E_m(k) = \frac{\hbar^2 k_x^2}{2m^*} + \frac{\hbar^2 k_y^2}{2m^*} + \varepsilon_m, \tag{1.4}$$

where k is the total wave vector, k_x and k_y are the wave vectors along the x and y directions, respectively. The quantified energy levels along the z direction are well resolved and they are referred as electrical subbands.

Once we know the allowed energy levels in the 2D system, we can see how it's possible to fill them with electrons. Let's condider a system with a known electron sheet density n_{2D}. The electron sheet density is given by the following formula:

$$n_{2D} = \int_{-\infty}^{\infty} D(E) f(E, E_F) dE, \tag{1.5}$$

where $D(E)$ is the 2D density of states (DOS), $f(E, E_F)$ is the Fermi-

Dirac occupation function and E_F is the Fermi energy. In 2D systems, the DOS can be decomposed into contributions from each subband. The DOS per unit area for each electrical subbands has a constant value, and is given by

$$D_0 = \frac{m^*}{\pi\hbar^2}. \tag{1.6}$$

The total DOS then writes as

$$D(E) = D_0 \sum_m \vartheta(E - \varepsilon_m), \tag{1.7}$$

where $\vartheta(x)$ is a step-like function. The total DOS is represented in Fig. 1.5(a) and is a step-like function with jumps of D_0 occuring when the energy reach the bottom of an electrical subband ε_m. We note here that in most 2DESs, only the lowest electrical subband is populated.

1.3.2 Case for a perpendicular magnetic field

For the 2D systems considered here above, if a perpendicular magnetic field B is applied, then the Schröedinger equation writes as

$$\left[\frac{1}{2m^*}(\mathbf{p} + e\mathbf{A})^2 + V(z)\right]\psi(x, y, z) = E\psi(x, y, z), \tag{1.8}$$

where $\mathbf{p}$ is the canonical momentum operator and $\mathbf{A}$ is the magnetic vector potential[2]. This magnetic vector potential can be chosen as $\mathbf{A} = (0, Bx, 0)$. The Schröedinger equation can be reformulated in the following form,

$$\left[-\frac{\hbar^2}{2m^*}\nabla^2 - \frac{ie\hbar Bx}{m^*}\frac{\partial}{\partial y} + \frac{(eBx)^2}{2m^*} + V(z)\right]\psi(x, y, z) = E\psi(x, y, z). \tag{1.9}$$

One can see from this equation that B only couples to the motion of the electrons in the plane of the 2D system (along x and y). Classically, through the Lorentz force, the magnetic field drives the electrons in a circular motion at a frequency ω_c, known as cyclotron frequency and given by:

$$\omega_c = \frac{|e|B}{m^*}, \tag{1.10}$$

[2]The magnetic potential vector is defined as follows: $\vec{B} = r\vec{o}t\vec{\mathbf{A}}$.

and with a cyclotron radius r_c of

$$r_c = \sqrt{\frac{\hbar}{eB}}, \tag{1.11}$$

where e is the electron charge. As the magnetic field only affects the motion of electron within the plane of the 2D system and confining potential along the z direction has only an additive contribution, the in-plane and transverse part of Eq. (1.9) can be solved separately. This leads to the following total energy for the electrons:

$$E_{m,r} = \varepsilon_m + \hbar\omega_c(r + \frac{1}{2}), \tag{1.12}$$

where $m, r = 0, 1, 2, ...$ are positive integers and ε_m are the transverse electrical subbands given by Eq. (1.3). The electron energies obtained here are independent of k. The electrons condensate into highly degenerate energy levels, called Landau levels (LLs). For levels originating in the same transverse electrical subband, the energy gap between two Landau level is $\hbar\omega_c$ while the degeneracy of each level is $2(eB/h)$. The DOS of a 2DES subject to a magnetic field is then given by

$$D(E, B) = 2\frac{eB}{h}\sum_{m,r}\delta\left(E - E_{m,r}\right), \tag{1.13}$$

where $\delta(x)$ is the delta function. This DOS, represented in Fig. 1.5(b), is made of a series of δ-like LLs. When B is swept up, the LLs move away from each other and are depopulated when passing through E_F. The increase of B also induces a variation of E_F. Indeed, E_F moves with the DOS in order to keep the number of electrons constant: the Fermi level follows the evolution of the highest LL until it is completely empty and then jumps to the following LL. The evolution of E_F as a function of B is shown in Fig. 1.6 for a perfect 2D systems with δ-like LLs.

In the previous developments, the spin of the electron has been neglected. However, when a magnetic field is applied, the electron spin can no more be omitted as B interacts with it through the Zeeman splitting. This particular interaction can be inserted in the Schröedinger equation by adding the following term to the hamiltonian of Eq. (1.8):

$$H_Z = sg^*\mu_B B, \tag{1.14}$$

where $s = \pm\frac{1}{2}$ is the spin quantum number of the electron, g^* is the effective Landé factor and μ_B is the Bohr magneton. With this additional term, the energy spectrum and the DOS reads:

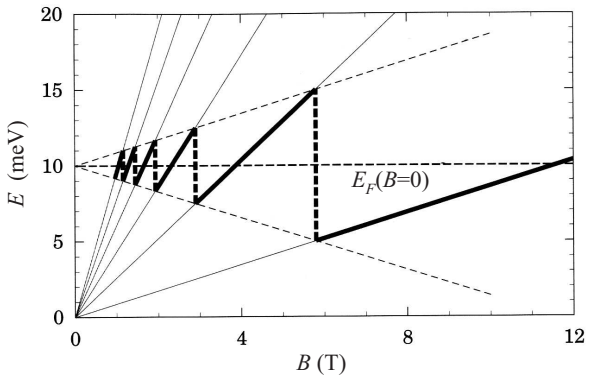

Figure 1.6: Variation of E_F as a function of B for a perfect 2D system with δ-like LLs and $E_F(B=0) = 10$ meV. The fan of thin lines shows the evolution of the LLs' energies while the thick one indicates E_F (from Ref. [51]).

$$E_{m,r,s} = \varepsilon_m + \hbar\omega_c(r + \frac{1}{2}) + sg^*\mu_B B, \tag{1.15}$$

and

$$D(E,B) = \frac{eB}{h}\sum_{m,r,s}\delta\left(E - E_{m,r,s}\right). \tag{1.16}$$

As shown in Fig. 1.5(c), for each Landau level, electrons with different spins split into two new level that have half the degeneracy of the initial ones and that are separated by the Zeeman energy $E_Z = g^*\mu_B B$. It's useful to define here the LL filling factor ν that measures the number of spin non-degenerate LLs that lie below E_F:

$$\nu = \frac{n_{2D}h}{eB}. \tag{1.17}$$

1.3.3 Magnetotransport in two-dimensional systems

Within the Drude model, developed for degenerate electron gas, the longitudinal and Hall resistivities, ρ_{xx} and ρ_{xy} of a 2D system subject to a perpendicular B, are expected to be

$$\rho_{xx} = \frac{1}{|e|n_{2D}\mu} \qquad \text{and} \qquad \rho_{yx} = \frac{B}{|e|n_{2D}}, \tag{1.18}$$

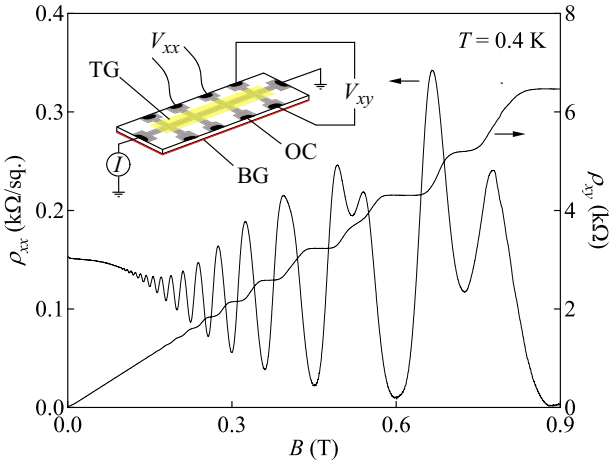

Figure 1.7: Longitudinal and Hall resistivities as a function of B and at $T = 0.4$ K of a 2DES with a density of $n_{2D} = 8.5 \times 10^{14}$ m^{-2}. Inset: Schematic representation of the sample geometry and measurement configuration for the determination of the longitudinal and Hall resisivities. The shaded area shows the Hall bar where the 2D carrier system has been confined. The ohmic contacts (OC), the metallic top gate (TG) and back gate (BG) are also shown.

where μ is the system mobility. When B is swept up, ρ_{xx} is expected to be constant while ρ_{xy} should increase linearly. The measured low T longitudinal and Hall magnetoresistivities of a 2DES are shown in Fig. 1.7. The prediction of the Drude model are correct only at low B ($\lesssim 0.1$ T). At higher B, the longitudinal resistivity shows Shubnikov-de Haas (SdH) oscillations, while the Hall resisivity exhibits a series of plateaus. This spectacular behaviour find its origin in the quantification of the electron energy into LLs that is not taken into account by the Drude model and is referred as the integer quantum Hall effect (QHE).

In order to explain the integer QHE, several crucial points, that have been omitted in the previous description of 2DESs, have to be clarified [50, 160, 207]:

- The measured samples have always a finite size. The edges of the sample can be represented as confining potentials along the x and y direction. These confining potentials are zero in the bulk of the sample but increase at the edges. The electron states, *i.e.* the LLs, behave similarly as the confining potential. Their energies are given by Eq. (1.12) in the bulk of the sample but increase when the edge is approached. There are then allowed energy states at the Fermi

energy close to the edges of the sample, these particular states are referred as edge states.

- The unavoidable presence of disorder in a 2DES broadens the δ-like Landau levels so that they have a rather gaussian-like shape. Moreover, due to disorder, we also have to distinguish the extended states that have energies centered around the original LLs energies and the localized states. These states are schematically represented in Fig. 1.8. Finally, one last important point concerning these states is that only the extended states can carry an electrical current.

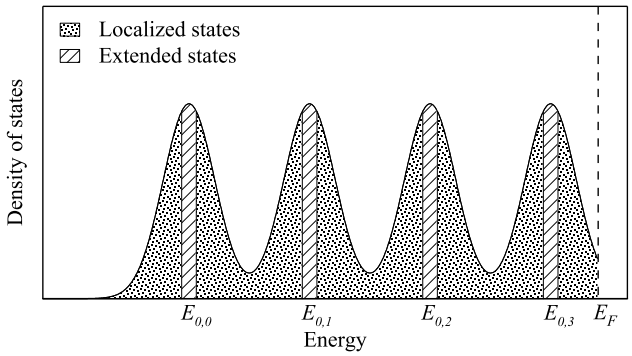

Figure 1.8: Broadening of the LLs due to the presence of disorder. The extended states are centered around the original position of the LLs, while the localized states lie between the extended states.

When a 2D system is subjected to a magnetic field, two different situations can exist. First, if E_F lies in the extended states that spread over the entire sample, then the system behaves as a normal metal: its longitudinal resistivity has a finite value and the Hall resistivity increases with B. On the other hand, if E_F lies in the localized states, only the edge states can carry an electrical current. Edge states on opposite sides of the sample will carry the electrical current in opposite directions[3]. Due to the spatial separation of the electron states that carry the current in opposite direction, the backscattering of electrons is almost impossible as only localized states are populated in the bulk of the sample: the

[3]In a classical picture, B drives the electrons into circular orbits. Close to the edges of the sample, the circular orbits bounce and conduct the electrical current along the edge of the sample. These conducting trajectories as referred as skipping orbits.

longitudinal resistivity then exhibits a minimum at integer ν. In this particular configuration, the Hall resistivity is flat. It can be shown that each egde state contributes equally to the total current [50], ρ_{xy} then has a value that depends only on the number of occupied edge states (or LLs) M and on fundamental constants:

$$\rho_{xy} = \frac{1}{M}\frac{h}{e^2}. \tag{1.19}$$

It is necessary to highlight here the importance of the localized states. They allow to the Fermi level to lie between two extended states. The gradual transition of the Fermi level from one extended state to the other is a key ingredient for the observation of the quantum Hall effect, as it allows for the measurements of plateaus of finite width in the Hall magnetoresistivity of a 2DES.

The existence of the integer QHE is intimately related to the quantification of the electron energy states in Landau levels. This implies that the LLs need to be well resolved. More precisely, the broadening of the energy levels due to the presence of disorder or to the temperature has to be smaller than the energy gap between two extended states. These conditions can be formulated as follow:

$$\frac{h}{\tau_m}, k_B T \lesssim \hbar\omega_c, \tag{1.20}$$

where τ_m is the momentum relaxation time, k_B is the Boltzman constant. It can be observed from Fig. 1.7 that above ~ 0.5 T, the oscillations of ρ_{xx} splits in two. This effect is due to the resolution of the spin energy levels. Similar to the previous case, it happens when the E_Z is sufficiently larger than the energy level broadening:

$$\frac{h}{\tau_m}, k_B T \lesssim g^* \mu_B B. \tag{1.21}$$

The magnetotransport properties of 2DESs have been described in this section whithout considering weak localization and electron-electron interaction. Of course, in a 2DES produced at the GaAs/AlGaAs interface, these effects can not be neglected. The weak localization brings a quantum correction to the resistivity that leads to the observation of a negative magnetoresistivity peak around $B = 0$. The weak localisation will be further described in the next chapter in the context of coherent transport. Electron-electron interaction combined with disorder and magnetic field has been shown, both experimentally and theoretically, to generate many new quantum phases, including electron solids [18, 81], as

well as composite fermions [87, 101], skyrmions [29], Bose-Einstein condensates [57] ... Some of these many-body ground states will be studied later in the text through thermopower experiments.

1.4 The two-dimensional GaAs hole system

1.4.1 Realization

GaAs/AlGaAs 2DESs are most often produced by growing the layer sequence detailed in Section 1.2.2 starting from a (100) GaAs wafer and using Si atoms as donors in the δ-doped layer. Two-dimensional hole systems (2DHSs) can be fabricated using a similar procedure and substituting Be for Si to dope the structure. However, Be atoms easily diffuse during the growth process and, as a result, reduce the hole mobility at the GaAs/AlGaAs interface. Another way to generate 2DHSs is to keep the Si atoms as dopants but to use a (311)A GaAs wafer as substrate. When the sample's growth is performed on such a substrate, the Si atoms substitute preferentially for the As atoms instead of the Al or Ga atoms and, as a consequence, act predominantly as acceptors. The 2DHSs investigated in this work were all fabricated from (311)A GaAs wafers, using Si atoms as dopants.

1.4.2 Interface roughness scattering

Two dimensional hole systems grown from (311)A wafer exhibit a mobility anisotropy: holes have a higher mobility along the $[\bar{2}33]$ (high-μ) cristallographic direction than along the $[01\bar{1}]$ (low-μ) cristallographic direction. A careful study of the hole mobility as a function of the hole sheet density p has shown that the main scattering mechanisms along the high-μ direction is remote ionized impurity scattering, while, along the low-μ, interface roughness scattering dominates [91]. The mobility anisotropy hence originates from an increase of interface roughness scattering along the $[01\bar{1}]$ direction. This behaviour has been elucidated through scanning tunneling microscope imaging of a (311)A GaAs surface after the MBE growth. The images revealed that the surface's morphology shows both nanoscopic and mesoscopic corrugations [143, 197]. The nanoscopic surface corrugation, that stems from a surface reconstruction, has a periodicity of ~ 3 nm, much smaller than the hole Fermi wavelength[4] and, as a result, does not affect the hole mobility. As for the mesoscopic corrugation, it ripples over lengths of the same order of magnitude as λ_F. The anisotropic hole mobility then likely comes from

[4]For a 2D system with a typical hole density $p = 2 \times 10^{15}$ m^{-2}, $\lambda_F = 56$ nm.

the aperiodic mesoscopic surface corrugations that are embedded in the GaAs/AlGaAs interface during the growth process.

1.4.3 Spin-orbit interaction

In the previous sections, we have presented the properties of GaAs 2DESs. In this case, the spin-orbit interaction is weak[5] and was not taken into account. For the specific case of GaAs 2D holes, however, spin-orbit interaction is important and strongly modifies the band structure [202]. Before presenting its effects in detail, it is useful to briefly define the spin-orbit interaction. Spin-orbit interaction is a relativistic effect that couples the spin of a particle to its orbital angular momentum. It can simply be depicted as follows. Let's consider a charged particle that moves in an electric field. This particle feels an effective magnetic field in its own frame of reference. The effective magnetic field interacts with the particle's spin and, as a result, modifies its energy.

In bulk GaAs, the electric field that leads to the spin-orbit interaction originates in the lack of inversion symmetry of the zinc-blende crystallographic structure. This contribution to the spin-orbit interaction is generally referred as the bulk inversion asymmetry (BIA) or as the Dresselhaus term. We have seen in Section 1.2.1 that if the spin-orbit interaction is neglected, the valence band is threefold degenerate around the Γ points. When spin-orbit interaction is taken into account, this degeneracy if lifted. The resulting band structure of bulk GaAs close to the fundamental gap is presented in Fig. 1.9(a). One of the subbands, the split-off band (SO), is shifted downwards by Δ_{so} in energy. The two other bands are split but remain degenerate at $k = 0$. As their curvatures are not the same, different effective masses are associated with each band. We distinguish the light hole band (LH) with $s = \pm\frac{1}{2}$ and the heavy hole band (HH) with $s = \pm\frac{3}{2}$.

In heterostructures, one additional term contributes to the total spin-orbit interaction. This contribution stems from the electric field produced by the asymmetry of the vertical confining potential and is referred as the structure inversion asymmetry (SIA) or as the Rashba term. One important property of the SIA is that, contrary to the BIA that only depends on the crystallographic structure and hole density, it can be considerably tuned experimentally by means of top and/or back gates (see inset to Fig. 1.7). Within this context, the fabrication of quantum wells with square vertical confining potential is particularly interesting as the SIA contribution to the total spin-orbit interaction can be recuced

[5]The weakness of the spin-orbit interaction in 2D GaAs electron systems can be evidenced, e.g. by the absence of weak anti-localization at low T [39].

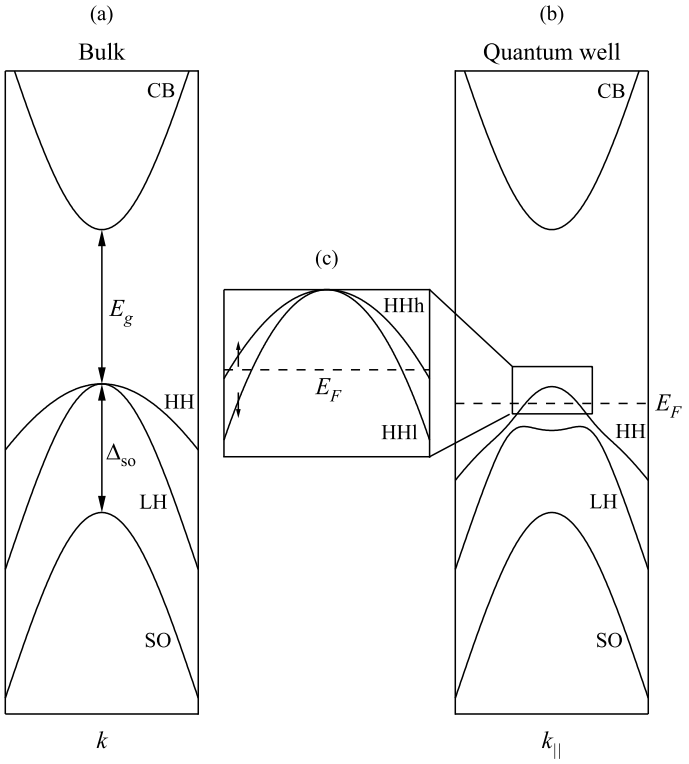

Figure 1.9: Band structure of GaAs around the fundamental gap with spin-orbit interaction for (a) a bulk system and (b) a 2D system. (c) Magnified view of the HH subband spin splitting into the HHh and HHl subbands.

to zero in such structures. When holes are confined to a 2D system, the degeneracy of the HH and LH subbands at $k = 0$ is lifted and the subband energies are shifted. For a confined system, the heavy or light character of the bands refers to the effective masses in the confinement direction. Since the confinement-induced subband energies are inversely proportional to the effective mass perpendicular to the 2D system, the LH subband has a larger hole energy than the HH subband. Nevertheless, within the plane, the heavy or light character of the HH and LH subbands are reversed: the LH subband has a heavier in-plane effective mass than the HH one. The energy shift as well as the anti-crossing of the HH and LH subbands around the fundamental gap are schematically represented as a function of $k_{||}$ in Fig. 1.9(b). Depending on the confinement properties, the mixing of the LH and HH subbands can

reverse the curvature of the LH subband near $k = 0$ and lead to a negative hole effective mass in this subband. In our samples, however, the Fermi energy and the 2D system's thickness are small enough so that only the HH subband is populated. Considering $E(k_{\parallel})$ of the different subbands, it can be shown that for the conduction band (CB) and the SO band, the Fermi surfaces remain almost circular. For the LH and HH subbands, however, the Fermi contour is warped and therefore the hole effective masses within the plane of the 2D system are anisotropic. One last effect of the spin-orbit interaction has to be taken into account. As explained previously, due to the presence of an electric field, the holes feel an effective magnetic field which lifts the remaining degeneracy of the different subbands, namely the spin degeneracy, at finite wave vectors. If we consider a 2DHS with only the HH subband populated, the spin-orbit interaction splits the HH subband as shown in Fig. 1.9(c) and generates a zero-B spin splitting. The two new spin subband are referred as the heavier heavy holes (HHh) and the lighter heavy holes (HHl) subbands. The exact determination of the effectives masses associated with the HHl and HHh subbands is quite difficult as they depend on sample's parameters such as the width of the confining potential and the hole density. Several studies [41, 94, 127, 147] have attempted to measure these quantities and have determined that they can reasonably be expected to lie between ~ 0.2 and $\sim 0.6\ m_e$.

Chapter 2

Mesoscopic transport in open quantum dots

> La théorie, c'est quand on sait tout et que rien ne fonctionne. La pratique, c'est quand tout fonctionne et que personne ne sait pourquoi. Ici, nous avons réuni théorie et pratique : Rien ne fonctionne... et personne ne sait pourquoi !
>
> *Albert Einstein*

2.1 Introduction

Intensive and ceaseless efforts have been devoted to the quest of high-performance electronic devices over the past decades. Up to now, the improvement of the electronic chips' speed and density has mainly been realized through a reduction of the size. However, the size of the existing electronic components can not be decreased indefinitely. When the system's dimensions become comparable to the electrons' characteristic lengths, *i.e.* at the *mesoscopic* scale [50], new transport regimes appear. When such regimes are entered, the well-known macroscopic transport laws are no longer applicable. To further reduce the devices' size, a new generation of electronic sytems that take advantage of these mesoscopic properties of the carrier needs to be developed. Several possibilities have already been considered including, e.g., quantum computing [14], spintronics [162, 204, 214] or molecular electronics [105, 106, 170]. Within this context, a clear understanding of the low-dimensional transport properties of electron systems is of major importance. This chapter first reviews the main transport characteristic lengths associated with the

carrier and the related transport regimes. Secondly, it presents the case of open quantum dots (QDs) that provide one of the most useful tools to study the specific case of coherent transport in a confined system.

2.2 Characteristic lengths and related regimes

2.2.1 Mean free path

2.2.1.1 Definition

In the previous chapter, we have seen that a metallic system can be described as a gas made of independent electrons with a mass m^*. In a real system, however, electrons are scatterred by the crystal defects and impurities as well as by the phonons. Two different types of scattering have to be distinguished: elastic scattering, which leaves the electron's energy unchanged, and inelastic scattering, which modifies the electron's energy. The electron momentum is randomized after a time τ_m, the momentum relaxation time. The mean free path l_m is the distance covered by an electron before its initial momentum is destroyed, and can be defined by

$$l_m = v_F \tau_m, \tag{2.1}$$

where v_F is the Fermi velocity[1]. From the Drude model, the momentum relaxation time can be related to the mobility μ using the following formula:

$$\mu = \frac{|e|\tau_m}{m^*}. \tag{2.2}$$

Combining Eq. (2.1), Eq. (2.2) and Eq. (1.18), it is possible to calculate the mean free path of the electrons in a 2D system from the longitudinal resistivity at $B = 0$. For example, in the case of the 2DES presented in Fig. 1.7, $\rho_{xx} = 150\ \Omega$/sq. at 0.4 K, equivalent to a mean free path $l_m = 2.3\ \mu$m. Several other techniques have been developed to measure l_m. However, all observables do not have the same sensitivity to the different scattering events and, as a consequence, do not provide the same value of l_m. As an example, values of l_m extracted from magnetic focusing peak amplitudes that are sensitive to both small angle and large angle scattering are found to be about two times smaller than values extracted from the mobility that is mostly affected by large angle scattering [179].

[1] $v_F = \frac{\hbar k_F}{m^*} = \frac{\hbar}{m^*}\sqrt{2\pi n_{2D}}$.

2.2.1.2 Ballistic transport

When the dimensions of a device are lowered below l_m, an electron experiences scattering events only at the boundaries of the device. The transport is referred as *ballistic* and the sample's resistance strongly depends on its shape.

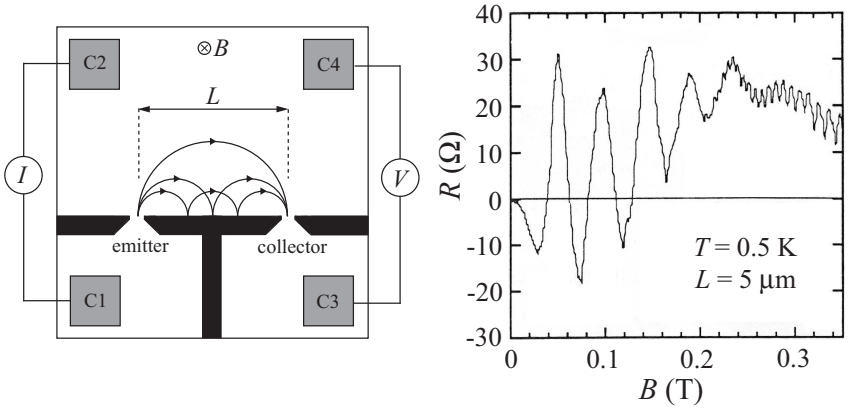

(a) (b)

Figure 2.1: (a) Schematic representation of a four-contact transverse magnetic focusing device. (b) Magnetoresistance at $T = 0.5$ K of a transverse magnetic focusing device with $L = 5$ μm and realized in a GaAs 2DHS with $p = 4.5 \times 10^{15}$ m^{-2}. Above $B \sim 0.2$ T, Shubnikov-de Haas oscillations are superimposed on the focusing peaks (from Ref. [92]).

One experiment that nicely illustrates the ballistic behaviour of electrons in low dimensional systems is the transverse magnetic focusing [191, 179, 140, 141]. Let's consider the device presented in Fig. 2.1(a). Starting from a 2DES, two constrictions separated by a distance $L \lesssim l_m$ are defined (the black areas are the zones where the 2D carrier system is depleted). A current I_{C1C2} is applied between the contacts C1 and C2. Through the Lorentz force, a magnetic field drives the carriers into a circular motion. When L is a integer multiple of the cyclotron diameter, the carriers that flow from the emitter are focused into the collector, eventually after several bounces on the device's boundary. In such configuration, a peak is observed in the voltage drop V_{C3C4} measured between contacts C3 and C4. The measurement of such peaks is shown as a function of B in Fig. 2.1(b) for a device with $L = 5$ μm realized on a 2DHS. The resistance is defined as $R = V_{C3C4}/I_{C1C2}$ and is measured at $T = 0.5$ K. A clear series of periodic oscillations of R, corresponding to

the magnetic focusing of the hole beam from the emitter to the collector, are observed and establish that ballistic transport of holes is achieved in this system.

2.2.2 Phase coherence length

2.2.2.1 Definition

Ballistic transport highlights the corpuscular behaviour of electrons. However, the quantum nature of electrons implies that they do not only behave as particles but also as waves. One consequence of the wavelike characteristic of electrons is that they carry a phase. In analogy with the momentum, the electron phase can be randomized by scattering events. Nevertheless, the phase is only sensitive to inelastic scattering, including electron-phonon scattering, electron-electron interaction and scattering by impurities with an internal degree of freedom like magnetic impurities. The timecsale over which the memory of the original phase of the electron is kept is the dephasing time[2] τ_ϕ. The distance covered by an electron before it loses its phase is the phase coherence length l_ϕ and is given by

$$l_\phi = v_F \tau_\phi, \tag{2.3}$$

if $\tau_m \approx \tau_\phi$. However, in disordered 2D systems at low T, when electron-phonon scattering is negligible, τ_ϕ can be substantially larger than τ_m. In this case, l_ϕ is given by

$$l_\phi = \sqrt{D\tau_\phi}, \tag{2.4}$$

where $D = v_F^2 \tau_m/2$ is the diffusion coefficient.

2.2.2.2 Coherent transport

If the size of a device is comparable to l_ϕ, the electron phase inside the system is preserved and the different possible electron paths interfere with each other. The interference of the electron partial waves that travel along the different paths leads to a quantum correction to the system's conductivity. The transport is said to be *coherent*.

The quantum interference of electrons can be illustrated with the Aharonov-Bohm interferometer [4]. In this experiment, an electron beam is split in two paths that are then recombined in order to interfere. Concretely, this can be realized by applying an electrical current through a quantum ring [184, 195, 196] as shown in the inset of Fig. 2.2. The

[2]The dephasing time τ_ϕ is also known as the coherence time.

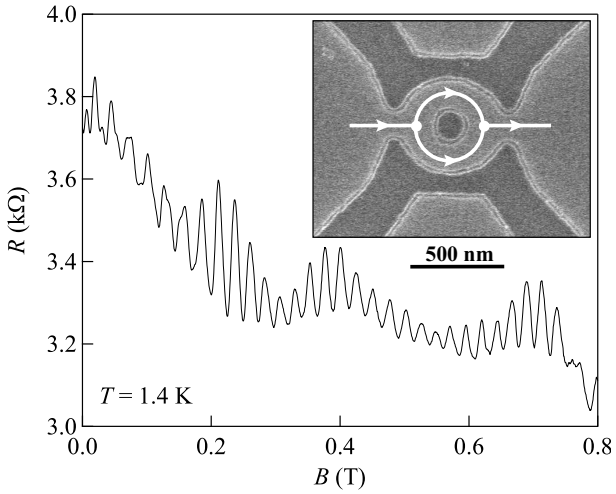

Figure 2.2: Aharonov-Bohm oscillations of the magnetoresistance of a quantum ring realized in a InGaAs 2DES with $n_{2D} = 1.6 \times 10^{16}$ m^{-2}. Measurements are performed at $T = 1.4$ K. Inset: SEM image of the quantum ring with a schematic representation of the carrier trajectories. The dark areas are the etched regions where the 2DES has been depleted. Courtesy of B. Hackens.

electrical current flowing through the ring is split between the two arms. The two different paths are recombined at the output of the ring where the electron partial waves interfere. If a magnetic field is applied perpendicular to the plane of the ring, the phase accumulated by electrons along the two arms of the device are shifted by $\Delta\varphi$ from each other, with

$$\Delta\varphi = \frac{2\pi|e|BA}{h}, \tag{2.5}$$

where A is the area of the ring. When the magnetic field is swept, the interference at the exit of the ring is then alternatively tuned from constructive to destructive. Consequently, the quantum correction to the resistance of the ring oscillates periodically as a function of B, as presented in Fig. 2.2.

2.2.3 Fermi wavelength

The wavelength of electrons at the Fermi level λ_F, is inversely proportional to the electron density. In a 2DES, λ_F is given by

$$\lambda_F = \sqrt{\frac{2\pi}{n_{2D}}}. \tag{2.6}$$

When one dimension of a metallic system is comparable to λ_F, the quantification of the energy into discrete levels along this particular direction becomes effective, *i.e.* only a few number of energy levels remain populated. However, similar to the case of the LLs (see Section 1.3.3), an additional condition has to be fulfilled in order to observe well resolved discrete energy levels: their separation in energy must be larger than their broadening given by h/τ_m and k_BT.

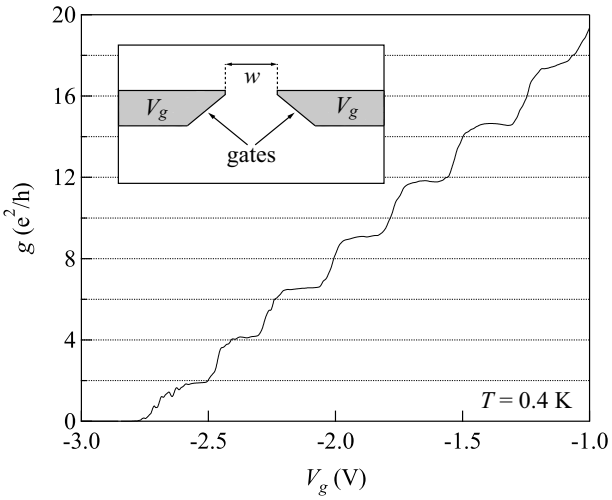

Figure 2.3: Conductance g as a function of the gate voltage V_g at 0.4 K of a quantum point contact realized in a GaAs 2DES with an electron density of $n_{2D} = 2.3 \times 10^{15}$ m^{-2}. Inset: Schematic representation of the quantum point contact. The shaded areas represent the metallic gates deposited on top of the sample; these gates are used to deplete the 2DES beneath them. The lithographic width of the constriction is $w = 0.4$ μm.

The discreteness of the electron energy spectrum in confined systems can be evidenced by electrical transport measurements performed through a quantum point contact (QPC) [192, 193]. A QPC is a narrow constriction realized by laterally confining a 2DES by means, for example, of metallic top gates. Such a device is schematically represented in the inset of Fig. 2.3. By applying a negative voltage V_g to the top gates, it is possible to deplete the zone of the 2DES that lies underneath the gates. The 2DES is then confined to a narrow one-dimensional (1D) channel. If the width w of the constriction is comparable to λ_F and the additional condition exposed above is satisfied, the 1D electrical subbands in the channel are resolved. Provided that the system is ballistic and that the electrical transport through the constriction is adiabatic,

meaning that electrons can not be transferred between two different subbands, the conductance g of the 1D channel is given by [50],

$$g = \frac{2e^2}{h} MT, \tag{2.7}$$

where the M is the number of subbands (or modes) populated in the 1D channel and T is the average probability for an electron to be transmitted through the constriction. If the gate voltage is further decreased, the extent of the depletion zone increases and w is reduced. As a result, sweeping down V_g depopulates in turn the 1D subbands in the constriction. The conductance as a function of V_g of a QPC is shown in Fig. 2.3. The successive depopulation of the different modes in the constriction when V_g is decreased leads to jumps of $\sim 2e^2/h$ in the QPC's conductance.

2.3 Open quantum dots

2.3.1 Description

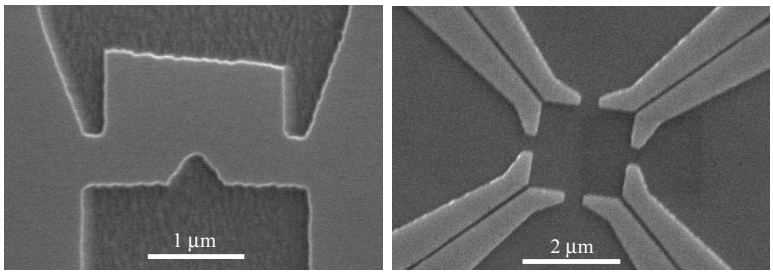

(a) (b)

Figure 2.4: (a) SEM image of an open QD realized by wet etching. The dark areas are the etched regions. (b) SEM image of an open QD defined with Ti/Au top gates (light area).

Open QDs are micrometer-sized cavities connected to electron reservoirs by two QPC leads with at least one mode populated. They are built from high-mobility heterostructures, so that, at low T, the electrical transport inside the cavity is both ballistic and coherent. Starting from a 2DES, the electrons can be laterally confined to a cavity by means of etching or using top gates. Figure 2.3 shows two examples. Open QDs defined by top gates have the advantage that, by adjusting the voltages applied on the different gates, it is possible to independently control the

dot's surface and shape as well as the number of modes in the QPC leads. For an etched QD, on the other hand, a top gate covering the entire device can be added. In this configuration, the gate voltage modifies the electron density in the cavity and the number of modes in the QPC leads at the same time.

2.3.2 Magnetoconductance of open quantum dots

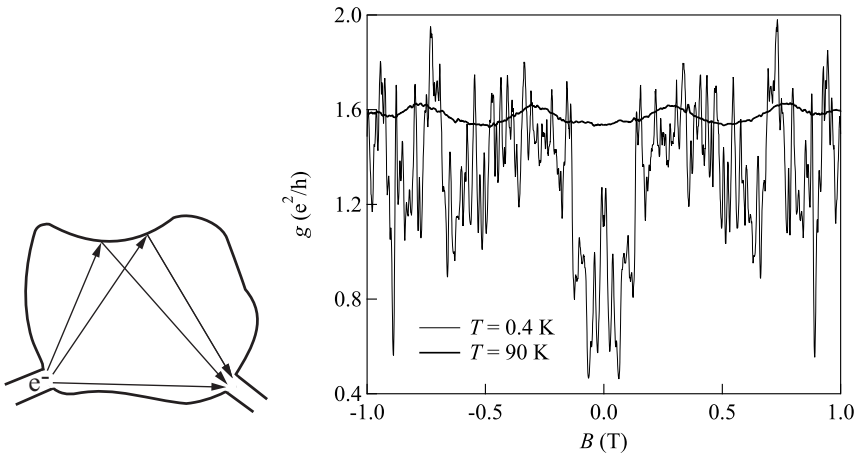

(a) (b)

Figure 2.5: (a) Carrier trajectories in a ballistic open quantum dot. (b) Magnetoconductance of a 0.5 μm^2 circular quantum dot built from an InGaAs 2DES with $n_{2D} = 1 \times 10^{16}$ m^{-2} at two different temperatures. Courtesy of B. Hackens.

2.3.2.1 Magnetoconductance fluctuations

The conductance g of an open QD is presented in Fig. 2.5(b) as function of B. At low T (0.4 K), the magnetoconductance shows a rich spectrum of fluctuations that are reproducible and symmetric with respect to $B = 0$ [129]. The behaviour of the electrons inside the cavity is schematically represented in Fig. 2.5(a). When an electron enters the QD in one lead, several different paths are possible to reach the second lead. If the two-terminal QD is both in the ballistic and coherent regimes, the different electron paths are only scattered at the boundaries

of the cavity[3] and interfere at the exit lead. Just like in a quantum ring, a magnetic field applied perpendicular the plane of the device changes the phase accumulated by the different electron paths and, as a result, modifies the interference at the exit of the QD. However, contrary to the case of the quantum ring, the different electron trajectories in a QD do not enclose identical magnetic fluxes. Consequently, the pattern of the magnetoconductance fluctuations (MCFs) is aperiodic. The shape of the MCFs pattern is determined by the QD's geometry as well as by the disorder potential in the cavity.

The different trajectories inside the QD, through the area they enclose, directly determine the shape of the MCFs pattern. The MCFs should then be a sensitive tool to study the electron dynamics inside the cavity. Classicaly, the dynamics of a ball moving ballistically, with specular bounces at the border in a given system is determined by the geometry of this system. One needs to distinguish between the chaotic and regular dynamics. The dynamics is said to be chaotic if the system behaviour is random, *i.e.*, is exponentially sensitive to the initial conditions. In this case, the ball probes the system in an ergodic fashion (it goes everywhere in the system) before it exits. Quantum systems like ballistic open QDs have been proposed to be excellent candidates to study the quantum manifestations of classical dynamics [102]. In this context, several statistical properties, like the electron escape rate or the spectral behaviour of the MCFs, have been predicted to differ for systems exhibiting regular vs chaotic dynamics [5, 17, 102, 103, 116]. Some of these predictions have been verified experimentally for QDs with chaotic and regular geometries [128, 129, 130]. However, it has been shown that, in real QDs, both regular and chaotic regions always coexist independently of their geometries [6, 44].

2.3.2.2 Magnetoconductance background

Figure 2.5(b) also shows a magnetoconductance trace measured at higher T (90 K). At this T, thanks to the reduction of the electron dephasing time, the MCFs disappear and only the slowly varying background remains. The mean conductance of the background is determined by the number of modes populated in the QPC leads. The slowly varying pattern is generated by the ballistic trajectories inside the cavity. As an example, for the particular case of the QD's conductance shown in Fig. 2.5(b), the oscillations observed at 90 K can clearly be ascribed to magnetic focusing from one QPC lead to the other (see Ref. [85]).

[3] By analogy to the macroscopic case, open QDs are also known as quantum billiards.

2.3.2.3 Weak (anti)-localization

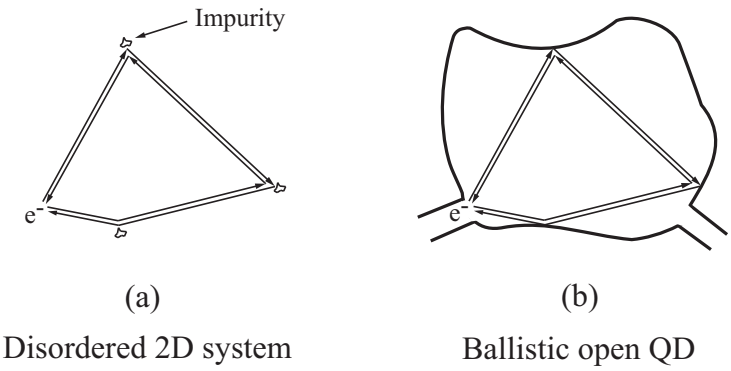

Figure 2.6: Schematic representation of the carrier trajectories travelling in opposite directions leading to coherent backscattering for (a) a 2D disordered system and (b) a ballistic open quantum dot.

The weak localization (WL) is a coherent effect that leads to a quantum correction to the conductivity. In two dimensions, WL was first predicted and observed in disordered systems [1, 23, 118]. If one considers an electron moving in a 2D disordered system, there are some trajectories that bring the electron back to its initial position after several scattering events (Fig. 2.6(a)). For each of these trajectories, there's a possibility for the electron to propagate on the same path but in the opposite direction. As these two paths are identical, the phase accumulated by the electron partial waves along the opposite directions are the same (time reversal symmetry). As a result, the pairs of paths propagating in opposite directions always interfere constructively. Therefore, it can be shown that in a quantum system the probability for an electron to be backscattered to its original position is twice as large as in a classical diffusion consideration. This enhanced coherent backscattering reduces the classical conductivity by a factor $\Delta\sigma$, given by [50],

$$\Delta\sigma = -\frac{e^2}{\pi h} \ln\left(\frac{\tau_\phi}{\tau_m}\right). \tag{2.8}$$

Once a magnetic field is applied perpendicular the 2DES, the phases acquired by electron along opposite direction paths are shifted with respect to each other and the time reversal symmetry is broken. The magnetoconductance of a disordered 2DES shows a dip around $B = 0$. For an arbitrary value of B, the quantum correction to the conductivity $\Delta\sigma$

is [11, 23]

$$\Delta\sigma(B) = -\frac{e^2}{\pi h}\left(\ln\left(\frac{B_\phi}{B}\right) - \Psi\left(\frac{1}{2}+\frac{B_\phi}{B}\right)\right), \tag{2.9}$$

where $B_\phi = \hbar/(4eD\tau_\phi)$ and Ψ is the Digamma function. The WL correction to the conductivity $\Delta\sigma$ is correct if the spin-orbit interaction is negligible. In the presence of strong spin-orbit coupling, *i.e.*, if the spin-orbit scattering time τ_{so} is much smaller than τ_ϕ, the two complementary waves propagating in opposite directions lose the memory of their initial spin. It can be shown that, in this case, the quantum correction to the conductivity at $B = 0$ has a reverse sign and is two times smaller than that given by Eq. (2.9) [21, 22]. One then speaks about weak anti-localization (WAL). In the absence of magnetic impurity scattering, the WAL correction to the magnetoconductivity is given by [93]

$$\Delta\sigma(B) = -\frac{e^2}{2\pi h}\left[\frac{3}{2}\Psi\left(\frac{1}{2}+\frac{B_2}{B}\right) - \frac{1}{2}\Psi\left(\frac{1}{2}+\frac{B_3}{B}\right) - \Psi\left(\frac{1}{2}+\frac{B_1}{B}\right)\right], \tag{2.10}$$

with

$$\begin{aligned} B_1 &= B_0 + B_{so}, \\ B_2 &= B_\phi + \tfrac{4}{3}B_{so}, \\ B_3 &= B_\phi, \end{aligned}$$

where $B_0 = \hbar/(4eD\tau_0)$, $B_{so} = \hbar/(4eD\tau_{so})$ and τ_0 is the elastic relaxation time[4]. It is worth noting that Eq. (2.10) is only valid for weak spin-orbit interaction, in the sense that $\tau_{so} > \tau_m$. Several improvements of the theory have been developed for arbitrary values of τ_{so} (see Refs. [112, 123, 134]). As an illustration, Fig. 2.7 shows the transition from WL to WAL with the increase of spin-orbit interaction. The curves were calculated from Eq. (2.10).

The WL and WAL effects described above for disordered 2DES can be transposed to open QDs. As sketched in Fig. 2.6, similar closed loop trajectories can exist in a ballistic quantum dot where the scattering by impurities or defects is replaced by boundary scattering. The observation of the WL/WAL correction to the conducivity, however, is more difficult in QDs than in 2DES (see Fig. 2.5(b)). Indeed, the magnetoconductivity of an open QD presents a second quantum correction, namely the

[4] If one consider a system where electron-phonon can be neglected (for example at low T), then $\tau_0 \sim \tau_m$.

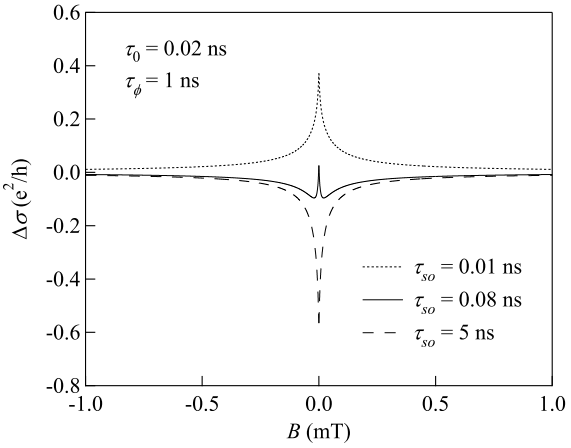

Figure 2.7: Weak (anti)localization correction to the conductivity for a 2DES with $n_{2D} = 2 \times 10^{15}$ m^{-2}, $\tau_0 = 0.02$ ns and $\tau_\phi = 1$ ns. Traces were calculated from Eq. (2.10) with $\tau_{so} = 5,\ 0.08$ and 0.01 ns.

MCFs. The superposition of the MCFs and the WL/WAL correction to the conducivity makes the quantiative analysis or even the observation of WL/WAL extremely difficult. Fortunately, contrary to the MCFs, the WL/WAL correction to the conducivity does not depend on the shape of the QD or on the disorder potential in the cavity. This particular property can be used to isolate the WL/WAL correction to the conductivity from the MCFs. For example, by differently adjusting the gate voltages of a gate-defined QD, its shape can be distorted while its area is kept constant. The WL/WAL correction to the conductivity is extracted by averaging the magnetoconductivity traces obtained for each shape of the QD (see Fig. 2.8) [98, 213]. It is worth noting here that the independence of the WL/WAL effect on the QD's shape is valid if one assumes that the electron dynamics in the QD is fully chaotic. It has been argued that the exact shape of the WL peak in the magnetoresistance of an open QD could probe whether the electron dynamics inside the cavity is either regular or chaotic [15, 27, 37].

2.4 The random matrix theory

The random matrix theory (RMT) is based on an idea introduced by Wigner in the 1950s, and was developed in the 1960s by Dyson, Mehta and Gaudin to describe the spectral properties of heavy nuclei [133, 157].

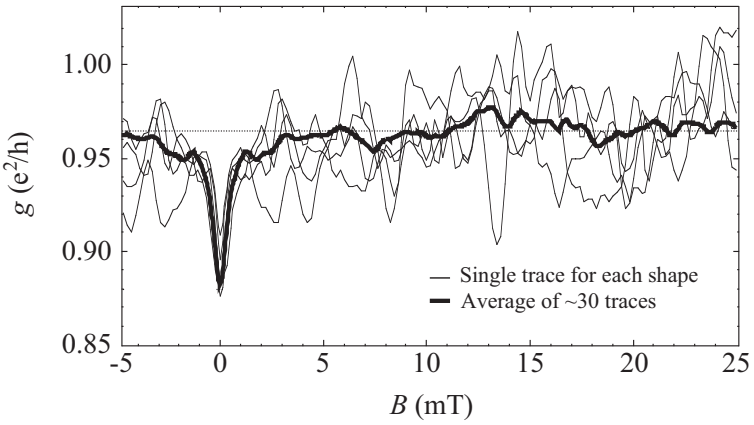

Figure 2.8: Magnetoconductances of an electron open QD for different shapes adjusted by means of top gates. The bold trace shows the averaged magnetoconductance for 30 independent shapes in order to isolate the WL/WAL correction to the magnetoconductivity (from Ref. [96]).

The main concept of the RMT is that the particular features that determine the microscopic hamiltonian governing the evolution of the system are ignored. Only the fundamental space-time symmetries of the system are kept to build a *random* hamiltonian that only provides universal information. Recently, an RMT of quantum transport has been developed for mesoscopic systems (for a review, see Refs. [8, 20]). This RMT was successfully applied to chaotic open QDs to predict their universal properties such as the mean conductance, the WL/WAL correction to the conductivity, and the variance of the MCFs.

Before providing the main results of the RMT for a ballistic open QD, it is worth noting the main assumptions and limitations introduced within this theory:

- The electron dynamics in the QD must be chaotic.
- The dwell-time τ_d must larger than the ergodic time τ_{erg}. In other words, the electron should probe the entire phase space ergodically[5].
- For most of the RMT's predictions, the number of modes in the QPC leads must be much larger than one.

[5]The dwell-time is $\tau_d = \frac{m^* A}{\hbar N}$, where A is the QD's area and N is the number of modes in the QPC leads. The ergodic time is given by $\tau_{erg} \simeq \frac{L^2}{v_F \min(l_m, L)}$, where L is the size of the QD.

For the properties of interest here, namely the WL correction to the conductivity δg^{WL} and the MCFs variance $var(g)$, the RMT predicts for a system at $T = 0$, with no spin-orbit interaction, [16]

$$\delta g^{\mathrm{WL}} = \frac{e^2}{h}\frac{N}{2N + N_\phi} \qquad N \geq 2, \tag{2.11}$$

and

$$var(g) = \frac{e^4}{h^2}\frac{N^2}{\left(\sqrt{4N^2 - 1} + N_\phi\right)} \qquad N \geq 2, B \neq 0, \tag{2.12}$$

where N is the total number of modes in the QPC leads. The number of modes N_ϕ in the fictitious ϕ-lead that is virtually added in order to account for the decoherence in the QD, writes as

$$N_\phi = \frac{2\pi\hbar}{\tau_\phi \Delta}, \tag{2.13}$$

with the spin-degenerate mean level spacing Δ given by

$$\Delta = \frac{2\pi\hbar^2}{m^* A}, \tag{2.14}$$

where A is the QD's area. In Refs. [30, 31], Brouwer et al. developed an extension of the ϕ-lead model that provides a more realistic description of dephasing processes in QDs and accounts for their spatial distribution.

At finite T, the electrons that contribute to electrical transport are spread out in energy around E_F. In this case, the QD's conductance is provided by a weighted average over the conductances of all the contributing energy states. This writes as [55]

$$g = -\int f'(E) g(E) dE, \tag{2.15}$$

where $f'(E)$ is the derivative of the Fermi-Dirac distribution. It can be shown that, as Eq. (2.15) is linear in g, the expression of δg^{WL} given in Eq. (2.11) is not affected by the thermal smearing, meaning that δg^{WL} depends on T only via τ_ϕ. The MCFs variance, on the other hand, is modified by T. When thermal smearing is included, the MCFs variance is provided by the following integration:

$$var(g) = \int_0^\infty \int_0^\infty f'(E) f'(E') cov(E, E') dE dE', \tag{2.16}$$

where the conductance correlation function $cov(E, E')$ reads as [55, 72]

$$cov(E, E') = \frac{\langle g \rangle^2}{(N + N_\phi)^2 + \frac{4\pi^2}{\Delta^2}(E - E')^2} \quad . \tag{2.17}$$

The equations presented above were formulated for QDs with no spin-orbit interaction and subjected to a strictly perpendicular magnetic field. Both the spin-orbit interaction and a parallel magnetic field, however, have been shown to significantly modify the statistical properties of a QD, such as δg^{WL} or $var(g)$. The spin-orbit interaction could tune the systems from WL to WAL as in a 2D disordered system [213]. It also reduces the variance of the MCFs by a maximum factor of 2 [88]. As for the parallel magnetic, it breaks time-reversal symmetry and, as a result, suppresses the WL/WAL correction to the conductivity [213]. Moreover, the parallel magnetic lifts the spin degeneracy through the Zeeman splitting and, consequently, reduces the MCFs variance [71, 88]. Recently, the RMT has been extended to account for the Zeeman splitting and for the spin-orbit interaction [7, 32, 43]. The spin-orbit interaction is introduced in the RMT as a perturbation through the spin-orbit scattering time τ_{so}. Eventual modifications of the band structure by the spin-orbit interaction are not included in the model. Moreover, this extension of the RMT is formulated for systems with $\tau_{so} \gg \tau_{erg}$. Within this extended RMT, the WL/WAL correction to the conductivity is given by the following equation [32]:

$$\delta g^{\mathrm{WL/WAL}} = -\frac{e^2}{h}\frac{N_1 N_2}{N_1 + N_2}\left[\frac{1}{N_C + 2a^2} + \frac{1}{N_C + 4a^2} - \frac{2a^2}{N_C(N_C + 2a^2) + 4b^2}\right], \tag{2.18}$$

where $N_{1,2}$ are the numbers of mode in the two QPCs. The parameters a, b and N_C are given by

$$a = \frac{2\pi\hbar}{\tau_{so}\Delta}, \tag{2.19}$$

$$b = \frac{\pi g \mu_B B}{\Delta}, \tag{2.20}$$

$$N_C = N_1 + N_2 + N_\phi + 2x^2, \tag{2.21}$$

with

$$x^2 = \frac{ce^2 L^4 B_\perp^2}{\hbar\tau_{erg}\Delta}. \tag{2.22}$$

where c is a numerical coefficient of order unity, L is the size of the QD, and $B_\perp$ is the perpendicular component of B. As for the conductance correlation function, it reads as [43]

$$cov(E, E') = \left(\frac{e^2}{h}\right)^2 \left(\frac{N_1 N_2}{N_1 + N_2}\right)^2 (V_C + V_D), \tag{2.23}$$

where the expressions of V_C and V_D can be found in Appendix A.

2.5 Dephasing time

As described in Section 2.2.2, the electron dephasing time is determined by the different inelastic scattering events. In a solid, the main mechanisms that induce decoherence are electron-phonon scattering, electron-electron interaction and inelastic impurity scattering. Note that external sources of scattering, such as RF radiation [97], can also lead to electron decoherence. The total dephasing time τ_ϕ can then be expressed as the sum of the different contributions using the Matthiessen rule,

$$\tau_\phi^{-1} = \frac{1}{\tau_{e-ph}} + \frac{1}{\tau_{EE}} + \frac{1}{\tau_{imp}} + ..., \tag{2.24}$$

where τ_{e-ph}^{-1}, τ_{EE}^{-1} and τ_{imp}^{-1} are the dephasing rates associated with electron-phonon, electron-electron and inelastic impurity scattering, respectively. The following sections succinctly introduce the dephasing mechanisms in 2D systems and open QDs. For a more complete review of dephasing in metal and semiconductor mesoscopic structures, see Ref. [120].

2.5.1 Dephasing in two-dimensional systems

Semiconductor heterostructures, fabricated using the MBE technique, are extremely clean systems where dephasing by inelastic impurities can be neglected. The only scattering mechanisms that are expected to induce decoherence in these systems are electron-phonon and electron-electron interaction.

At high T, decoherence is generally dominated by electron-phonon interaction. In GaAs 2D systems, for $T \gtrsim 30$ K, interaction of electrons with longitudinal optical phonons is prominent [172, 205]. When T is decreased, this mechanism is exponentially reduced and, below 1 K, the electron-phonon interaction is dominated by the piezoelectric coupling of electrons with acoustic phonons. At sub-Kelvin temperatures, the electron-phonon scattering time τ_{e-ph} has a T^{-3} dependence [136, 198].

However, at few Kelvin temperatures, the dephasing time is mainly determined by electron-electron interaction, which is made of two different contributions. One must distinguish between the large energy transfer scattering mechanisms and small, quasi-elastic energy transfer (Nyquist) scattering mechanisms with the corresponding dephasing times, τ_{ee} and $\tau_{\phi N}$, respectively. The former mechanism corresponds to the timescale over which the excess energy of an electron excited above the Fermi level is relaxed through electron-electron interaction, while, the latter, the Nyquist mechanism, arises from the interaction of an electron with the fluctuations of the electromagnetic background stemming from the thermal motion of the other electrons. Within the Fermi liquid theory, the dephasing rates associated with these mechanisms in 2D disordered systems write as [9, 73, 98, 211]

$$\tau_{ee}^{-1} = \frac{\pi}{4}\frac{(k_B T)^2}{\hbar E_F}\ln\frac{E_F}{k_B T}, \tag{2.25}$$

$$\tau_{\phi N}^{-1} = \frac{k_B T}{2\pi\hbar}\frac{\lambda_F}{l_e}\ln\frac{\pi l_e}{\lambda_F}, \tag{2.26}$$

where l_e the elastic mean free path. Measurements of τ_ϕ in 2D systems at low T, mainly performed through the analysis of WL, were found to be in good agreement with these theoretical predictions [39].

2.5.2 Dephasing in open quantum dots

The analysis of the signatures of coherent transport in open QDs, such as WL and MCFs, provided a measure of the dephasing time. Most experimental studies were performed on GaAs systems. Several techniques, including the RMT, have been used to analyse the magneto-transport data and have provided results in good agreement with each other [120]. The experimental investigations were performed below 4 K, where the coherence length is comparable to the dots' size, and where the WL correction to the conductivity and the MCFs can be measured. In this T range, the decoherence is dominated by electron-electron interaction and τ_ϕ exhibits a power law scaling with the temperature, $\tau_\phi \propto T^{-\alpha}$, where α generally lies between 1 and 2 [85, 98, 213]. Only few theoretical predictions have been developed for τ_ϕ in open QDs. Takane [181] considered Coulomb interaction in ballistic chaotic quantum dots and calculated the dephasing time for QDs with a width of QPC leads w much larger than λ_F:

$$\tau_\phi^{-1} \sim \frac{\lambda_F}{w}\frac{k_B T}{\hbar}. \tag{2.27}$$

Sivan *et al.* [178] considered electron-electron scattering in disordered QDs and predicted a T^{-2} dependence for τ_ϕ. Interestingly, the behaviour of τ_ϕ in ballistic open QDs was found to be well described by the Fermi liquid theory developed for disordered 2D systems (Eq. (2.25) and Eq. (2.26)) [85, 98].

The most surprising aspect of decoherence in open QDs is the unexpected low T saturation of τ_ϕ [24, 40, 86, 156, 161]. Within the conventional Fermi liquid theory, the electron coherence time is expected to become infinite when $T \to 0$ if only electron-electron or electron-phonon interactions are taken into account[6]. Several conjectures have been proposed to explain this intriguing behaviour, including transition to zero-dimensional behaviour [24, 156] or unintentional RF radiation [97], but they were unvalidated experimentally. The importance of geometrical factors like the coupling to the reservoirs was first pointed out by Bird and coworkers [26, 59]. Indeed, the dephasing time was found to be larger for *almost* closed QDs. Moreover, the dephasing time in closed quantum dots, with less than one mode in the QPC leads and coupled to the reservoirs through electron tunneling, was found to be strongly enhanced in comparison to open QDs [56]. Recently, Hackens *et al.* [86] showed that the saturation value of τ_ϕ could possibly be determined by the QDs' dwell-time τ_d that depends on the dot's area and on the number of modes in the QPC leads.

[6]Decoherence due to dilute magnetic impurities has been proposed to explain the low-T saturation of τ_ϕ in metal films and wires. However, this argument cannot be invoked in clean semiconductor structures.

Chapter 3

Hole open quantum dots

> Tout obstacle renforce la détermination. Celui qui s'est fixé un but n'en change pas.
>
> *Léonard de Vinci*

3.1 Introduction

Mesoscopic systems have attracted considerable interest over the past decades since they are a potential source for novel generations of electronic devices. Within this context, semiconductor QDs have emerged as unique confined systems for studying spin phenomena and carriers' properties such as characteristic transport times. Several research groups have focused on dephasing time τ_ϕ and the spin-orbit relaxation time τ_{so} for electrons in quantum wires and QDs [120] for different materials including GaAs [24, 40, 84, 98] and InGaAs [85, 86]. Up to now, only few studies have been carried out on p-type nanostructures [82, 121, 167, 206, 208] because they are hard to realize and also because their experimental study is made difficult by the small amplitude of the holes' quantum interference effects.

This chapter first presents the fabrication process we employed for the realization of p-type GaAs open QDs. Second, it shows the magnetotransport measurements performed on our hole QDs that display both MCFs and WAL for T below ~ 500 mK. From these measurements, we deduce a T-dependence for τ_ϕ together with an upper limit for τ_{so} using the RMT. We compare the values obtained for these transport times with existing theories and with values obtained for electrons in similar QDs and for holes in 2D systems [62].

3.2 Fabrication and characterization

The lateral confinement of a 2D carrier system to a submicron cavity can be performed by means of top gates or by etching. While the top gate technique is much more flexible, in the sense that it allows to independently control several QD's parameters such as its shape, its size or the population of the QPC leads, we realized our hole QDs using the etching technique. This choice was motivated by two reasons. First, the hole QDs fabricated by means of top gates exhibit extremely noisy magnetoconductance traces, most probably resulting from the presence of switching impurities in the doped layer [153]. Under these conditions, the observation of signatures of coherent transport in the conductance measurements was impossible. Second, the combination of an etched QD with a top gate covering the entire device allows us to control the shape of the vertical confining potential and, consequently, to tune the SIA contribution to the spin-orbit interaction. The production of such nanostructures with controlable spin-orbit interaction is of particular interest for the emerging field of spintronics. Beyond the confinement of the 2D carrier systems to a cavity, the fabrication of a QD sample also requires the realization of electrical connections to the macroscopic measurement system. These connections are realized by patterning a Hall bar and ohmic contacts on the 2D hole system. The complete fabrication process of hole QDs samples then consists of four fabrication steps, including the realization of the ohmic contacts, the Hall bar patterning, the QD's definition, and the top gate deposition. Each fabrication step is performed by applying a particular treatment to a selected area of the sample's surface. The definition of the surface area that has to be modified in each process step is done using electron beam (e-beam) lithography. The e-beam lithography, as well as the method used to transfer the design to the substrate, are described in the following section.

3.2.1 Surface patterning

3.2.1.1 Electron beam lithography

Electron beam lithography [165] is a technique that allows the creation of extremely fine designs (resolution $\lesssim 10$ nm) on the sample's surface. The principle of e-beam lithography is schematically represented in Fig. 3.1:

- An electron sensitive resist is deposited on the substrate.
- The patterns are exposed by means of an electron beam.

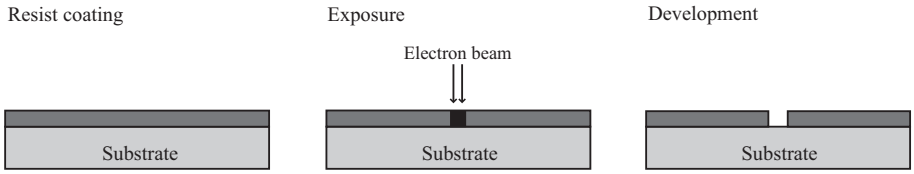

Figure 3.1: Schematic representation of the electronic lithography process.

- The exposed-unexposed areas are selectively dissolved in a developer solution.

The usual resists used for e-beam lithography are electron sensitive polymers dissolved in a liquid solvent. They are first deposited on the sample's surface by spin-coating and baked out in order to remove the solvent. The electron beam that is swept on the sample's surface following the chosen design, locally modifies the chemical structure of the resist making the exposed area more (or less) soluble in the developer solution. If the exposed (unexposed) area is dissolved and the unexposed (exposed) area remains on the surface, the resist is said to be positive (negative).

The resist used in our fabrication process is a positive resist: polymethyl methacrylate (PMMA)[1]. The resist thickness is adapted depending on the process step. Two different thicknesses are used: $\sim$ 700 nm produced by spin-coating a solution of 6 % PMMA in chlorobenzene at 5000 rpm, and $\sim$ 180 nm produced by spin-coating a solution of 3 % PMMA in chlorobenzene at 6000 rpm. After the spin-coating step, the resist is baked for 10 minutes at 160°C on a hot plate to evaporate the solvent. Moreover, for the fabrication steps that require the definition of submicron patterns, e.g. the QD's definition, the resist is further baked overnight at 140°C in an oven in order to relax the stresses that appear during the spin-coating process.

The resist exposure is performed in a modified SEM that consists in a Philips XL30 SEM-FEG with a Raith Elphy Plus hardware module that controls the beam blanker, the deflecting lens and the laser interferometer stage. The beam blanker is used to correctly adjust the electron dose sent to a particular area of the sample's surface and to protect the resist when the beam is deflected above areas that do not need to be

[1]The PMMA resist used here is a standard product from MicroChem Corp., Newton, MA 02464, USA. This resist has a molecular weight of 950 000 and is dissolved in chlorobenzene. Note also that above a critical electron exposure dose of ~ 3.5 mC/cm^2, PMMA turns into a negative resist.

Exp. type	Magn.	Stitching	Dose (μC/cm^2)	I_{beam} (pA)	d (nm)	t (μs)
Large field	$\times$400	yes	250	670	16	1.01
QD	$\times$2000	no	190	25	4	1.2

Table 3.1: Typical e-beam lithography parameters for the exposure of large patterns and QDs. The magnifications of $\times$400 and $\times$2000 correspond to exposure fields of 216 and 45 μm, respectively. The parameter d is the distance between two exposed pixels, while t is the exposure time corresponding to one single pixel. Note that d is always adjusted to provide a value of t as close as possible to the hardware limit of 1 μs.

exposed. Note that the optimal electron dose for the PMMA resist used here was found to be around 190 μC/cm^2 on a GaAs substrate. Using the laser interferometer stage equipped with stepping and piezoelectric motors, the sample's position can be changed with an accuracy of $\sim$ 4 nm. This allows the definition of patterns much larger than the exposure field accessible from the SEM at a given magnification. This is done by cutting out the total design and exposing it part by part after displacements of the sample (stitching exposure). Using the stitching exposure technique, it is possible to define large patterns without loss of resolution and without exposure field deformation that are unavoidable when working at low SEM magnification.

The resist exposure is always performed with an acceleration voltage of 30 kV in order to reduce the proximity effect, while the magnification and the e-beam current were adjusted depending on needed resolution and pattern size. In our fabrication process, we use two different conditions for e-beam lithography. For the patterning of large areas that does not require high resolution, we combine a thick layer of PMMA ($\sim$ 700 nm) with the stitching technique at a magnification of $\times$400. To ensure a good overlap of the areas exposed in the different stitching exposure fields, the designs are a bit overexposed at a dose of 250 μC/cm^2. On the other hand, for the exposure of the QD, which requires a higher resolution, the lithography was performed at a magnification of $\times$2000 using a 180 nm thick layer of PMMA. For this particular step, we determine the optimal dose for the device's exposure by making a test on a bulk sample. Indeed, due to the proximity effect, the optimal dose can slightly vary for devices with different geometries. The optimal dose is generally close to 190 μC/cm^2. The detailed values of the e-beam lithography parameters for the two types of exposures described above are presented in Table 3.1.

The development of the exposed area was done by immersing the sample in a solution of 1/3 methylisobutylketone/isopropanol for 1 minute and 30 seconds. After the development, the sample is rinsed for 30 seconds in isopropanol and 5 minutes in water. Finally, it was dried using nitrogen.

Once the e-beam lithography step is finished, the PMMA patterns present on the sample's surface have to be transfered to the substrate. This can be done in two ways: by metallization/lift-off or by etching. These two techniques are described below.

3.2.1.2 Metallization/lift-off

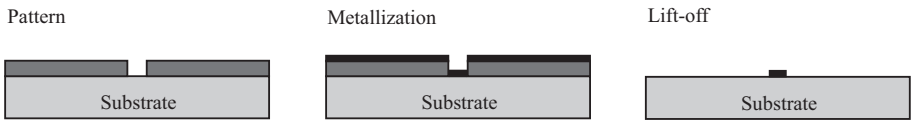

Figure 3.2: Schematic representation of the pattern transfer by metallization and lift-off.

The metallization/lift-off technique is schematically represented in Fig. 3.2. After the e-beam lithography step, a metallic layer is deposited on the entire sample. By immersing the metallized sample in a solvent, the resist is dissolved and the metal deposited on the resist is lifted-off from the surface. The metal remains only in the areas that were uncovered during the development step.

The metallic layer is generally deposited by evaporation in an e-beam metallizer. This technique provides a highly directional deposition of the metal that precludes any metal deposition on the lateral side of the resist and, consequently, ensures an easier lift-off. Also, in order to make the lift-off step easier the metal thickness is generally kept below 1/3 of the resist's thickness. Finally, when depositing metals with high evaporation T, like Pt for example, care has to be taken not to heat the sample above the glass transition of the resist[2].

For our PMMA resist, the lift-off process is realized in an acetone bath. In order to help the lift-off, the acetone and the sample can be placed in an ultrasonic bath for a few seconds. Also, heating the acetone bath helps the dissolution of the PMMA resist.

[2]For the PMMA resist used here the glass transition occurs around 100°C.

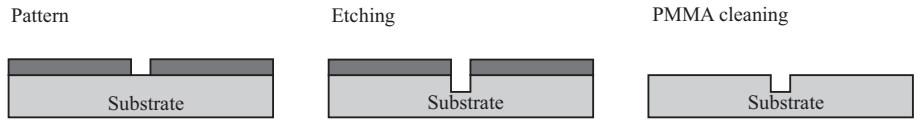

Figure 3.3: Schematic representation of the pattern transfer using an etching technique.

3.2.1.3 GaAs Etching

The pattern resulting from the lithography steps can be alternatively transferred to the substrate by etching the sample. If the etching rate ratio between the substrate and the resist is high, the resist protects the areas underneath and only the uncovered zones of the sample are etched. This process is represented in Fig. 3.3.

In order to etch our (311)A GaAs samples, we used a wet eching process. The liquid etchant was a 1/1/25 solution[3] of $H_3PO_4/H_2O_2/H_2O$. This solution leaves the PMMA intact but etches the (311)A GaAs at a rate of $\sim$ 120 nm/s at room T. The etchant operates by first oxidizing the GaAs substrate and then dissolving the oxide [201]. The hydrogen peroxide acts as oxidizing agent, while the phosporic acid dissolves the GaAs oxide. The phosporic acid solution was chosen instead of the usual sulphuric acid one [201] because it leads to better etching profiles for the particular case of (311)A GaAs wafer [92]. Once the sample has been etched to the desired depth, the process is halted by rinsing the sample in de-ionized water for 5 minutes. After the etching step, the resist mask can be removed by immersing the sample in boiling acetone for 5 minutes.

As the acid present in the etchant dissolves the GaAs oxide, one must be careful that the GaAs surface is not oxidized before the e-beam resist spin-coating. If it is the case, the solution will etch the sample under the resist mask. To avoid such underetching problem, a preparation step that removes the oxide layer from the GaAs surface is performed before spin-coating. To that purpose, the sample is immersed in a dilute solution of sulphuric acid (1/240 of H_2SO_4/H_2O) for 15 seconds and rinsed for 5 minutes in de-ionized water. The sample is then dried using nitrogen and degased overnight at 140°C under vacuum.

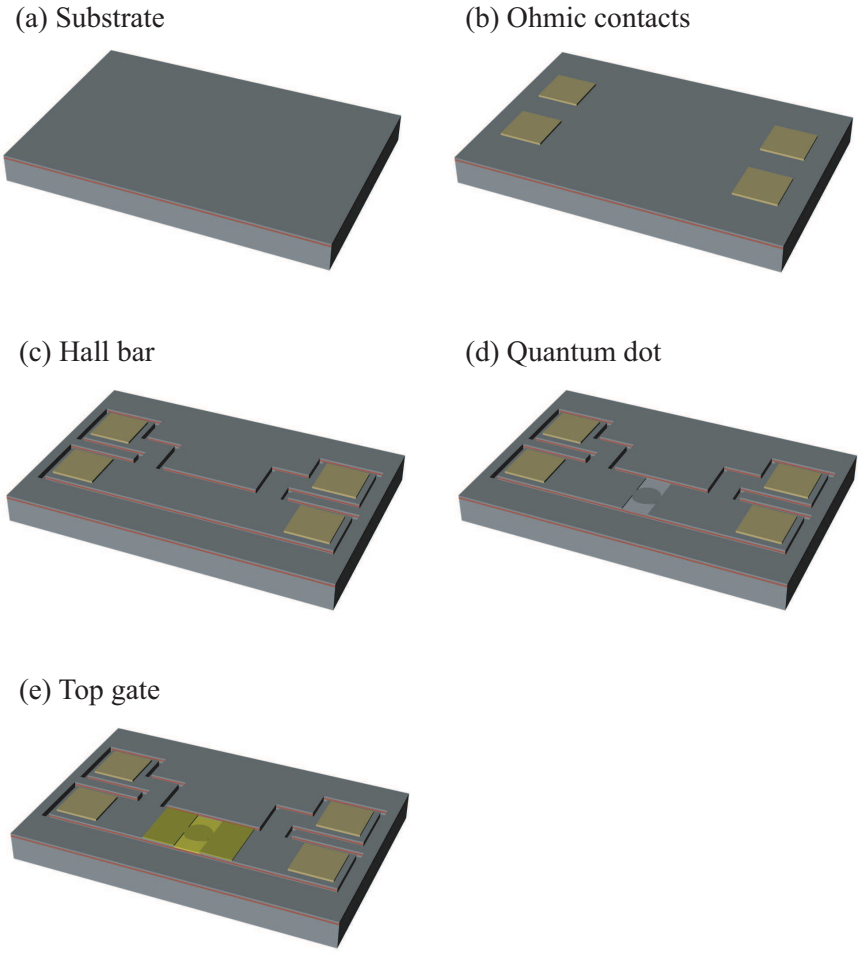

Figure 3.4: Schematic illustration of the fabrication steps for QDs, including the starting substrate (a), the realization of ohmic contacts (b), the Hall bar (c) patterning, the quantum dot definition (d) and the top gate deposition (e).

3.2.2 Fabrication Steps

After the description of the methods used to pattern the sample's surface, we present here the general fabrication steps that are performed in order to realize our open QDs. The detailed process sequence for the fabrication of the hole QDs samples can be found in Appendix B. The different fabrication steps as well as the sample's design are schematically illustrated in Fig. 3.4.

- **Standard cleaning**: The fabrication of submicron devices requires that the sample's surface remains perfectly clean and devoid of dust, impurities or residue from previous fabrication steps. To that purpose, the entire fabrication process was realized in UCL cleanrooms and each fabrication step was followed by standard sample cleaning. The standard cleaning consists of: 5 minutes in boiling trichlorethylene, 5 minutes in trichlorethylene and ultrasonic bath, 5 minutes in boiling acetone, 5 minutes in acetone and ultrasonic bath, and 5 minutes in methanol. After the cleaning sequence, the sample was dried with nitrogen.

- **Substrate**: The substrates for the fabrication of our QD samples are 3×3 mm^2 pieces of GaAs heterostructure. In order to make the sample handling easier, they are glued, after cleaning, on 2 inch Si wafers using carbon paint[4] that is hardened at 100°C for 10 minutes on a hot plate.

- **Ohmic contacts**: The first lithography followed by a metallization and lift-off step defines the ohmic contacts' pads (Fig. 3.4(b)). These metallic pads provide, after annealing, electrical connections to the 2D carrier system buried below the GaAs surface.

  For the particular case of our hole QD samples, they consist in 300×300 μm^2 metallic pads made of the following layer sequence: 13 nm of Ni, 30 nm of Be, 100 nm of Au, 15 nm of Ni, and 50 nm of Au. After the lift-off process, the sample is cleaned and a rapid thermal annealing at 450°C for 1 minute is realized in a reducing atmosphere (95%/5% of N_2/H_2). The first Ni layer ensures a good adhesion of the deposited metal to the GaAs substrate. During the annealing process, the Be atoms diffuse in the heterostructure and act as dopants by replacing the Ga atoms that move to the first

[3]The solution was prepared with phosphoric acid at a concentration of 85% and hydrogen peroxide at a concentration of 30%.

[4]The carbon paint is colloidal graphite in an isopropanol solution from Ted Pella, Inc., PO BOX 492477, Redding, CA96049-2477, USA.

Au layer [201]. The second Ni layer is used to avoid the diffusion of Be and Ga atoms to the topmost passivating Au layer.

The heavy doping of the GaAs and AlGaAs layers that lie between the metallic pads and the 2D hole system has two purposes [201]. First, it reduces the thickness of the Schottky barrier at the GaAs/metal interface. The reduction of the Schottky barrier strongly enhances the electron tunneling process and leads to an ohmic behaviour of the GaAs/metal interface. Second, the doping of the GaAs cap and AlGaAs spacer layers generates a conductive path from the metallic pads to the 2D hole system.

- **Hall bar**: Once the ohmic contacts are realized, we pattern the Hall bar that defines the current and voltage probes together with a 200 μm wide measurement area by laterally confining the 2D hole system (Fig. 3.4(c)). To realize the Hall bar, we perform a deep wet etching, in the sense that the heterostructure is etched beyond the 2D hole system. A small overlap between the edge of the Hall bar and the ohmic contacts is realized in order to avoid a Corbino geometry (see Fig. 3.5(a)).

- **Quantum dots**: The quantum dot, located inside the Hall bar, is also realized by laterally confining the 2D hole system using wet etching (Fig. 3.4(d)). However, to define the QD, we perform a shallow etch: the structure is only etched down to the doped layer. This technique ensures the depletion of the zones lying below the etched areas and keeps the surface states away from the QD. Moreover, the deformation of the lithographic pattern due to the anisotropic and lateral etching becomes less important.

- **Front gate**: After the QD definition, the metallic top gate is deposited on top of the QD and the Hall bar (Fig. 3.4(e)). The top gate covers the entire Hall bar, so that its effect on the hole density and vertical confining potential can be probed by Shubnikov-de Haas (SdH) and Hall measurements. For our samples, the metallic top gate is made of a 10 nm thick Ti adhesion layer and a 50 nm thick Pt layer.

An optical microscopy image of a finished QD sample is shown in Fig. 3.5(a). One can clearly distiguish the ohmic contacts, the Hall bar, the QDs areas and the top gate. In the corners of the sample, one can also observe the alignment marks used to obtained a perfect superposition of the different fabrication steps.

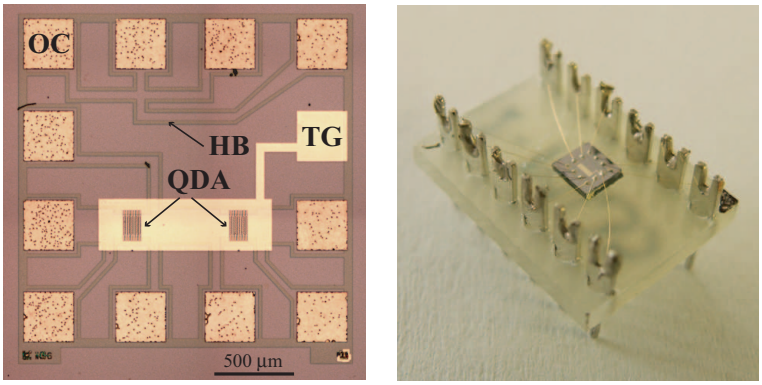

Figure 3.5: (a) Optical microscopy image of a QD array sample realized on a GaAs heterostructure. One can distinguish the ohmic contacts (OC), the Hall bar (HB), the QD arrays (QDA) and the top gate (TG). (b) Photograph of a sample mounted on a sample holder using gold wires and silver epoxy.

Once the fabrication process is over, the sample is mounted onto a sample holder[5] using vacuum grease as glue (Fig. 3.5(b)). The ohmic contact pads are connected to the sample holder's pins using gold wire with a diameter of 25 μm and an electrical conductive silver epoxy[6]. The silver epoxy is baked for 1 hour at 120°C.

3.2.3 Measurements

3.2.3.1 Cryogenic system

The magnetotransport measurements were performed in an Oxford Instrument Kelvinox 300 dilution refrigerator with a base temperature of $\sim$ 30 mK and equipped with a superconducting solenoid that generates a magnetic field up to 17 T. We use a home made stainless steel mixing chamber (MC) carrying a [porous Ag]/[Ag] cold finger[7]. The sample is

[5]The sample holders are glass epoxy component mounting boards from Wearnes Cambion LTD, Castleton, Hope Valley, Derbyshire, S33 8WE, England.

[6]We used EPO-TEX H31D silver epoxy from Epoxy Technology Inc., 14 Fortune Drive Billerica, MA 01821-3972, USA.

[7]Silver powder with 70 nm diameter particles was sintered on the cold finger to a packing fraction of $\sim$ 50% in order to increase the effective surface contact between the ^{3}He/^{4}He mixture and the Ag cold finger and enhance the heat transfer between these two materials. The Ag powder was packed at a pressure of $\sim$ 100 bars at room T and was subsequently baked out for 1 hour at 100°C in an inert atmosphere [166].

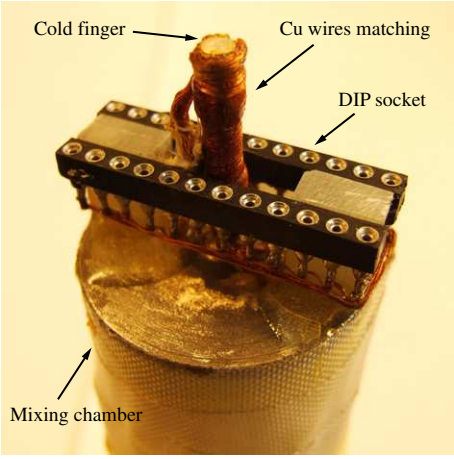

Figure 3.6: Photograph of the bottom of the mixing chamber.

mounted under vacuum on a dual in-line pin (DIP) socket fixed at the bottom of the MC, close to the cold finger (see Fig. 3.6). The sample is cooled via the Cu measurement wires which are thermally anchored onto the cold finger and the MC's body using 7031 General Electric (GE) varnish. The system temperature is determined using a RuO_2 thermometer thermally anchored to the cold finger. A resistive wire with a resistance of 500 Ω, matched in a non inductive way on the body of the mixing chamber, is used as heater.

In order to avoid system heating due to the ambient electromagnetic noise, low pass filters are placed on each measurement wire at the top of the refrigerator. The filters are an RLC circuit made of a 1kΩ resistor in series with a commercial LC component[8] containing a capacitance of 330 pF. The cutting frequency of the filters strongly depends on the sample's resistance. For lock-in amplifier frequencies below 15 Hz, the filters used here allow the measurements of samples with resistance up to 1 MΩ without attenuating the measurement signal.

The data obtained from the measurement apparatus located in a Faraday cage are transferred to the NanoFreeze acquisition program[9] via

The 70 nm Ag powder is commercially available from ULVAC Materials, Inc., 516 Yokota, Sammu-shi, Chiba-ken 289-1297, Japan.

[8]The LC filters were purchased from RS Component (stock n° 239-163).

[9]The NanoFreeze acquisition program was developped for the Wavemetrics Igor Pro software by Dr. Cédric Gustin. It provides a highly flexible data acquisition framework that controls the refrigerator status, the magnet source as well as the measurement apparatus through GPIB controllers.

a GPIB/ethernet controller. In order to electrically decouple the acquisition computer from the low-noise measurement system, the ethernet data transfer from the GPIB controller to the computer is performed using a wireless connection.

3.2.3.2 Electrical characterization

The conductance of the QDs was measured using a PAR 124A lock-in amplifier working at a frequency of 15 Hz and by applying a constant current of 1 nA to the sample. The measurement current was chosen to be as small as possible in order to avoid unwanted heating effects, but large enough to obtain a reasonable signal/noise ratio when measuring the MCFs and the WAL correction to the conductivity. A simple way to verify if the measurement current heats the sample is to reduce the current and check if the MCFs and the WAL peak amplitudes remains unchanged. In order to remove contributions from the measurement wires and directly access the resistance of the QDs, we use a four-terminal configuration measurement circuit. In our case, however, the configuration is not really four-terminal as we always measure a part of the Hall bar in series with the QD. Fortunately, the resistance added by the 2D hole system in the Hall bar is ~ 2 orders of magnitude smaller than the QD's resistance and, consequently, is negligible.

The magnetic field is generated by applying an electrical current to the superconducting solenoid located in the ^{4}He bath using an Oxford Instrument IPS120 magnet source. For the magnetotransport measurements performed on the hole open quantum dots, B was always applied strictly perpendicular to the plane of the 2D system. In order to properly measure the rich spectrum of MCFs, B was slowly swept at a rate of 10^{-4} T/s. Sweeping the magnetic field across $B = 0$ T strongly increases the MC temperature. In order to minimize the impact of this heating effect on the measurements, both the positive and negative B part of the magnetoconductance traces were taken by decreasing the absolute value of B and by lowering the B sweeping rate to 1.7×10^{-5} T/s below 0.09 T. As for the measurement of the WAL peak located around $B = 0$ T, it was performed at fixed B's, point by point. The magnetic field was swept to the different target fields at a rate of 3.4×10^{-5} T/s and the temperature was relaxed to the desired value before the conductance measurements. Moreover, for the particular case of the WAL peak, the conductance was calculated by averaging 30 different measurements in order to improve the signal/noise ratio.

At very low T, the hole-phonon coupling becomes weak and the holes' T can deviate from the T of the lattice and hence from the T given

by the thermometer. Below 150 mK, we then estimate the real T of the holes from an analysis of the SdH oscillations measured in the 2D hole system by correcting the effective T against linear fits to activation plots at integer filling factors (see Ref. [132]). Using this technique, the deviation of the effective holes' T from the MC's T was found to be around 10 mK at 100 mK, while the holes' real base T was determined to be ~ 70 mK.

3.3 Sample description

The samples were realized, using the fabrication process described above, from a p-type GaAs quantum well grown by molecular beam epitaxy on a (311)A wafer. The quantum well was grown at Princeton University in the group of Prof. M. Shayegan. A schematic layout of the quantum well structure can be found in Appendix C, where it is referred to as M439. The two-dimensional hole system has a density $p = 2.3 \times 10^{15}$ m^{-2} and a low-T mobility of 35 m^2/Vs, equivalent to a mean free path of 2.7 μm. The mobility quoted here was measured along the [$\bar{2}$33] high-μ direction.

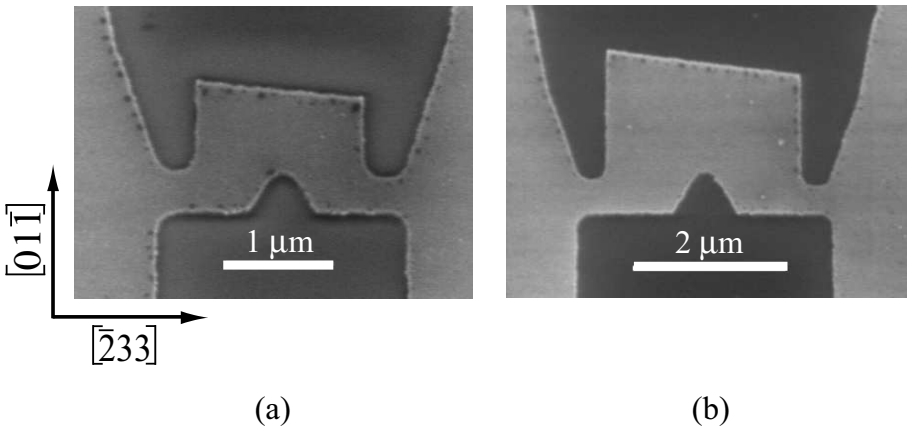

Figure 3.7: SEM images of (a) D1 and (b) D2. The orientation of the QDs with respect to the heterostructure's crystallographic axes is also shown.

Two different dots with similar shapes but different areas (1.4 μm^2 - D1 and 4.5 μm^2 - D2) were fabricated. The dots' areas were deduced from the lithographic dimensions and by taking into account the depletion regions, which were estimated from the effective width of the quantum point contacts, given by the number of modes entering the cavity. SEM

images of the two QDs are given in Fig. 3.7. The orientation of the QDs with respect to the heterostructure's crystallographic axes is also shown.

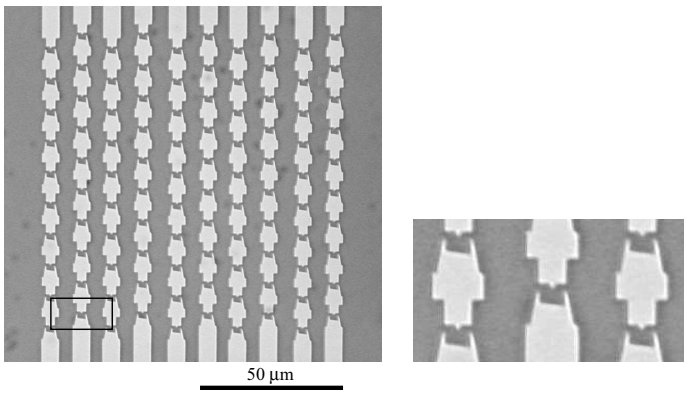

Figure 3.8: Image of a 10×10 array of QDs. The QDs are spaced by 10 μm. The picture has been taken after the e-beam lithography step.

In order to average out the MCFs and access the WAL correction to the conductivity [37, 98], we fabricated two additional samples made of arrays of 10×10 dots with cavities similar to D1 and D2. These samples are denoted as A1 and A2 for the smaller and the larger dots, respectively. A picture of a QDs array is presented in Fig. 3.9. The QDs of the array are arranged in quincunx (as indicated in the figure) and spaced by 10 μm in order to avoid ballistic focusing from one dot to the other.

As described in Section 1.4.3, the spin-orbit interaction in p-type GaAs is strong and leads to a splitting of the valence band into heavy holes (spin $= \pm \frac{3}{2}$) and light holes (spin $= \pm \frac{1}{2}$). In the quantum well used to fabricate our QD samples, only the heavy hole subband is populated. Moreover, the spin-orbit interaction gives rise to a zero magnetic field spin-splitting. The magnitude of this spin-splitting can be probed by SdH measurements [122, 148]. In this work, we investigate two different configurations: $p = 2.3 \times 10^{15}$ m^{-2} with an asymmetric confining potential, and $p = 1.7 \times 10^{15}$ m^{-2} where the quantum well is made symmetric by means of the gate voltages. Figure 3.9 shows the longitudinal resistivity of the 2DHS measured for both configurations. In Fig. 3.9(b) and (d), we plot the corresponding Fast Fourier Transform (FFT) power spectrum performed on the ρ_{xx} vs B^{-1} traces. For the first configuration, at $p = 2.3 \times 10^{15}$ m^{-2}, three peaks are well defined. The two lowest

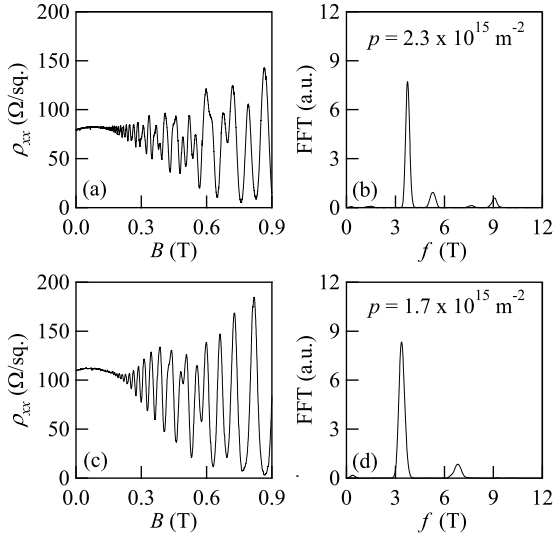

Figure 3.9: Longitudinal resistivity of the 2D hole system at (a) $p = 2.3 \times 10^{15}$ m^{-2} and (c) $p = 1.7 \times 10^{15}$ m^{-2}. Panels (b) and (d) show the corresponding FFT analysis of the SdH oscillations.

peaks at 3.7 and 5.3 T are related to the split spin subbands[10] while the higher frequency peak is their sum and represents the total sheet density of holes. For the second configuration at $p = 1.7 \times 10^{15}$ m^{-2}, because the applied gate voltage makes the quantum well symmetric and suppresses the SIA contribution to the total spin-orbit interaction, the two frequencies merge to the same value at 3.4 T. We then observe only two peaks, one corresponding to the spin subbands and one to the total hole density. Note that in the latter configuration, even though the confining potential is symmetric and only one frequency is observed for the two spin subbands in the SdH data, the zero magnetic field spin-splitting is still present [203].

3.4 Magnetoconductance fluctuations in single open quantum dots

The conductance g of D1 at $p = 2.3 \times 10^{15}$ m^{-2} is plotted in the upper panel of Fig. 3.10 as a function of B for various temperatures. The

[10]However, the position of the two lowest peaks in the FFT does not indicate the densities of the spin subbands [203].

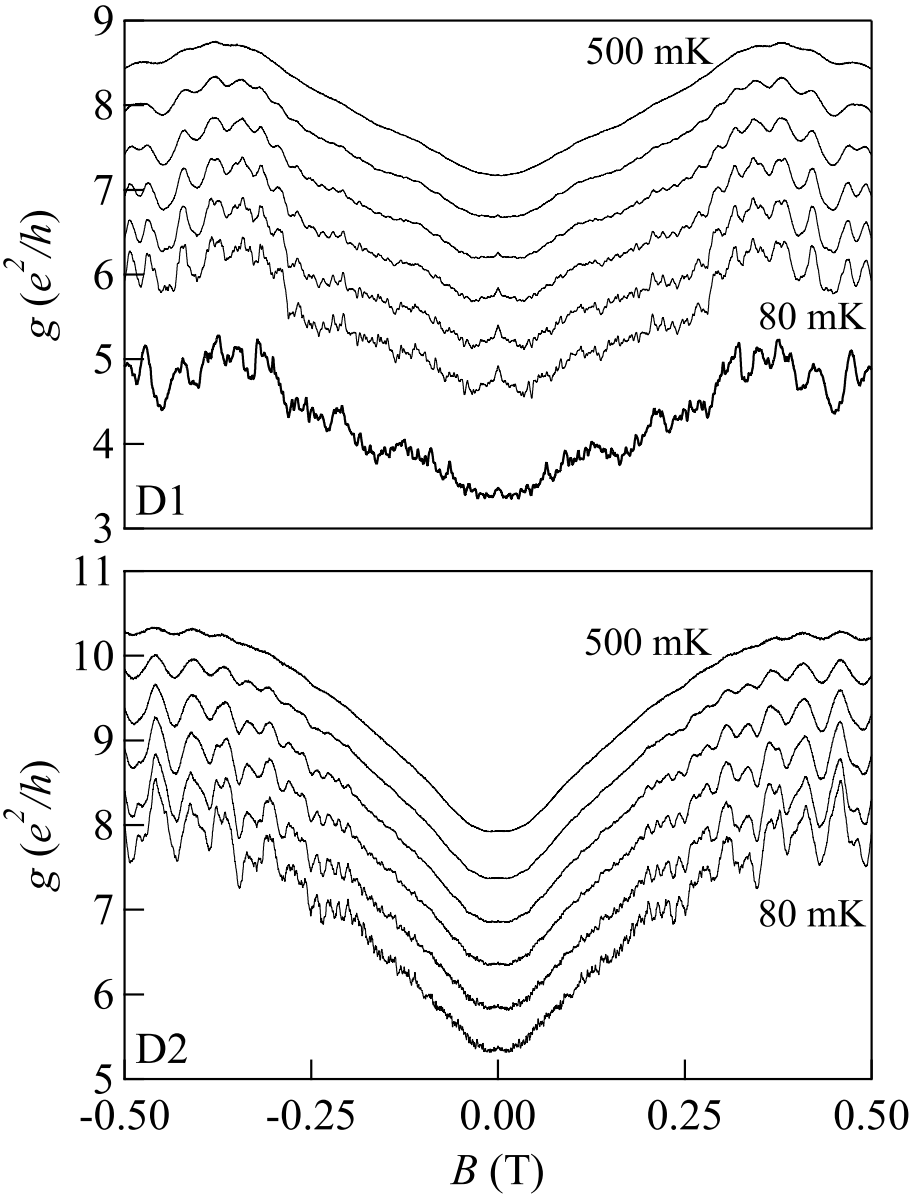

Figure 3.10: Magnetoconductance of D1 (upper panel) and D2 (lower panel) for $p = 2.3 \times 10^{15}$ m^{-2} at $T = 80$, 95, 135, 200, 300 and 500 mK. For clarity, traces are shifted upwards by 0.5 e^2/h. A magnetoconductance trace of D1 at 80 mK measured in a second cooldown (bold trace) is also shown in the upper panel and is shifted downwards by 1.5 e^2/h.

T's indicated here are the corrected T's using the technique described in Section 3.2.3.2. At the lowest temperatures, we observe reproducible magnetoconductance fluctuations (MCFs), symmetric with respect to $B = 0$ T, that can be attributed to quantum interferences of holes inside the dot. When T is increased, these MCFs are strongly reduced in amplitude and disappear for $T \gtrsim 500$ mK. At these high T's, only the slowly varying background remains, caused by ballistic effects in the cavity and the reduction of backscattering at the quantum point contact leads [190]. From the mean conductance, we deduce that 5 to 6 modes are populated in each quantum point contact. We also note that for $B > 0.25$ T, SdH oscillations are visible in the dot's magnetoconductance traces. Similar data were obtained at $p = 1.7 \times 10^{15}$ m^{-2} with two modes in each quantum point contact lead. The lower panel of Fig. 3.10 shows the magnetoconductance of D2 at $p = 2.3 \times 10^{15}$ m^{-2} and various T's. The traces obtained from D2 are similar to that from D1, while the MCFs exhibit a smaller amplitude and higher frequencies due to the larger area of D2 compared to D1.

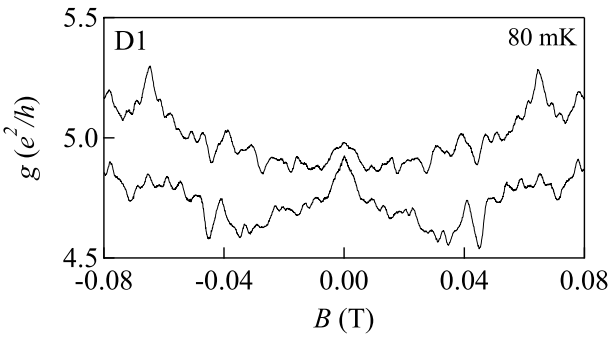

Figure 3.11: Magnified view of the magnetoconductance traces measured in D1 at $p = 2.3 \times 10^{15}$ m^{-2} and $T = 80$ mK. Traces are from two different cooldowns.

Around $B = 0$ T, a sharp peak is observed in the conductance of D1 at low T (Fig. 3.10, upper panel). This peak is reminiscent of the WAL correction to the conductivity. However, the superposition of the MCFs, which are comparable in magnitude, prevents any quantitative analysis of the WAL effect. This is clearly evidenced by a comparison of the $B = 0$ T peak for two different cooldowns of D1 (see Fig. 3.11). When a QD is thermally cycled between room and very low-T, the disorder potential inside the cavity is modified, leading to a different MCFs pattern. The WAL peak, on the other hand, is not sensitive to this change and is

preserved.

3.5 Weak antilocalization in open quantum dot arrays

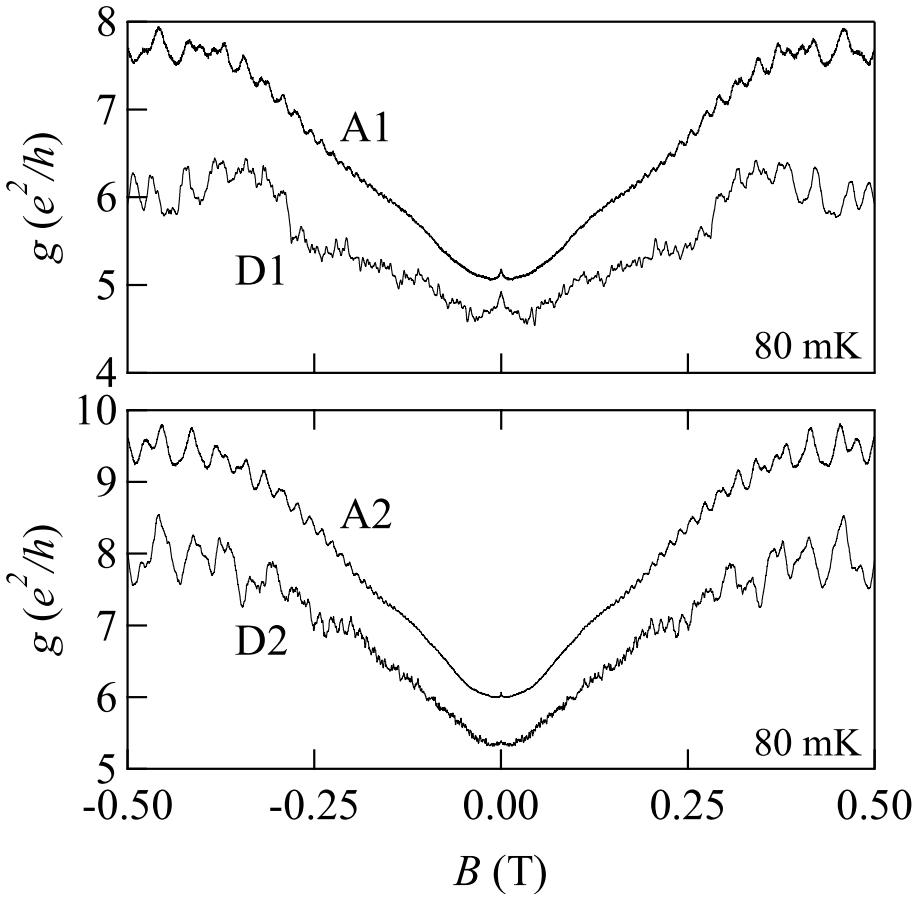

Figure 3.12: Comparison of the magnetoconductance of single QDs (D1 and D2) and QD arrays (A1 and A2) for $p = 2.3 \times 10^{15}$ m^{-2} and $T = 80$ mK.

In order to suppress the MCFs and access the WAL correction to the conductivity, it is necessary to average out the magnetoconductance traces obtained from QDs with the same area and the same number of modes in the QPC leads but with different intrinsic shapes. This averaging is naturally performed when measuring the conductance of QD arrays. While the lithographic geometry is identical for all the QDs of

the array, the disorder potential differs in each QD due to their different location in the 2DHS. As the disorder potential is not identical, each QD has then its own MCFs pattern, similar to what happens for two different cooldowns of the same QD.

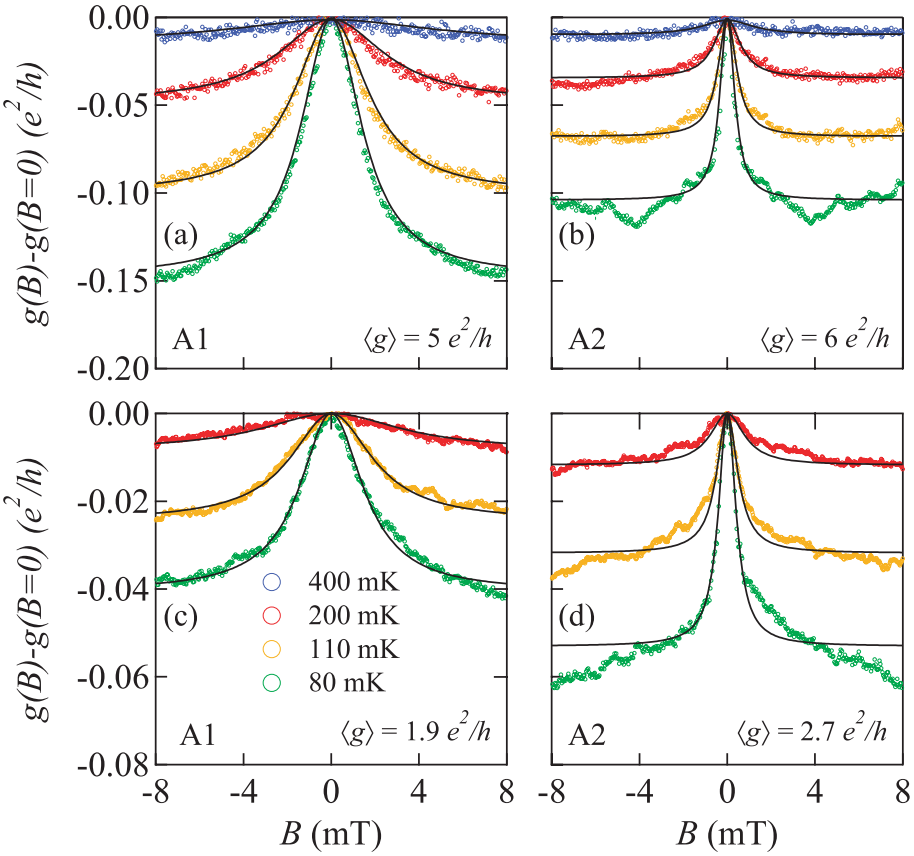

Figure 3.13: $g(B)-g(B=0)$ as a function of B at the indicated temperatures for (a) A1 and (b) A2 at $p = 2.3 \times 10^{15}$ m^{-2} as well as (c) A1 and (d) A2 at $p = 1.7 \times 10^{15}$ m^{-2}. Solid lines show the fits of the WAL peak using the RMT. The mean conductance $\langle g \rangle$ at $B = 0$ is given for each case.

A comparison of the low-T magnetoconductance traces of single QDs and QD arrays is presented in Fig. 3.12 for $p = 2.3 \times 10^{15}$ m^{-2}. As expected, the conductance of the arrays consists of a slowly varying background, similar to that of the single dots, but without the MCFs. Around $B = 0$ T, a peak associated with WAL can clearly be observed in the magnetoconductance of both QD arrays. The T-dependence of this peak is shown in Fig. 3.13 for both samples and for both investigated config-

urations. Similar to the MCFs, it disappears above $\sim$ 500 mK, further indicating that it is related to coherent effects in the cavities. Also, the general shape of the WAL peak seems to be independent of the symmetry of the vertical confining potential. Moreover, because the holes' trajectories enclose a smaller magnetic flux in a dot with a smaller area, the width of the WAL peak is found to be larger in the case of A1 than A2. Note also that our hole WAL peaks spread over a B range approximatively 4 times larger than in electron quantum dots with comparable areas [213, 37].

3.6 Dephasing time of 2D hole quantum dots

We now come to a more quantitative analysis of our data. To our knowledge, there has been no theoretical attempt to study the coherent transport of holes in quantum dots. In particular, an appropriate model for magnetotransport in GaAs hole quantum dots, in the spirit of the theory developed for WAL in 2DHSs [13], would possibly give access to both τ_ϕ and the spin relaxation times.

Generally, electron transport in open quantum dots is described using the random matrix theory (RMT). Although the RMT doesn't account for the complex band structure of GaAs hole systems under study here, it has been recently extended in order to take the spin-orbit interaction into account [7, 32, 43]. We use this framework to analyze our magnetoconductance data.

We start with the study of the WAL peak that provides information on both dephasing and spin-orbit interaction in the quantum dots. We fit the WAL peak using Eq. (2.18) [32] with $m^* = 0.38\ m_e$, where m_e is the free electron mass. The fits are shown in Fig. 3.13 as solid curves. The three parameters of this model are τ_ϕ, τ_{so} and c, where c is a geometrical factor. For each sample and configuration, c is determined from the fits to the lowest T traces. We obtain values ranging from 0.03 to 0.06. These values of the geometrical factor are found to be much smaller than 1 and reflect the large width of the WAL peak. The fits indicate that τ_{so} is too small ($\lesssim 10^{-11}$ s) to be probed by the WAL in our samples and further confirm that the quantum dots are in a strong spin-orbit coupling regime[11]. This deduction stands for both investigated configurations, meaning that the QDs remain in the strong spin-orbit regime while the SIA contribution has been reduced to zero by making the vertical confining potential symmetric. The BIA contribution alone

[11] Calculations of the WAL correction to the conductivity using the RMT and our QDs' parameters collapse on the same curve at fixed τ_ϕ for all values of $\tau_{so} \lesssim 10^{-11}$ s.

is sufficient to induce a strong spin-orbit regime in our QDs. We therefore extract the hole τ_ϕ in the quantum dots by setting $\tau_{so} = 0$ in the fits. The T-dependence of τ_ϕ in samples A1 and A2 is plotted in Fig. 3.15(a) and is discussed below.

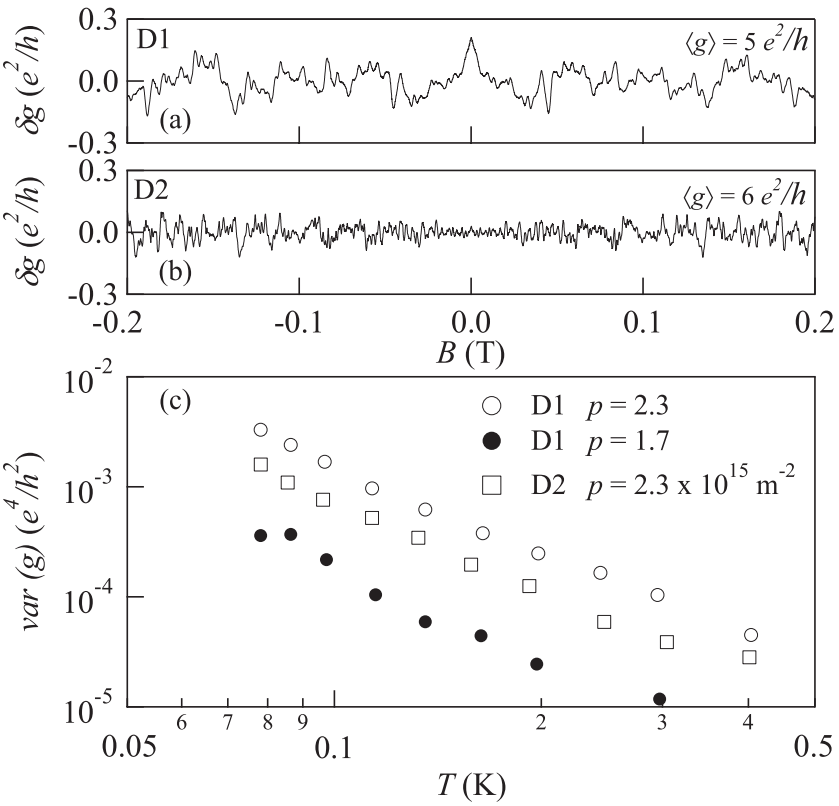

Figure 3.14: Magnified view of the MCFs of (a) D1 and (b) D2 at $p = 2.3 \times 10^{15}$ m^{-2} and $T = 80$ mK after background subtraction (see text). The mean conductance $\langle g \rangle$ is calculated in the range $-0.2 < B < 0.2$ T. (c) Variance of the MCFs as a function of T for D1 and D2.

The analysis of the MCFs also gives a measure of the carrier dephasing time. The RMT allows us to extract τ_ϕ from the variance of the dot's conductance, $var(g)$:

$$var(g) = \int_0^\infty \int_0^\infty f'(E) f'(E') cov(E, E') dE dE' \ , \qquad (3.1)$$

where E and E' are energies, $f'(E)$ is the derivative of the Fermi function, and $cov(E, E')$ is the conductance correlator, given by Eq. (2.23) [43].

Before calculating $var(g)$, we isolate the MCFs from the background by applying a high-pass filter to the traces. The determination of the cut-off frequencies f_c was performed as in Ref. [85]. We have used $f_c = 12$ and 17 T^{-1} for D1 at $p = 2.3 \times 10^{15}$ m^{-2} and $p = 1.7 \times 10^{15}$ m^{-2}, respectively, and $f_c = 37$ T^{-1} for D2 at $p = 2.3 \times 10^{15}$ m^{-2}. Filtered traces are shown in Fig. 3.14 for D1 and D2 at $p = 2.3 \times 10^{15}$ m^{-2} and $T = 80$ mK.

Once the background is removed, we calculate the variance of the MCFs in the range $0.04 < B < 0.2$ T. This range was chosen in order to ensure that time reversal symmetry is broken and also because of the SdH oscillations appearing for $B > 0.25$ T. The MCFs variance is plotted in Fig. 3.14(c) as a function of T for D1 at $p = 2.3$ and 1.7×10^{15} m^{-2}, and for D2 at $p = 2.3 \times 10^{15}$ m^{-2}. Once the MCFs variance is extracted, we calculate the hole τ_ϕ using Eq. (3.1). As established from the analysis of WAL, we set $\tau_{so} = 0$ in the calculation. The value of τ_ϕ deduced from the MCFs is shown in Fig. 3.15(b) as a function of T.

Figure 3.15 shows the hole dephasing time determined from our data. In Fig. 3.15(a) we show τ_ϕ extracted from the fits to the WAL peak of samples A1 and A2. Figure 3.15(b) shows τ_ϕ deduced from the variance of samples D1 and D2. For all investigated cases τ_ϕ exhibits a T-dependence that lies between T^{-1} and T^{-2}. The dephasing time does not change significantly when the number of modes in the leads is reduced from ~ 6 to ~ 2. While values of τ_ϕ extracted from the MCFs analysis are slightly smaller (see Fig. 3.15(c)), the results obtained from these two different methods are in excellent agreement[12].

By comparing τ_ϕ in our hole samples with data reported for electrons in GaAs open quantum dots [24, 40, 84, 98, 120], we observe that τ_ϕ is approximately one order of magnitude smaller for holes. Generally, the expected mechanisms leading to dephasing at low T in quantum dots are carrier-carrier scattering [98] as well as geometrically related mechanisms such as dwell-time limiting effect [86] and environmental coupling [26, 59]. The T-dependence of τ_ϕ in our dots can be described within the Fermi liquid theory as the sum of a T^{-2} and a T^{-1} terms originating from large-energy-transfer carrier-carrier scattering (Eq. (2.25)) and from the Nyquist scattering mechanism (Eq. (2.26)), respectively [9, 39]. Nevertheless, within the Fermi liquid theory, the value of τ_ϕ is expected to decrease only by a factor of ~ 3 for holes with respect to electrons because of their smaller Fermi energy and lower mobility. This reduction factor does not explain the small value of τ_ϕ

[12] An effective mass $m^* = 0.38\ m_e$ (heavier heavy holes) has been used in our calculations of τ_ϕ. Using $m^* = 0.2\ m_e$ (lighter heavy holes) reduces the extracted value of τ_ϕ by a factor of ~ 2 for both sets of data.

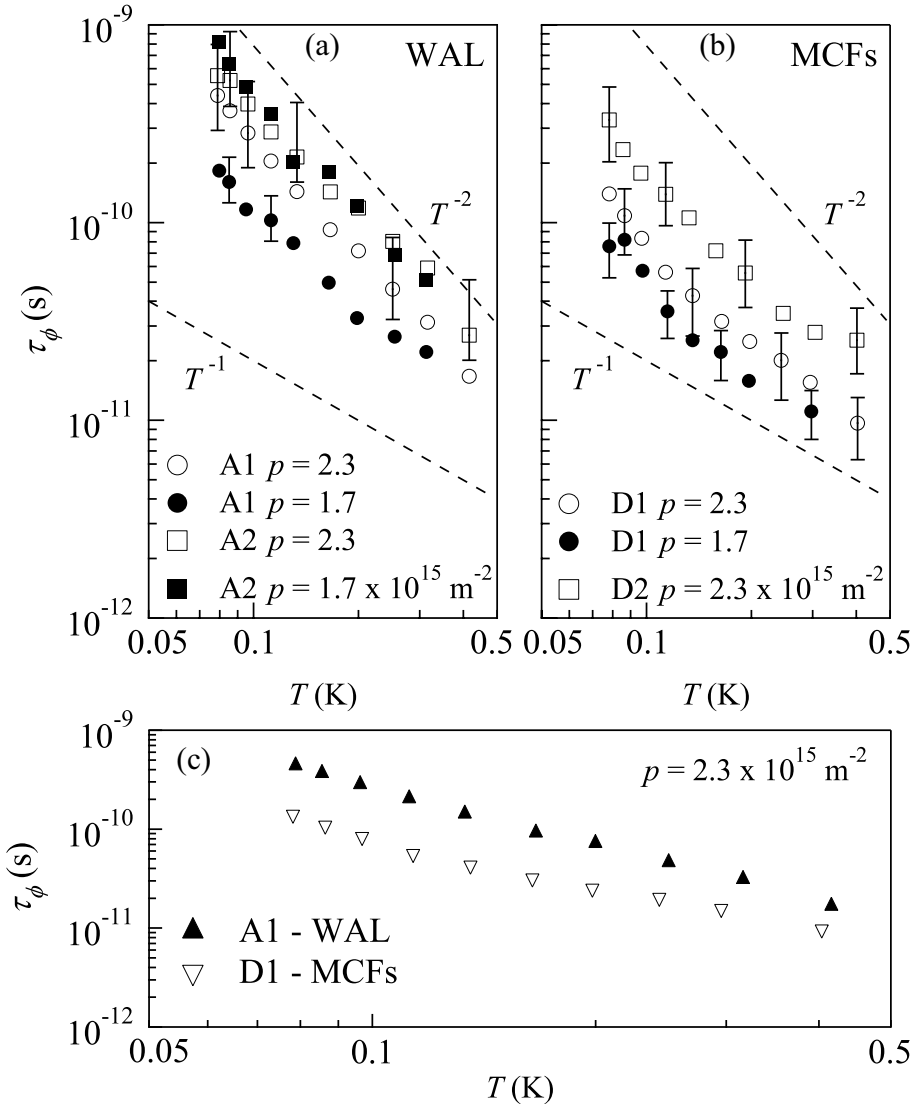

Figure 3.15: Dephasing time τ_ϕ of holes as a function of T. (a) τ_ϕ extracted from the WAL correction to the conductivity in samples A1 and A2. (b) τ_ϕ calculated from the variance of the MCFs in samples D1 and D2. Open and solid symbols correspond to asymmetric and symmetric confining potential, respectively. The dotted lines indicate various T dependencies. Error bars are determined from uncertainties in the number of modes in the quantum point contact leads and in the dots' areas. (c) Comparison of the T-dependence of τ_ϕ for sample D1 (MCFs analysis) and sample A1 (WAL analysis) at $p = 2.3 \times 10^{15}$ m^{-2}.

extracted for our quantum dots. However, Fermi liquid theory has been formulated for electrons and might not be directly applicable to 2D holes. Moreover, in 2DHSs other mechanisms such as intersubband scattering can contribute to the total hole dephasing.

We now compare τ_ϕ extracted for our dots with values measured in 2DHSs. Unfortunately, in GaAs (311)A 2DHS, the magnetoconductance around $B = 0$ originates from a combination of different factors [149], making the extraction of τ_ϕ from the WAL difficult. Nevertheless, τ_ϕ measurements have been reported for very low density (311) GaAs, as well as for (100) GaAs and InGaAs p-type quantum wells [132, 135, 152, 163, 176]. Extracted τ_ϕ values in these 2DHSs are consistent with τ_ϕ measured in our quantum dots. This indicates that the small value of τ_ϕ observed in our samples is likely related to scattering mechanisms in the 2DHS.

The Zeeman energy has been shown theoretically [88] and experimentally [71] to reduce the MCFs' variance by a factor of two when the spin splitting is sufficiently strong to allow the spin states to become statistically independent. Moreover, a strong enough parallel magnetic field breaks time reversal symmetry and suppresses the WAL correction to the conductivity. At intermediate values of the Zeeman energy, the amplitude of the WAL is reduced [32, 43]. In our experiments, the hole QDs were subjected to a strictly perpendicular B and, for the study of the MCFs and of the WAL, the Zeeman energy was negligible. However, the strong spin-orbit interaction in 2DHS leads to a $B = 0$ T spin splitting that is not accounted in the RMT. The effect of such a splitting on the statistical properties of open QDs, and in particular on the MCFs, is not clear and should be further investigated. This study could be performed by increasing the spin splitting by means of a second magnetic field applied parallel to the 2D system and monitoring the evolution of the MCFs' variance, similar to the experiment by Folk *et al.* [71] in electron QDs.

3.7 Magnetoresistance hysteresis at integer filling factors

In Fig. 3.16, we plot the high-B magnetoresistance of D1 for $p = 2.3 \times 10^{15}$ m^{-2} and $T = 70$ mK. Data are shown for both up and down sweeps of B. The most striking features of these traces is the observation of hysteresis around interger LL filling factors $\nu = 1, 2$ and 3. Around $\nu = 2$ (Fig. 3.16(c)), Aharonov-Bohm oscillations are superimposed on the magnetoresistance background. Such oscillations have already been

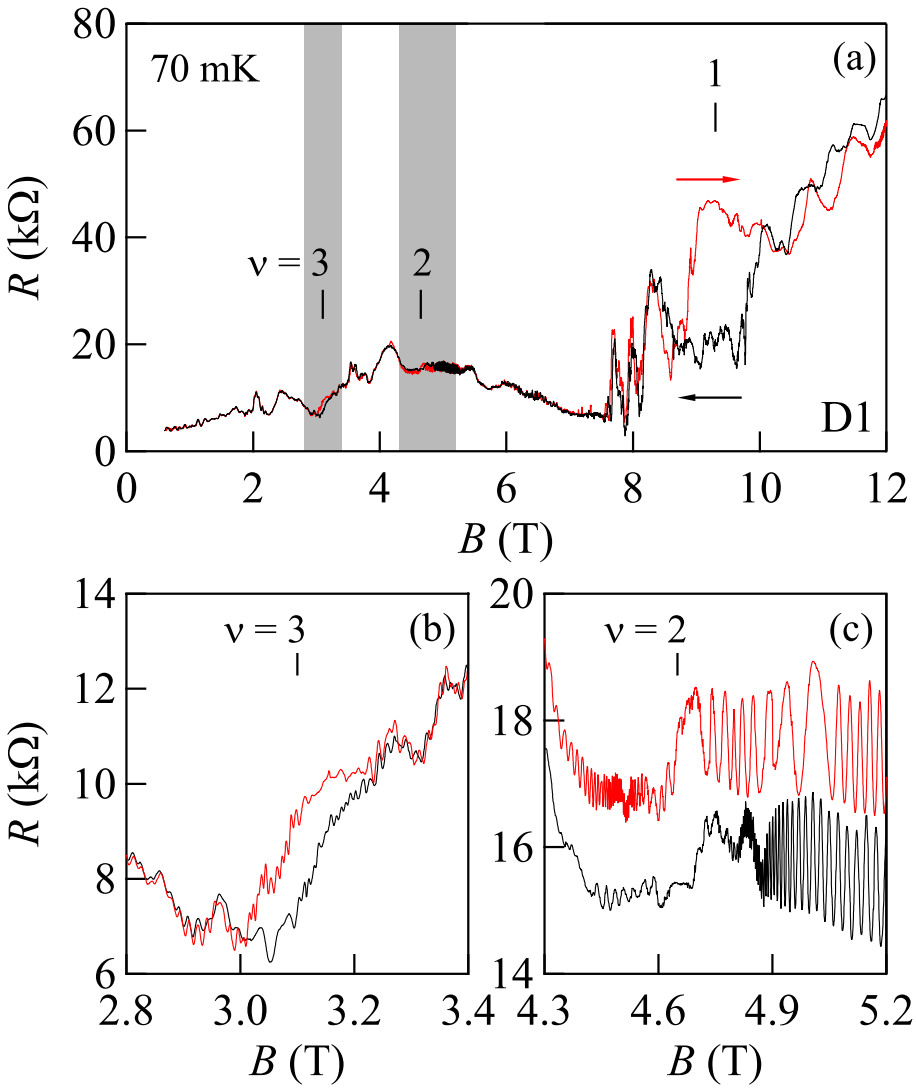

Figure 3.16: (a) High-B magnetoconductance of D1 for $p = 2.3 \times 10^{15}$ m^{-2} and $T = 70$ mK. Data are shown for both up (red trace) and down (black trace) sweeps of B at a rate of 0.02 T/min. The shaded areas highlight the B-ranges around $\nu = 3$ and $\nu = 2$ that are presented in a magnified view in panels (b) and (c), respectively. In panel (c), the up sweep trace is shifted upwards by 2 kΩ for clarity.

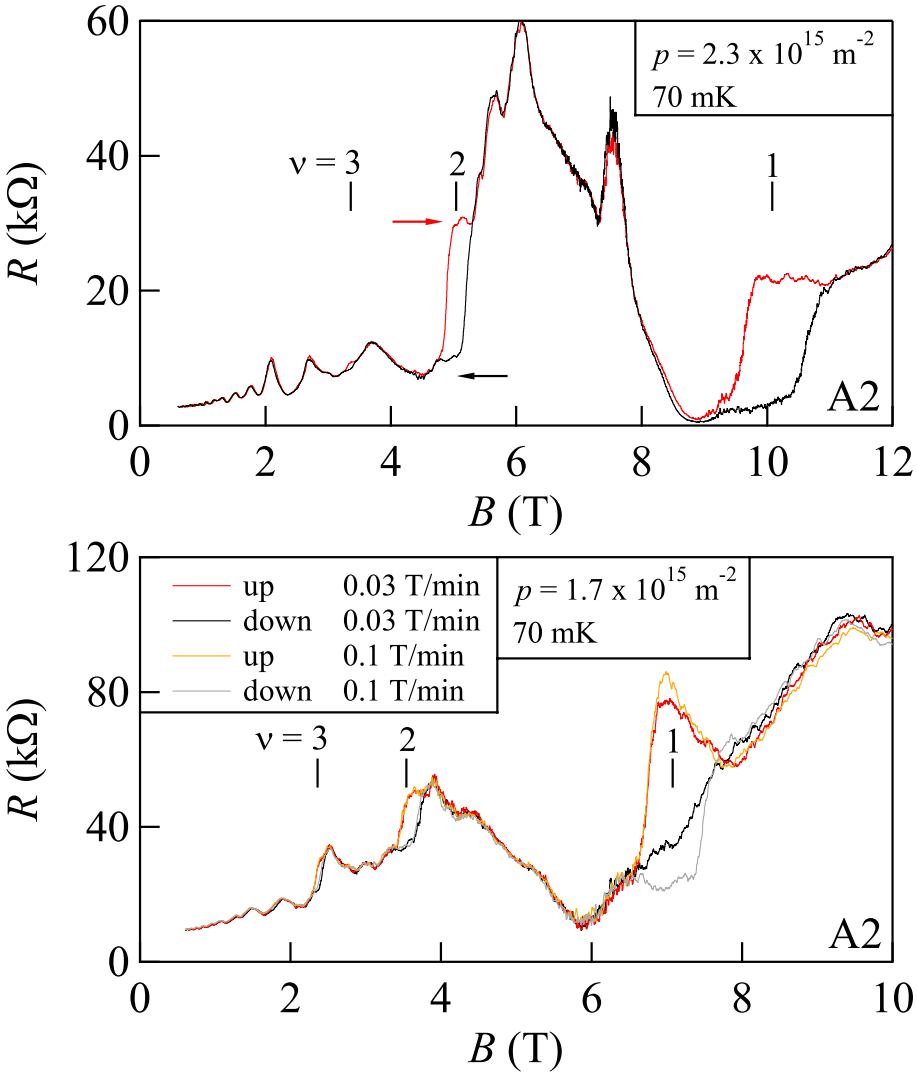

Figure 3.17: High-B magnetoconductance of A2 at $T = 70$ mK for $p = 2.3 \times 10^{15}$ m^{-2} (upper panel) and $p = 1.7 \times 10^{15}$ m^{-2} (lower panel). In the upper panel, data are shown for both up (red) and down (black) sweeps of B at a rate of 0.03 T/min. In the lower panel, similar data are presented at two different sweep rates of 0.03 T/min (red, black) and 0.1 T/min (yellow, grey).

observed in the magnetoresistance of open QDs in the quantum Hall regime, and were attributed to the formation of edge state loops inside the cavity [25]. While the hysteresis around $\nu = 2$ is not as clear as for $\nu = 1$ and 3, it can be seen as a perturbation of the frequency of the Aharonov-Bohm oscillations. When B is swept (up or down) and $\nu = 2$ is approached, the Aharonov-Bohm oscillations' frequency first strongly increases. Then, while passing through $\nu = 2$, it becomes very low and comes back to normal. Similar results were obtained from D2.

In Fig. 3.17, similar data are shown for the QD array A2 at $p = 2.3 \times 10^{15}$ m^{-2} (upper panel) and $p = 1.7 \times 10^{15}$ m^{-2} (lower panel). In the case of the QD arrays, all the fluctuations are smoothed out and only the magnetoresistance background remains. The hysteresis at the integer LL filling factors can clearly be observed for both investigated configurations, indicating that it is not related to the shape of the vertical confining potential. In the lower panel of Fig. 3.17, we show data for two different sweep rates. Around $\nu = 1$, the size of the hysteresis increases with the sweeping rate.

Similar hysteresis features were observed in gated electron QPCs and closed QDs in the quantum Hall regime [154, 155] and were attributed to time-varying B-induced eddy currents. Such time-varying B-induced currents in clean 2D systems become large when $\rho_{xx} \to 0$ at integer or fractional LL filling factors [107, 131] and can persist for hours after the B sweep stops. In order to explain the magnetoresistance hysteresis in their gated nanostructures, Pioro-Ladrière *et al.* [154, 155] invoked these long-lived eddy currents as the origin of charge transfer from the center to the egdes of the 2D areas surrounding the nanostructure. This charge accumulation in the regions adjacent to the metallic top gates, whose sign depends on the B sweep direction, modifies the depletion under the gates and, hence the geometry of the device. Similar arguments can be used to interpret our data. While our samples are defined by etching, charge accumulation at the edge of the devices could possibly modify the size of the depletion zone and the shape of the lateral confining walls. In our case, however, it is not clear whether the eddy currents are only induced in the surrounding 2D system areas or also inside the cavity of the QD. Indeed, the perturbation of the Aharonov-Bohm oscillations' frequency indicates a modification of the area of the edge state loop inside the cavity.

3.8 Conclusion

In this chapter, we presented the fabrication process used to construct open QDs from a p-type (311)A GaAs quantum well. Using this fabrication process, we realized two single QDs with areas of 1.4 and 4.5 μm^2 as well as two 10×10 QDs arrays with similar cavities as the single dot samples.

We report the first magnetotransport measurements on hole open QDs, that show clear evidence of coherent transport when $T < 500$ mK. The single QDs' magnetoconductance traces show a rich spectrum of fluctuations, while the QD arrays allow a direct measurement of the WAL correction to the conductivity. We have analysed these coherent effects using an extended RMT that includes spin-orbit interaction and have extracted a T-dependence for τ_ϕ together with an upper limit for τ_{so}.

From the analysis of the WAL peak, we determined that $\tau_{so} \lesssim 10^{-11}$ s, independent of the shape of the vertical confining potential. This indicates that the BIA contribution to the spin-orbit interaction is large enough to induce a strong spin-orbit regime in our micrometer-sized QDs. The realization of p-type GaAs-based systems with controlable spin-orbit interaction through a modification of the vertical confining potential could only be achieved by decreasing the devices' size or by reducing the BIA contribution to the spin-orbit interaction. The reduction of the BIA contribution could be performed by modifying the total hole sheet density.

The T-dependence for τ_ϕ extracted from our magnetotransport measurements lies between T^{-1} and T^{-2}. While this T-dependence resembles that measured in similar electron QDs, the value of τ_ϕ is found to be one order of magnitude smaller for holes than for electrons. On the other hand, the value of τ_ϕ extracted from our samples is consistent with that reported for various p-type 2D systems, indicating that the small value of τ_ϕ observed here is likely related to scattering mechanisms in the 2DHS.

Chapter 4

Thermopower in 2D systems

> Thermopower is one of the easiest experiments that can be performed on conductors.
>
> *P. M. Chaikin*

4.1 Introduction

The thermoelectric properties of materials, that have been discovered experimentally by Seebeck and Peltier, relate the heat flux and the electrical current flowing through matter. The thermoelectricity is expressed in three different, yet related phenomena, namely the Seebeck, Peltier and Thomson effects [78, 142, 168].

Since their discovery in the 19^{th} century, the thermoelectric effects have generated much interest for many different applications. The most widespread thermoelectric-based device is the thermocouple that provides a low cost and wide T-range thermometer. Several other applications have been considered, such as thermoelectric coolers and heat-to-electricity converters [168]. Thermoelectric coolers, for example, have been used for particular applications like CPU cooling and have the advantage to be void of mobile parts. However, thermoelectric materials currently available are not performant enough to allow thermoelectric devices to be pervasive in daily applications. Recent work has mainly focused on the development of new high-performance thermoelectric materials [142, 168], especially with low dimensionality [53, 168].

Beyond the industrial applications, thermoelectric effects are also of great interest for the understanding of the electronic properties of materials. Indeed, the sign, magnitude and T-dependence of the thermoelectric coefficient provide many complementary pieces of informations

to those given by the electrical conductivity. In particular, the thermoelectric effects are sensitive tools to probe 2D system's ground state and the scattering mechanisms involved in the conduction process [36]. The thermoelectric coefficients are thus perfectly suitable to investigate the 2D metal-insulator transition (MIT) problem. As an example, thermoelectric effect studies have helped identify the ground state of B-induced insulating phases in 2D GaAs [19] and SiGe [158] hole systems.

In the following chapters, we will investigate the evolution of Seebeck coefficient for the parallel B-induced MIT [2D GaAs hole heterostructures] as well as for perpendicular B-induced MIT [2D bilayer GaAs hole systems]. This chapter briefly reviews the essential concepts for understanding the thermoelectric effects in 2D carrier systems. It also presents the samples' preparation and the measurement technique used to access the Seebeck coefficient in 2D GaAs heterostructures down to very low T.

4.2 Basic concepts

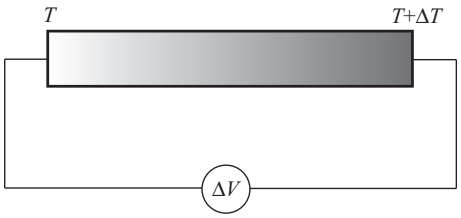

Figure 4.1: Illustration of the Seebeck effect in a rod-shaped sample subjected to a thermal gradient. The Seebeck coefficient or thermopower S is given by the ratio of the voltage drop ΔV to the temperature difference ΔT.

The Seebeck effect is the voltage drop appearing between two points of a material, which are kept at different temperatures. If one considers a rod-shaped sample subjected to a thermal gradient, as presented in Fig. 4.1, the Seebeck coefficient or thermopower S is defined by:

$$S = \lim_{\Delta T \to 0} \frac{\Delta V}{\Delta T}. \tag{4.1}$$

The thermopower is an intrinsic property of the considered material and generally has three different origins (or components): the diffusion thermopower S^d, the phonon-drag thermopower S^g and the magnon-drag thermopower. The latter is only observed in magnetic materials or in materials containing magnetic impurities. Therefore, in the clean 2D

semiconductor heterostructures under scrutiny in this work, the total thermopower S is the sum of the diffusion and phonon-drag contributions:

$$S = S^d + S^g. \tag{4.2}$$

A simple picture to understand the diffusion thermopower S^d of a conductor is the following. When the sample is subject to a thermal gradient, because of the spreading of the Fermi-Dirac distribution, there will be more carriers with higher velocities in the hot side of the sample. The carriers then leave the hot side faster than the cold side. This results in a net flux of carriers from the hot side to the cold side of the sample. At equilibrium, a voltage drop is established, due to the accumulation of carriers at the cold side, and counterbalances the flux generated by the asymmetry of the Fermi-Dirac distribution spreading. Interestingly, the diffusion thermopower has been shown to be a measure of the entropy per carrier or of the heat per carrier over T [36].

The phonon-drag thermopower S^g can be described as follows. The thermal gradient applied to the sample induces a flow of phonons from the hot side to the cold side. Due to the phonon-carrier interaction, there will be a net transfer of momentum from phonons to carriers, preferentially in the direction of the thermal gradient. The carriers are then dragged by the phonons to the cold side of the sample.

Based on these simple descriptions of diffusion and phonon-drag thermopowers, we have seen that the carriers tend to accumulate at the cold side of the sample for both effects. One then expects a negative thermopower for electron systems and a positive one for hole systems. The situation, however, is a bit more complicated and the nature of the carriers alone does not necessarily determine the sign of S. A more quantitative description of diffusion and phonon-drag thermopower is provided in the following sections for the particular case of 2D systems.

4.3 Diffusion thermopower in 2D systems

4.3.1 Degenerate carrier gas

Within the Boltzmann approach, the diffusion thermopower S^d of a 2D degenerate carrier gas (Fig. 4.2) can be expressed as a function of the conductivity σ through the famous Mott formula [66, 74]:

$$S^d = \frac{\pi^2 k_B^2 T}{3q} \frac{\mathrm{d}\ln\sigma}{\mathrm{d}\ln E}\bigg|_{E_F}, \tag{4.3}$$

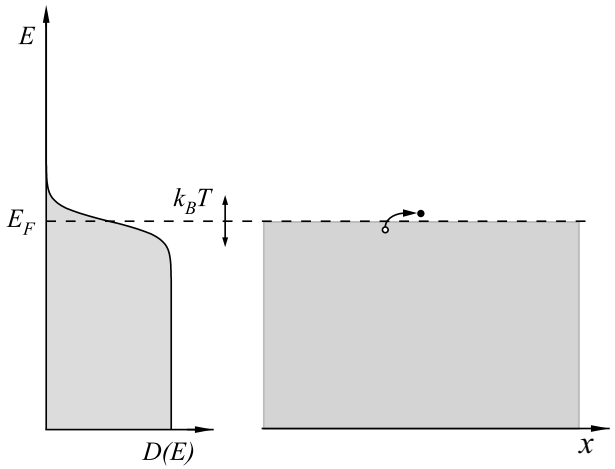

Figure 4.2: Schematic representation of the DOS as a function of the energy and the allowed states vs position in real space for a metal.

where q is the carrier charge. If σ is expessed in terms of an energy dependent relaxation time $\tau(E) \propto E^{\alpha}$, where α is a constant, then Eq. (4.3) writes as

$$S^d = \frac{\pi^2 k_B^2 T}{3qE_F}(1+\alpha). \tag{4.4}$$

Assuming that α is T-independent, the diffusion thermopower of a degenerate 2D carrier gas is then expected to decrease linearly with T. It can be shown that the first term of Eq. (4.4) expresses the entropy of the system. The second one, on the other hand, measures the energy dependence of the dominant carrier scattering mechanism.

When a magnetic field is applied perpendicular to the 2D carrier system, S^d is a tensor with two independent components, under the assumtion that the system is isotropic in the xy plane. One distinguishes between the longitudinal thermopower $S_{xx} = S_{yy}$ and the transverse thermopower (Nernst Ettingshausen coefficient) $S_{xy} = -S_{yx}$. Within the Boltzmann approach, the diffusion thermopower coefficients read as [66]

$$\overline{S_{xx}^d} = \frac{\pi^2 k_B^2 T}{3qE_F}\left(1 + \frac{\alpha}{1+\beta^2}\right), \tag{4.5}$$

$$\overline{S_{yx}^d} = \frac{\pi^2 k_B^2 T}{3qE_F}\left(1 + \frac{\alpha\beta}{1+\beta^2}\right), \tag{4.6}$$

where $\beta = \mu B$. The bars over the S^d symbols denote that these equations only describe the non-oscillatory part of the diffusion thermopower coefficients. Indeed, at low T, when B is increased, oscillations in ρ and S^d are observed when the LLs' separations exceed their broadening. At low B, when the LLs are not fully resolved, the oscillatory part of the thermopower coefficients can be calculated from ρ_{xx} and ρ_{xy} using the Mott formula (see Ref. [66] for details). The thermopower oscillations are phase shifted by $\pi/2$ with respect to the ρ_{xx} oscillations. At higher B, in the quantum Hall regime, *i.e.* when the localized states play a predominant role, the separation of the smooth and oscillatory parts of S^d is no more appropriate. In this regime, S^d_{xx} can be extracted from the entropy per carrier [66]. One then expects S^d_{xx} to oscillate between 0, when E_F lies between two LLs, and a maximum value of

$$S^d_{xx} = \frac{k_B \ln 2}{q(n + \frac{1}{2})}, \tag{4.7}$$

when $n + \frac{1}{2}$ LLs are populated. In the high-B regime, the S^d_{xx} and ρ_{xx} oscillations are in phase. Finally, note that S^d_{yx} is expected to be small at high B [66].

4.3.2 Energy gap

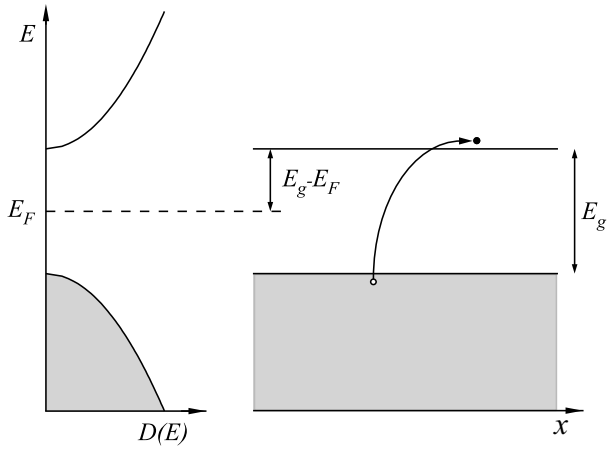

Figure 4.3: Schematic representation of the DOS as a function of the energy and the allowed states vs position in real space for a semiconductor. Transport takes place by carriers excited above the energy gap.

Let's now consider a 2D system that presents an energy gap E_g

(Fig. 4.3). We have seen previouly that the diffusion thermopower can be simply expressed as the heat per carrier over T. In such a system, the heat carried by a particle excited across the energy gap is given by the difference between the band edge energy and the chemical potential of the system $\sim E_F$. The heat of an excited carrier is then $(E_g - E_F) \sim E_g/2$ and the diffusion thermopower is [36]

$$S^d \sim \frac{E_g}{2qT} = \frac{k_B}{q}\frac{E_g}{2k_BT}. \tag{4.8}$$

A more rigorous estimation of S^d in gapped systems provides [212],

$$S^d = \frac{k_B}{q}\left(\frac{E_g}{2k_BT} + \mathcal{C}\right), \tag{4.9}$$

where $\mathcal{C}$ is a constant of order unity that takes into account the energy dependence of the relaxation time. Similar to Eq. (4.4), which is developed for a degenerate carrier gas, the first term of Eq. (4.9) represents the carriers' entropy while the second term depends on the energy dependence of the scattering mechanisms. If $E_g \gg k_BT$, the entropy term dominates and one finds Eq. (4.8) again. The diffusion thermopower of a system with an energy gap has a T^{-1} dependence and diverges as $T \to 0$.

4.3.3 Strongly disordered 2D systems

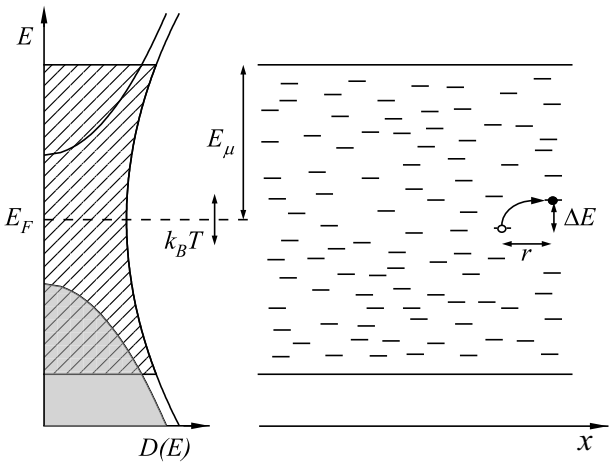

Figure 4.4: Schematic representation of the DOS of a disordered semiconductor. Localized states have filled the band gap and the mobility edge has moved into the band. Carrier transport occurs by jumps between localized states.

In the presence of disorder, localized carriers' states can be introduced into the band gap of a semiconductor system (Fig. 4.4). If the disorder is sufficiently important, a continuous DOS can even be established in the gap and a finite value of the DOS can be observed at E_F. When disorder is further increased, the states in the conduction and valence bands' tails become localized [36, 45]. The energy difference between E_F and the energy onset of the extended states is referred to as the mobility gap E_μ.

When $k_BT \gg E_\mu$, transport occurs by activation of carriers across the mobility gap. At low T ($k_BT \ll E_\mu$), however, transport in such disordered sytems takes place between localized states (Fig. 4.4). The probability for an electron to be transferred from one state to another decreases exponentially with the distance r between the sites and also with the energy difference ΔE between these two sates. The transfer rate between two different states is then proportional to $e^{-ar}e^{-\frac{\Delta E}{k_BT}}$, where a is a constant characterizing the spatial decrease of the carrier wavefunctions. This transport mechanism is known as Variable Range Hopping (VRH).

If one consider a 2D disordered system with a slowly varying DOS around E_F, the conductivity of the system has the following form [34, 215]:

$$\sigma = \sigma_0 \exp\left[-(T_0/T)^{1/3}\right], \tag{4.10}$$

where σ_0 is weakly dependent on T, and

$$T_0 = \mathcal{A}\frac{4a^2}{\pi k_B D(E_F)}, \tag{4.11}$$

with $\mathcal{A} \sim 7$. This transport mechanism is known as the Mott VRH. The diffusion thermopower in 2D systems with Mott VRH is given by [34]

$$S^d = \frac{k_B}{2q}a^{4/3}\left[\frac{1}{\pi D(E_F)}\right]^{2/3}\left.\frac{\partial \ln D(E)}{\partial E}\right|_{E_F}(k_BT)^{1/3}. \tag{4.12}$$

The diffusion thermopower is then expected to behave as $T^{1/3}$, while the magnitude as well as the sign of S^d are mainly determined by the shape of the density of states distribution around E_F.

The above considerations have been formulated for systems with a slowly varying DOS around E_F. However, it has been shown that Coulomb interaction between localized states decreases the DOS around E_F. Then, in the presence of carrier-carrier interactions, the DOS exhibits a minimum in the vicinity of the Fermi level and vanishes at E_F,

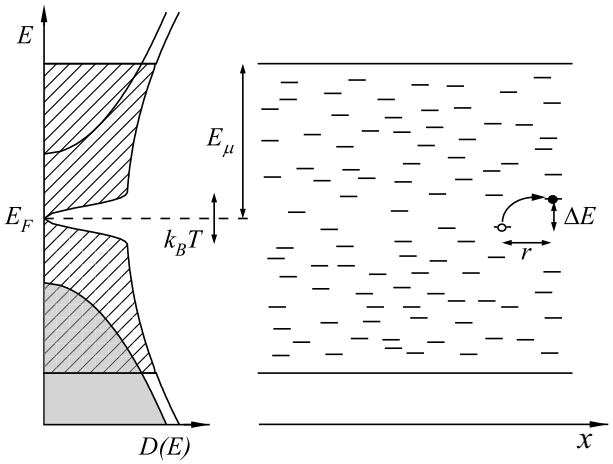

Figure 4.5: Schematic representaion of the DOS of a disordered semiconductor. Localized states have filled the band gap and the mobility edge has moved into the band. The carrier-carrier interaction leads to a reduction of the DOS around E_F, *i.e.* the formation of a Coulomb gap. Carrier transport occurs by jumps between localized states.

forming the Coulomb gap (Fig. 4.5). At low T, the conduction mainly occurs through the states within the Coulomb gap. Under this condition, the transport is referred as Efros-Shklovskii VRH and the conductivity is expressed as [34, 215]

$$\sigma = \sigma_0 \exp\left[-(T_0'/T)^{1/2}\right], \tag{4.13}$$

with

$$T_0' = \frac{8aq^2}{k_B K}, \tag{4.14}$$

where K is the dielectric constant. Here again, σ_0 is only weakly T-dependent. As for the diffusion thermopower, it reads as [34]

$$S^d = \frac{k_B q}{K} a \left.\frac{\partial \ln D_0(E)}{\partial E}\right|_{E_F}, \tag{4.15}$$

where $D_0(E)$ is the non-interacting DOS. The low-T thermopower of system with a Coulomb gap is expected to be T-independent. Here, also, the magnitude and the sign of S^d are determined by the shape of the DOS around E_F.

4.4 Phonon-drag thermopower in 2D systems

Let's assume that phonons are a 3D gas subjected to a thermal gradient. Under these conditions, there is also a pressure gradient and, consequently, a net force in the direction of the thermal gradient. Thanks to the carrier-phonon interaction, a fraction of this force is exerted onto the carriers. At equilibrium, an electric field couterbalances the force exerted by the phonon gas. Based on these simple considerations, it can be shown that, for a 2D degenerate carrier gas with a sheet density n_{2D}, the phonon-drag thermopower S^g can be written as [74]

$$S^g = \frac{CL_z}{3qn_{2D}} \frac{\tau_p'}{\tau_p' + \tau_{pe}}, \tag{4.16}$$

where C is the specific heat, L_z is the specimen's dimension in the confinement direction, τ_p' is the phonon relaxation time excluding carrier-phonon scattering and τ_{pe} is the phonon relaxation time due to scattering from carriers only. Al low T and low n_{2D}, τ_p' is limited by boundary scattering and S^g can be reformulated as

$$S^g = \frac{CL_z}{3qn_{2D}} \frac{\Lambda}{v_s \tau_{pe}}, \tag{4.17}$$

where v_s is the sound velocity, and Λ is the phonon mean free path. For single crystals with non-specular reflections, Λ corresponds to the specimen's minimum dimension. Considering that the lattice thermal conductivity κ_l can be expressed as [78]

$$\kappa_l = \frac{1}{3} C v_s \Lambda, \tag{4.18}$$

the phonon-drag thermopower writes as

$$S^g = \frac{\kappa_l L_z}{q v_s^2 n_{2D}} \tau_{pe}^{-1}. \tag{4.19}$$

As established in Eq. (4.19), the T dependence of the phonon-drag thermopower is determined by the lattice thermal conductivity and by the electron-phonon interaction. In a crystalline solid, where Λ is limited by boundary scattering, κ_l has the same T dependence as the specific heat [78] and is proportional to T^3. The phonon relaxation time due to scattering from carriers only τ_{pe}, on the other hand, is strongly dependent on $|\mathbf{q}|/2k_F$, where $\mathbf{q}$ is the average phonon wavevector [74].

At low T, when the average phonon wavevector $|\mathbf{q}| \ll 2k_F$, τ_{pe} is small and increases with T. The increase of τ_{pe} with T depends on the material used to build the 2D system. In systems with screened

deformation potential scattering, the evolution of τ_{pe} with T leads to $S^g \propto T^6$. If the screened piezoelectric scattering dominates, $S^g \propto T^4$. When screening is negligible, a T^4 and a T^2 dependence correspond to the deformation potential and piezoelectric carrier-phonon scattering mechanisms, respectively [159]. In GaAs heterostructures, piezoelectric carrier-phonon scattering has been shown theoretically to be the dominant contribution below 2 K [124], in agreement with experimental results that have reported a T^4 dependence at very low-T for both electron [70, 183] and hole [64, 65, 137] systems. In Si inversion layers, a T^6 dependence of S^g has been reported [68], consistent with carrier-phonon scattering mediated by a screened deformation potential. In p-type Si/SiGe heterostructure, a T^4 dependence of S^g observed [159]. In this particular case, however, it is not clear whether this behavior arises from screened piezoelectric carrier-phonon scattering or unscreened deformation potential carrier-phonon scattering.

When $|\mathbf{q}| = 2k_F$, τ_{pe} shows a maximum [74]. At this particular T, $S^g \propto T^3$. Such behavior of the electron-carrier scattering rate and the phonon-drag thermopower have been observed in various 2D systems [74], including GaAs heterostructures [70, 137].

At higher temperatures, *i.e.* for $|\mathbf{q}| \gg 2k_F$, τ_{pe} falls rapidly when T is increased and S^g increases much more slowly than T^3. Finally, when the temperature is further raised, measurements in electron GaAs heterostructures [67] have shown that S^g reaches a maximum and decreases with increasing T. Note that in this regime, the phonon mean free path is limited by phonon-phonon scattering and decreases below the boundary scattering value.

In a perpendicular B, quantum oscillations of S^g have been reported in various 2D systems. While there is no theoretical framework to describe the low-B behaviour of S^g, the high-B oscillations can be described in a simple picture. They arise from the modulation of the available initial and final possible states for carriers interacting with phonons, whether the Fermi level lies between two LLs or is close to the center of a LL. Note also that the magneto-oscillations of S^g_{xx} were found to be in phase with that of ρ_{xx} both at low-B and in the quantum Hall regime [74]. The behaviour of S^g_{yx} in a magnetic field is still poorly understood and several controversial results have been reported. For details concerning S^g_{yx}, see Ref. [66] and references therein.

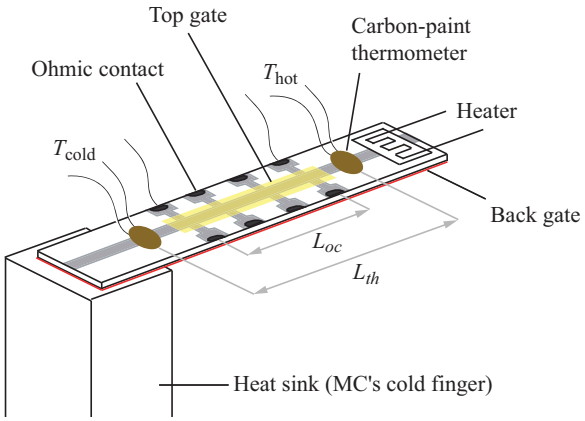

Figure 4.6: Schematic representation of the thermopower measurement set up (see text).

4.5 Low-T thermopower measurement technique

4.5.1 Sample preparation and mounting

The samples used to measure the thermopower in 2D GaAs hole heterostructures are 8×2 mm^2 pieces of wafer (see Fig. 4.6). Four ohmic contacts, spaced by $\sim$ 1 mm, are placed on each side of the sample, around the center of the longer edges. The ohmic contacts consist in small droplets of In/Zn alloy (92%/8%) deposited by means of a soldering iron. In order to make the Zn dopant atoms diffuse in the heterostructure and electrically contact the 2D hole gas, the samples are annealed at $\sim 440°$ C for 10 minutes in a reducing atmosphere. After the realization of the ohmic contacts, a 400 μm wide Hall bar is patterned on the sample (shaded area in Fig. 4.6) using e-beam lithography and wet etching. Following to the Hall bar patterning, a metallic top gate is evaporated on the sample. The top gate is realized by e-beam lithography and lift-off. A metallic back gate that covers the entire sample's rear can also be added[1].

Carbon paint thermometers [19] are deposited on the sample's surface as shown in Fig. 4.6. Two gold wires with a diameter of 25 μm are embedded in each carbon paint thermometer to measure their resistance. In order to optimally probe the sample's T, the gold wires need to be as

[1]The fabrication techniques used to prepare the thermopower samples (e-beam lithography, wet etching, gate deposition,...) are similar to those used to fabricate the open QDs. See Sec. 3.2 for details.

close as possible to the sample's surface. The procedure used to prepare the thermometers is the following. The gold wires are placed on the sample's surface and attached to the sample's egdes using photoresist. Then, the carbon paint drop is deposited on the wires at the center of the sample and dried under ambiant conditions overnight. As shown in Fig. 4.7(a), the T-dependence of the carbon paint thermometer's resistivity makes them particularly suitable for low T measurements. In order to optimize the T measurement in the range 30 - 500 mK, the thermometers' resistance has to lie beetween ~ 70 and $\sim 120\ \Omega$ at room T.

For thermopower measurements, a controlled thermal gradient has to be applied to the sample. To that purpose, the measurements are performed under vacuum. One end of the sample is thermally anchored to the cold finger of the MC of a dilution refrigerator[2](heat sink), while a strain gauge used as heater[3] is glued on the other end of the sample (see Fig. 4.6). The anchorage of the sample to the cold finger and to the heater is performed using 7031 GE varnish. A piece of cigarette paper soaked in GE varnish is intercalated between the back gate and the cold finger to avoid electrical contact.

4.5.2 Thermometry

Once the systems have been cooled down, the thermometers are first calibrated. In order to improve the quality of the T measurements, we make two different calibrations, below and above 200 mK. The calibrations are performed by recording the thermometers' resistance, while the MC's T is slowly rised by increasing MC's heater power by 0.1% every 3s. The resistance of a carbon paint thermometer as a function of T is shown in Fig. 4.7(a) for the entire investigated T-range. The carbon paint thermometers' resistance is measured in a two-contact configuration using PAR 124A lock-in amplifiers. As this resistance goes up to $\sim 10\ \mathrm{M}\Omega$ at low-T (see Fig. 4.7(a)), we use very low frequency of ~ 4 Hz in order to avoid signal cutting by the RLC filters[4]. The relation of the temperature to the thermometers' resistance is then determined by fitting the data to a polynomial law, using the following equation:

$$\ln T = \sum_i C_i \left(\ln R\right)^i , \tag{4.20}$$

[2]The low-T measurement system is described in Sec. 3.2.3.1.

[3]The heater is a 1 mm long strain gauge with a resistance of 120 Ω (QLFA model) purchased from Tokyo Sokki Kenkyujo Co.,Ltd., 8-2, Minami-Ohi 6-Chome, Shinagawa-Ku, Tokyo, 140-8560 Japan.

[4]See Sec. 3.2.3.1 for details about the filters.

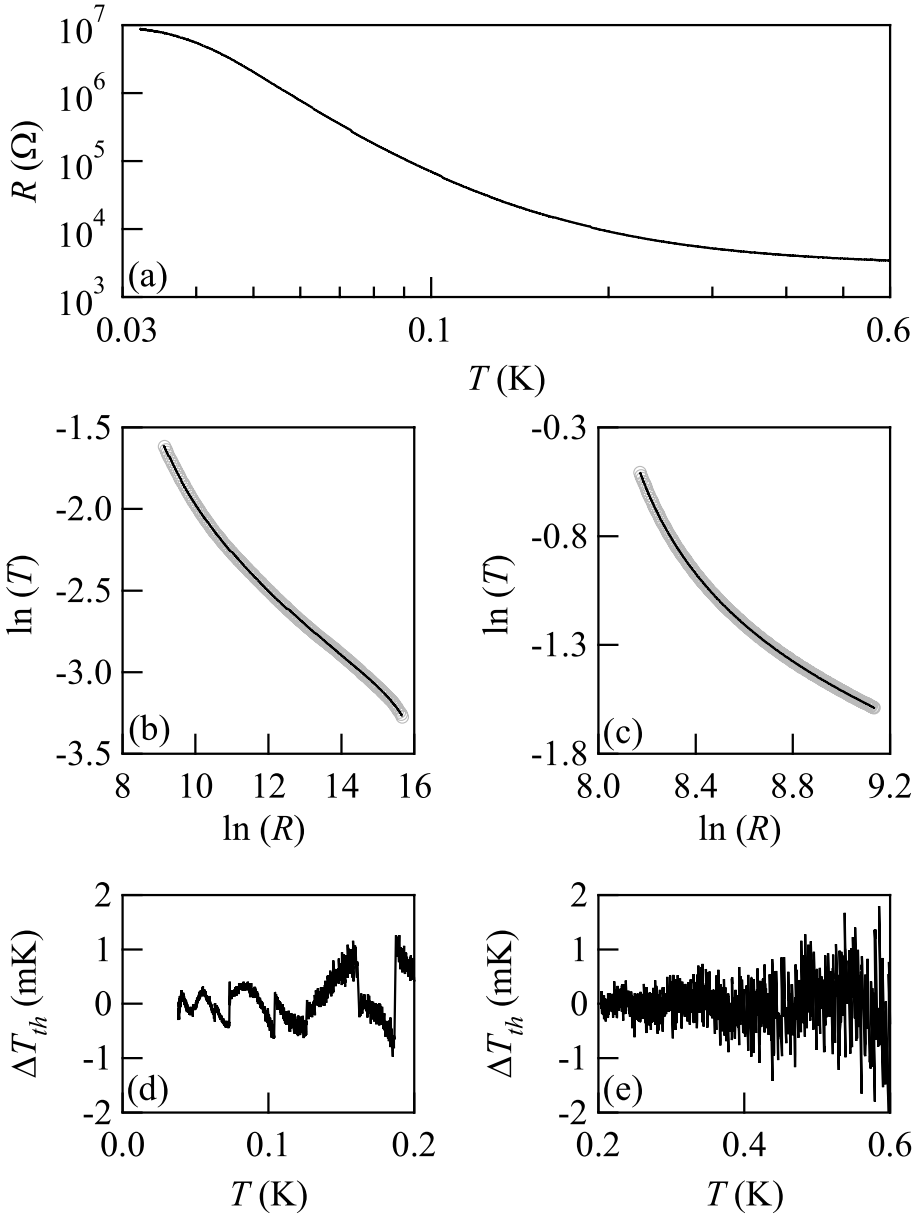

Figure 4.7: (a) Resistance as a function of T of a carbon paint thermometer. (b) and (c) Calibration curves for the carbon paint thermometer. Fits were done using Eq. (4.20) for $T < 200$ mK (b) and $T > 200$ mK (c). Temperature difference ΔT_{th} measured between the carbon paint and MC's thermometers for T below (d) and above (e) 200 mK.

where C_i are constants. The number of terms in the polynoms is adjusted to optimize the fit. Figure 4.7(b) and (c) present the fits of $\ln T$ vs $\ln R$ (open circles) above and below 200 mK, respectively. The quality of the calibrations can be checked by monitoring the temperature difference ΔT_{th} measured between the carbon paint and MC's thermometers. Figures 4.7(d) and (e) show ΔT_{th} for the fits presented in Figure 4.7(b) and (c), respectively, revealing that it is less than 1 mK in the investigated range. It is worth noting that the jumps observed in ΔT_{th} below 200 mK correspond to the change of the lock-in amplifier's range. These jumps are reproducible and are also similar for the two different lock-in amplifiers. Consequently, if the range of the lock-in amplifiers measuring the resistances of the two carbon paint thermometers are switched together, the effect of these jumps cancels when calculating the gradient across the sample. The accuracy of the T difference between the two carbon paint thermometers is then generally better than 0.5 mK for temperatures below 200 mK.

The thermopower measurements are performed using an ac technique. Consequently, the thermal gradients can not be measured simultaneously with S. It is then necessary to first characterize the thermal gradient that establishes along the sample for a given power in the heater and a given T. The thermal characterization of the sample is realized at $B = 0$ T and proceeds as follows[5]. Once the MC's T has been adjusted to the desired value, we apply a dc voltage V^{dc}_{heater} to the heater in series with a resistor[6] and record the evolution of the carbon paint thermometers' T for several values of V^{dc}_{heater}. This procedure is repeated for a series MC's T included between 40 and 500 mK. The T difference between the voltage probes ΔT is given by

$$\Delta T = \frac{L_{oc}}{L_{th}} \left(T_{hot} - T_{cold} \right), \tag{4.21}$$

where T_{hot} and T_{cold} are the temperatures of hot and cold side carbon paint thermometers, respectively (see Fig. 4.6). As the thermometers do not measure T exactly at the position of the voltage probe, we assume that the thermal gradient is constant along the sample and correct the measured T difference by a geometrical factor L_{oc}/L_{th}, where L_{oc} is

[5] If an In back gate is used, the thermal characterization is also performed at $B = 0.1$ T. Indeed In becomes superconductor below 3.4 K and has a critical field of ~ 0.029 T at $T = 0$ K. The superconductor/metal transition of the In back gate changes the overall thermal conductivity of the sample and modifies the thermal gradient along the sample.

[6] Typically, at 100 mK, a current of 5 μA is the heater, corresponding to a power of 3 nW, produces a ΔT of $\sim$ 5 mK. At 500 mK, a current 58 μA in the heater, corresponding to a power of 0.4 μW, leads to a ΔT of $\sim$ 10 mK.

the distance between the ohmic contacts used as voltage probes for the thermopower measurements and L_{th} is the distance between the carbon paint thermometers. The mean sample temperature T_m is given by

$$T_m = \frac{T_{hot} + T_{cold}}{2}. \tag{4.22}$$

Note that ΔT is always kept below 10% of T_m and below 10 mK.

4.5.3 Thermopower measurement

For the thermopower measurements, the thermal gradient is created by passing a sine wave current at a frequency $f = 1.3$ Hz through the heater and the voltage signal is measured at $2f$ between two contacts on the same edge of the sample using a Signal Recovery 5210 lock-in amplifier. The value of the frequency is chosen to be low enough to let the system thermally follow the heater excitation. The integration time was adapted depending on the magnitude of the measured thermopower signal: we used values from 3 to 30 s for the smallest signals. As the value of the thermal gradient was previously determined by appying a dc voltage V^{dc}_{heater} to the heater in series with a resistor, one must be careful to convert this dc value to the corresponding rms voltage provided by the output of the lock-in amplifier V^{rms}_{heater} using:

$$V^{rms}_{heater} = \frac{V^{dc}_{heater}}{\sqrt{2}}. \tag{4.23}$$

Similarly, the thermoelectric voltage measured using the lock-amplifier V^{rms}_{TP} has to be converted to a dc value:

$$V^{dc}_{TP} = 2\sqrt{2}V^{rms}_{TP}. \tag{4.24}$$

The thermopower S is then calculated using:

$$S = \frac{V^{dc}_{TP}}{\Delta T}. \tag{4.25}$$

It is worth noting here that our measurement technique implies that we probe S along the length of the sample. Two different samples are then required to measure the thermopower for two different crystallographic directions.

For magnetothermopower measurements, the magnetic field is always swept from the high-B end-point down to zero. The sweep rate is adapted to the integration time used for the data acquisition, as well as to ensure the thermal stability of the system. We generally sweep B at a rate between 0.01 and 0.05 T/min.

To finish this chapter, it is worth summarizing the essential assumptions that were made to measure thermopower data that are presented in the following two chapters:

- While thermopower is an intrinsic property of the considered material, the measurement set up implies that the measured S contains contributions from the sample S_{sample} as well as from the measurement wires S_{wires}. Indeed, as the temperature differences along the two measurement wires are not identical, it can be shown that the measured S is given by the following relation: $S = S_{sample} - S_{wires}$. However, since the thermopower of gold, used for the measurement wires, is extremely small at low T, we assume that $S_{wires} \approx 0$.

- The carbon paint thermometers are in thermal equilibrium with the sample and the thermal gradient is constant between the thermometers. To reduce heat conduction through the gold wires used to measure the resistance of the thermometers, they are connected to the DIP socket through $\sim$ 15 mm long segments of Nb/Ti superconducting wires.

- The thermal gradient is small enough to ensure that S is measured in the linear regime.

- The thermal gradient is independent of B. This assumption is well respected as the main heat conduction mechanism through the samples comes from the GaAs lattice.

- The carriers are in thermal equilibrium with the lattice. We have seen in Sec. 3.2.3.2 that, due to the reduction of hole-phonon interaction with decreasing T, the holes' T can deviate from the temperature of the lattice at very low T. This deviation can weakly modify the T-dependence of the measured thermopower below 100 mK. However, it does not change the global S vs T behaviour and it does not affect the conclusions of the following chapters.

Chapter 5

Parallel magnetic field-induced metal-insulator transition

N'a de convictions que celui qui n'a rien approfondi.

E. Cioran

5.1 Introduction

The past two decades have witnessed extensive theoretical and experimental work on the subtle interplay between disorder and carrier-carrier interaction that dictates the low temperature T behavior of two-dimensional systems in semiconductor structures [2, 114, 173, 48]. Within the scaling theory of localization [1], carriers in non-interacting 2D systems with disorder have been predicted to be localized. In such systems, the resistivity is expected to increase logarithmically or exponentially as $T \to 0$ for weak and strong localization, respectively. It has been shown that in the presence of weak carrier-carrier interaction the localization should be strengthened [10]. On the other hand, strongly interacting 2D systems are expected to form a Wigner crystal at low T [182, 200]. Due to the unavoidable presence of disorder in 2D semiconductor structures, the Wigner crystal should be pinned and the system should not conduct at $T = 0$. Based on these theoretical predictions, 2D systems have for a long time been expected to solely behave as insulators.

In the early 1980s, experimental investigations [28] provided evidence of a logarithmic increase of the resistivity in agreement with the localization theory.

In the 1990s, a striking metallic T-dependence of the resistivity was reported in Si-MOSFETs [113]. This observation was made in a low density 2D system with much higher mobility than those previously available. Following this seminal work, similar data have been recorded for 2D systems in various materials, including n-GaAs/AlGaAs heterostructures [90], p-GaAs/AlGaAs heterostructures [89], p-SiGe heterostructures [42], n-AlAs heterostructures [151] and n-GaAs FETs [119]. However, the density and T ranges where the metallic behaviour is observed have been shown to be material dependent. The strong metalliclike T-dependence of the resistivity, as well as the low density range where this metallic regime is observed, first suggested the formation of a new metallic phase stabilized by strong carrier-carrier interaction[1].

If the carrier density is further reduced, such metalliclike 2D system is driven through a metal-insulator transition (MIT) [113]. Deep in this insulating state, the T-dependence of the resistivity is consistent with with hopping in the presence of a Coulomb gap (Efros-Shklovskii VRH). Interestingly, when a parallel magnetic field $B_{\|}$ is applied to the system, a huge positive magnetoresistance is observed in both the metallic and in the insulating state [177]. The magnetoresistivity first strongly increases as $\sim B_{\|}^2$ and saturates once the minority spin subband has been depopulated [194, 186]. Moreover, it was found that $B_{\|}$ also destroys the metallic behavior, suggesting that the MIT could be related to carriers' spin.

Many different conjectures have been proposed to describe the metallic behavior of 2D systems and the transition to an insulating state at lower densities or in the presence of $B_{\|}$. The two prominent theses for the description of the metallic regime observed in 2D systems are based on the Fermi liquid theory. The first one describes the metallic behavior as arising from a dependence upon T, $B_{\|}$, n_{2D} of the screening of the charged impurity potential [48, 47]. The second, on the other hand, explains the strong metallic T-dependence as stemming from the delocalizing effects caused by strong carrier-carrier interaction [164, 209]. Within this theory, a strong $B_{\|}$-induced positive magnetoresistance is expected as $B_{\|}$ quenches the delocalizing effects of the carrier-carrier interaction by aligning the spins. Nevertheless, these Fermi liquid-based theories do not explain the strong increase of the effective carrier mass that has been reported in the vicinity of the density-induced MIT [174, 175]. Several

[1]The strength of carrier-carrier interaction can be probed by the ratio of the Coulomb energy to the Fermi energy: $r_s = \frac{m^* q^2}{4\pi\hbar^2 K\sqrt{p\pi}}$, where K is the dielectric constant. The carrier-carrier interaction is supposed to be weak for $r_s \ll 1$ and strong for $r_s \gg 1$.

other models have been developed to describe the ground state of 2D systems close to the MIT (for a review, we refer to Refs. [2, 114, 173]).

Most experiments performed to study the MIT in 2D systems consist of electrical transport measurements and only poor attention has been paid to the other electronic properties of these systems. The study of the carriers' specific heat, for example, could contribute to decrypt the nature of the MIT. In fact, one of the fundamental thermodynamic quantities, the compressibility, has been adressed experimentally across the MIT. The compressibility measures the ability of the system to screen external charges. Macroscopic measurements of the compressibility as a function of the carrier density in 2D p-type GaAs heterostructures have shown a sign reversal from negative to positive value at the MIT [54]. While the negative value and the p-dependence of the compressibility in the metallic regime are well understood by the Hatree-Fock theory [58, 76], its behaviour in the insulating regime, the sign reversal and the vanishing value at low-p, first suggested a phase transition to an incompressible state, possibly a Wigner crystal [54]. Soon after, further measurements of the local compressibility in similar systems have confirmed the behavior of the compressibility in the metallic regime, as well as the presence of a thermodynamic change at the p-induced MIT [76]. These measurements, however, have shown that the behavior of the compressibility in the insulating regime is spatially inhomogeneous. Moreover, local measurements of the compressibility exhibit clear signatures from the charge traps in the doping layer, highlighting their important role in the systems' thermodynamic ground state. Finally, similar local compressibility measurements have been performed on 2D GaAs FETs that do not contain any intentional dopants [77]. Results in these systems confirms the presence of a thermodynamic change at the MIT and suggested the presence of two phases in the insulating regime: a continuous compressible phase and an incompressible, discrete phase. As the carrier density is reduced, the discrete phase grows to the detriment of the continuous compressible one. The compressibility results have emphasized the inhomogeneous nature of the p-induced insulating phase and have highlighted the importance of sample's parameters, like the presence of charge traps in the doping layer, in the determination of the thermodynamic ground state.

Up to now, no clear, universally accepted understanding has been established and the nature of the metallic phase and of the MIT are still hotly debated. The main difficulty arises from the fact that the true nature of the system's ground state can only be probed at $T = 0$. Within this context, it is worth noting that very recent investigations have reported the disappearance of the metallic behavior in 2D GaAs

FETs below 30 mK [95], indicating that the true system's ground state is probably insulating.

In the previous chapter, we have seen that the diffusion thermopower is sensitive to the density of states at the Fermi level. For a metallic 2D system, made of a degenerate 2D hole gas, S^d can be expressed in terms of the conductivity σ using the Mott formula:

$$S^d = \frac{\pi^2 k_B^2 T}{3qE_F}(1+\alpha)\,. \tag{5.1}$$

where α describes the energy dependence of the scattering mechanisms. Assuming that α is T-independent, the diffusion thermopower of metallic 2D systems decreases linearly with T. For insulating 2D systems, we distinguish three different cases. First, if an energy gap separates the ground state from its excitations, S^d diverges as T^{-1} when T is lowered (Eq. (4.9)). Second, for systems with a mobility gap, S^d should vanish as $S^d \propto T^{1/3}$ at low T if the transport occurs through Mott VRH (Eq. (4.12)). Finally, if the system presents a Coulomb gap and Efros-Shklovskii VRH is responsible for transport, S^d exhibits a constant value (Eq. (4.15)). Thermopower is then particularly suitable to study the MIT in 2D systems as it can precisely determine the nature of system's ground state and provides valuable information concerning the dominant scattering mechanisms.

In this chapter, we study dilute (311)A GaAs 2D hole systems through magneto-thermopower measurements along the $[01\bar{1}]$ and $[\bar{2}33]$ crystallographic directions. Our results indicate that, below 150 mK, in the diffusion regime, S decreases linearly with T at low $B_\parallel$, as expected for a metallic system. Interestingly, at high $B_\parallel$, in the insulating phase, S drops and saturates to zero for the $[\bar{2}33]$ direction, while for the $[01\bar{1}]$ direction it changes sign. This remarkable behavior suggests that the system's ground state is not modified when it is driven through the MIT, instead, it shows that the apparent MIT is accompanied by a dramatic change in the dominant scattering mechanism. In particular, we cast our data within the screening model [80, 48] and explain the negative thermopower in terms of $B_\parallel$-dependent interface roughness and intersubband scattering [63].

5.2 Sample description

The samples investigated in this chapter are two 8×2 mm^2 rectangular pieces from a p-type GaAs/AlGaAs heterojunction grown by molecular beam epitaxy on (311)A. The heterojunction has been fabricated in

the group of Prof. M. Shayegan at Princeton University. A schematic layout of its structure is available in Appendix C, where it is referred to as M230. The heterojunction has a hole density $p = 4 \times 10^{14}$ m^{-2} and exhibits a mobility anisotropy [91] stemming from the mesoscopic corrugation of the (311)A GaAs/AlGaAs interface [197]. The mobilities are $\mu = 38$ m^2/Vs along the [$\bar{2}33$] (high-μ) and 18 m^2/Vs along the [$01\bar{1}$] (low-μ) directions at 1.5 K.

In order to study ρ and S along the two crystallographic directions, one sample had its length along the high-μ direction and the other one along the low-μ direction. The samples were prepared as described in Section 4.5.1.

Since the response of a 2D GaAs hole system to $B_\parallel$ depends on the orientation of the magnetic field with respect to the crystal axes [150, 186], $B_\parallel$ was always kept parallel to [$\bar{2}33$]. This particular configuration and the low carrier density of 1.9×10^{14} m^{-2} chosen for the experiments, allow the observation of MIT and subband depopulation at lower $B_\parallel$'s. This makes the thermopower measurements easier as the required thermal stability is more difficult to achieve when sweeping at very high-$B_\parallel$'s in our experimental set-up. Moreover, it precludes any spurious superposition of the MIT with the Shubnikov-de Haas oscillations appearing at high-$B_\parallel$ due to a small misalignment between the sample and the magnetic field. Finally, note that while most of the data presented in this chapter were recorded for $p = 1.9 \times 10^{14}$ m^{-2}, similar results were obtained at $p = 2.3 \times 10^{14}$ m^{-2}.

5.3 Magnetotransport measurements

We first present magnetotransport measurements performed at $p = 1.9 \times 10^{14}$ m^{-2} and show ρ as a function of $B_\parallel$ at various temperatures and for current along both crystallographic directions in Fig. 5.1(c). At $B = 0$, ρ exhibits a metallic behavior[2]. By sweeping up $B_\parallel$, ρ first strongly increases for both directions and displays an insulating behavior above a critical magnetic field $B_\parallel^c \sim 1.7$ T. The T-dependence of ρ at various $B_\parallel$ in the metallic and in the insulating regime is further illustrated in Fig. 5.1(a) and (b) for the low-μ and the high-μ crystallographic directions, respectively. When $B_\parallel$ is further raised, the ρ variation slows down and increases approximately linearly for $B_\parallel \gtrsim B_\parallel^d \sim 2.7$ T, corresponding

[2]The ratio of the Coulomb energy to the Fermi energy, r_s, is equal to 22.8 in our sample for $p = 1.9 \times 10^{14}$ m^{-2}, using $m^* = 0.38\ m_e$.

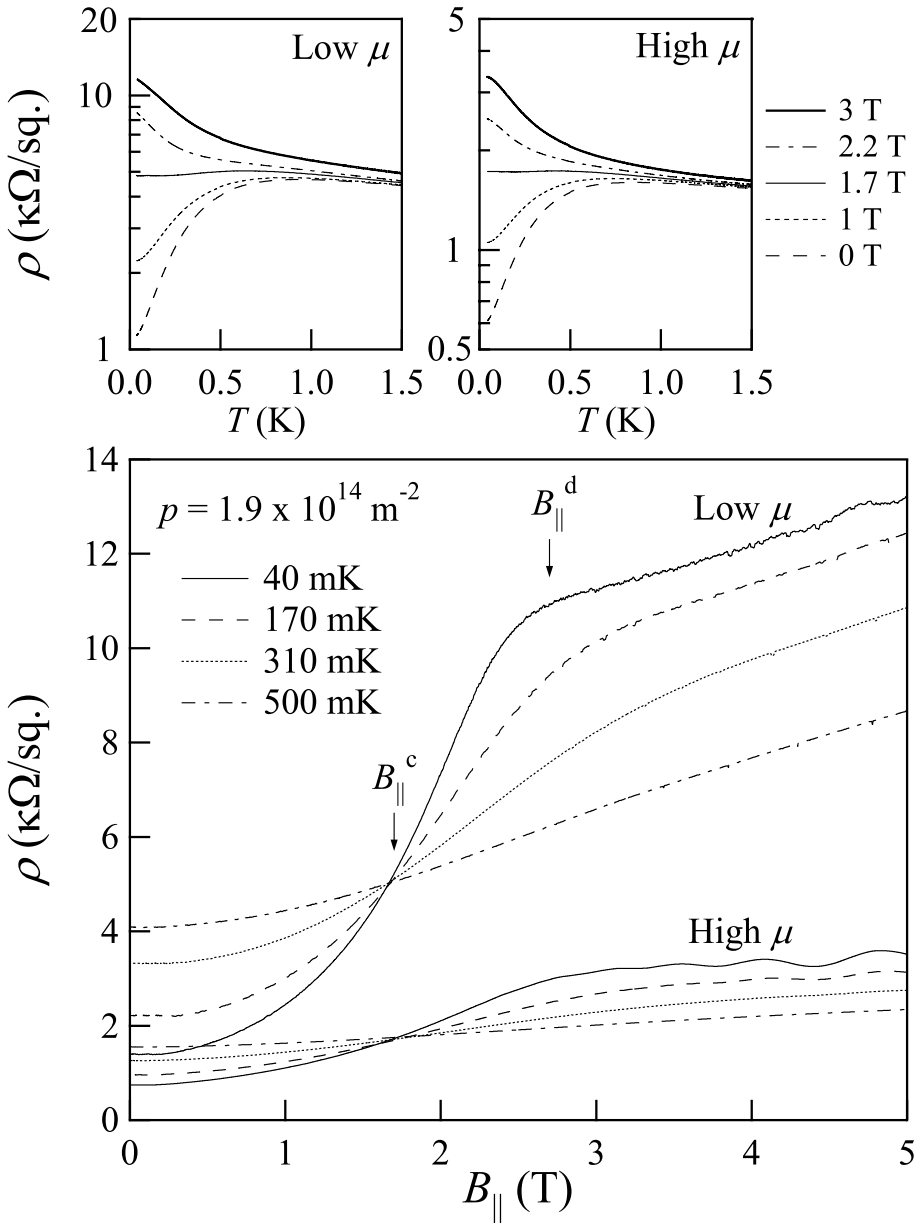

Figure 5.1: Temperature dependence of ρ along (a) the low-μ and (b) the high-μ crystallographic directions for $p = 1.9 \times 10^{14}$ m^{-2} and $B_{\|} = 0$, 1, 1.7, 2.2 and 3 T. (c) Longitudinal resistivity as a function of $B_{\|}$ at various T's for $p = 1.9 \times 10^{14}$ m^{-2}. Data are shown with the current applied along two crystallographic directions (high-μ and low-μ).

to the complete depopulation of the minority spin subband [194, 186][3]. The behavior of ρ as a function of $B_{\parallel}$ and T observed here is typical for dilute 2D carrier systems and is similar to that previously reported in the literature.

Within the screening model [48, 47], the strong increase of the resistivity for $B_{\parallel} < B_{\parallel}^{d}$ is ascribed to the reduction of screening of the charged impurity potential due to the depopulation of the minority spin subband. The slower increase of ρ for $B > B^{d}$ is attributed to the magneto-orbital effect originating from the finite width of the 2D system [46, 188]. If we compare data obtained for the two different crystallographic directions, we observe that the ratio $\rho(B_{\parallel}^{d})/\rho(0)$ at 40 mK is ~ 4 and ~ 8 along the high- and low-μ directions, respectively. Theoretically, this ratio has been predicted to have a maximum value of 4 [47], but larger values have already been reported for low density Si-MOSFETs [177]. Recent experimental studies have suggested that the large values of $\rho(B_{\parallel}^{d})/\rho(0)$ could be related to interface roughness scattering [115]. This explanation seems consistent with our observation, since for (311) p-type GaAs heterojunctions interface roughness scattering is known to play a more important role along the low-μ direction compared to the high-μ direction [91].

5.4 Magnetothermopower measurements

The T-dependence of S at various $B_{\parallel}$ is presented in Fig. 5.2 and Fig. 5.3 for $p = 1.9 \times 10^{14}$ m^{-2} and for both crystallographic direction. We first focus on S at low-B ($\lesssim B_{\parallel}^{c}$). At T's between 500 mK and ~ 200, S decrease as T^4 when T is lowered. This behavior is consitent with low-T phonon-drag thermopower in a 2D system with screened piezoelectric coupling [124]. Below ~ 150 mK, S decrease linearly with T and behaves as expected from the diffusion thermopower of a 2D degenerate hole gas. The low-B behaviour of S, *i.e.* the T-dependencies and the T transition from phonon-drag to diffusion thermopower is consistent with previous experiments on GaAs/AlGaAs heterostructures [64, 137, 183].

When $B_{\parallel}$ is increased, we observe that, for $T \gtrsim 0.2$ K, S remains $\propto T^4$. Below 0.15 K, $S \propto T$ for $B_{\parallel} \lesssim B_{\parallel}^{c}$ and both crystallographic directions. However, the behavior of S change drastically when $B_{\parallel} \gtrsim B_{\parallel}^{d}$. Indeed, at magnetic fields higher than $B_{\parallel}^{d}$, the diffusion thermopower

[3]Note also that for $B_{\parallel} > B_{\parallel}^{d}$, ρ shows Shubnikov-de Haas oscillations, caused by a small misalignment of the 2D hole gas with respect to $B_{\parallel}$. From these oscillations, we deduce that the misalignment is smaller than 1.5° for both samples.

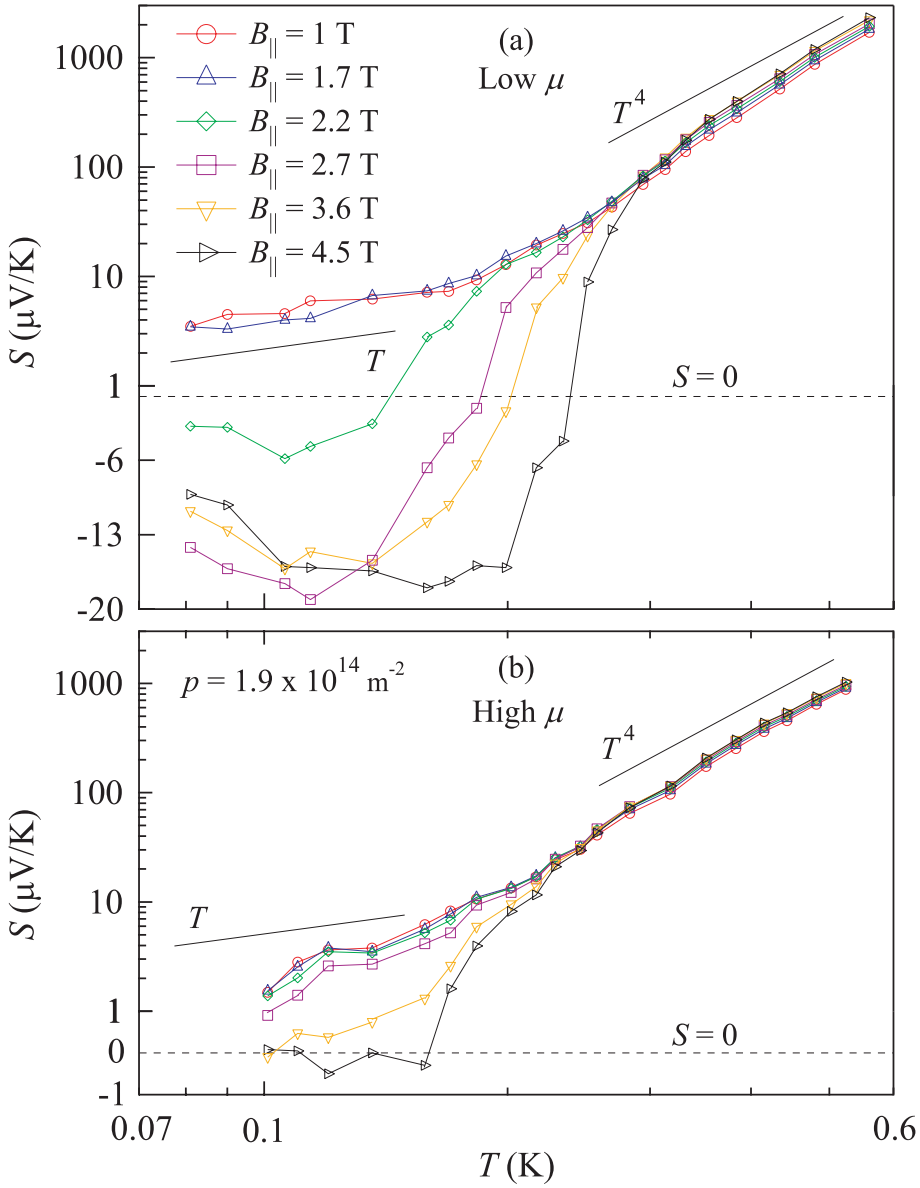

Figure 5.2: Temperature dependence of S at different magnetic fields and $p = 1.9 \times 10^{14}$ m^{-2} for (a) the low-μ and (b) the high-μ direction. Data are plotted on a logarithmic scale for $S \geq 1$ and on a linear scale for $S \leq 1$. The dashed lines correspond to $S = 0$ and the solid lines indicate various temperature dependencies.

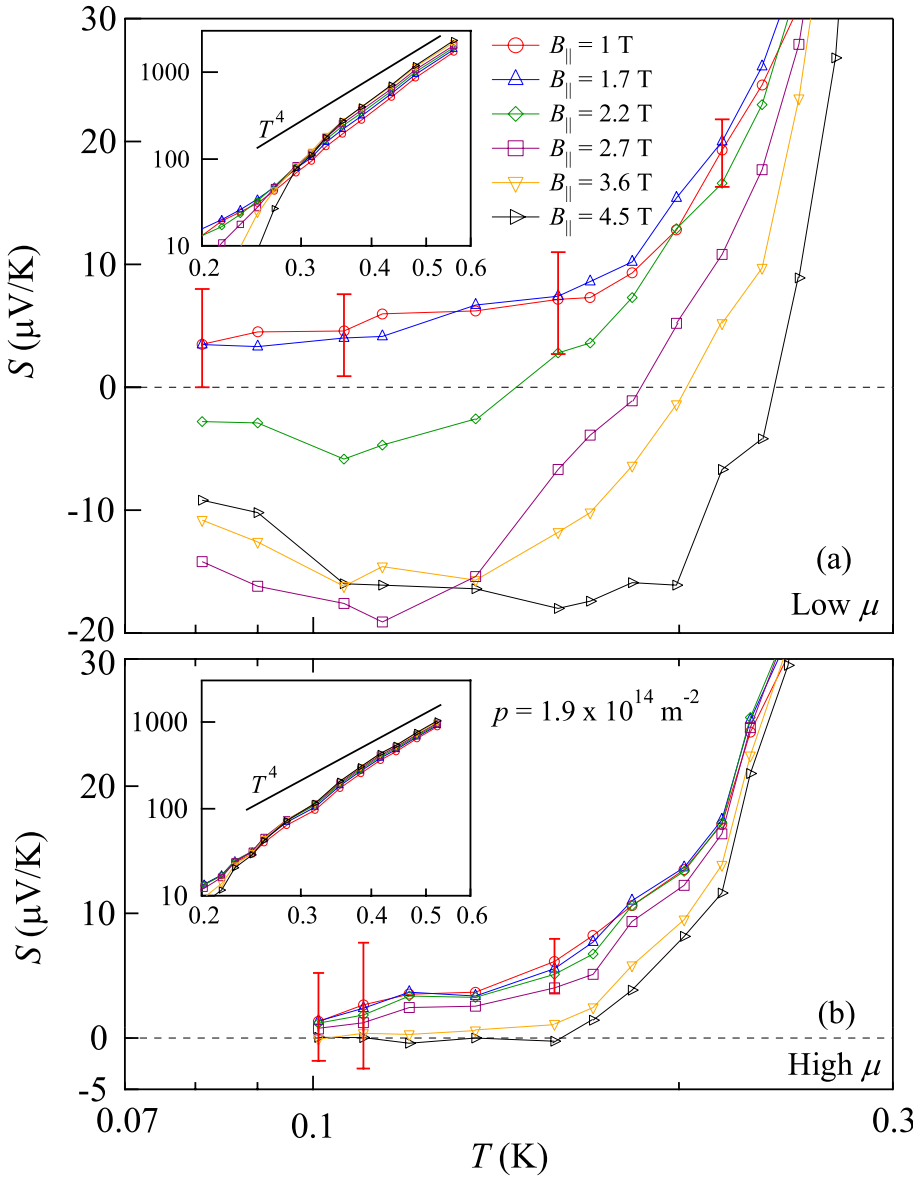

Figure 5.3: Temperature dependence of S at different magnetic fields and $p = 1.9 \times 10^{14}$ m^{-2} for (a) the low-μ and (b) the high-μ direction. The main panels present the low-T data. The insets show the thermopower in the phonon-drag regime. The dashed lines correspond to $S = 0$. The error bars are given by the noise of the lock-in amplifier, the magnitude of the applied thermal gradient, and the accuracy of the thermometers' calibration.

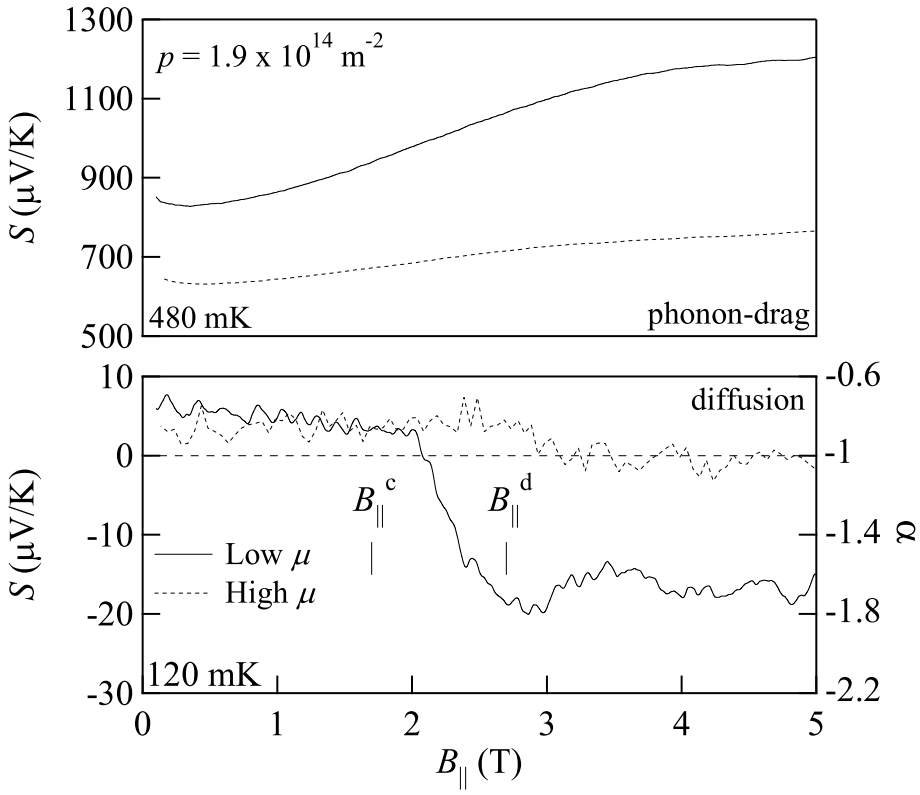

Figure 5.4: Thermopower as a function of $B_\parallel$ for the low-μ (solid traces) and the high-μ (dotted traces) directions at two different temperatures and $p = 1.9 \times 10^{14}$ m^{-2}. The dashed line in the bottom panel indicates $S = 0$. In the lower panel, the corresponding value of α is shown on the rigth axis.

drops to zero along the high-μ direction, and becomes negative along the low-μ direction.

The unexpected behavior of S^d at high-$B_\parallel$ is further illustrated in Figure 5.4 which displays S as a function of $B_\parallel$ at two different temperatures for $p = 1.9 \times 10^{14}$ m^{-2} and for the two crystallographic directions. At 480 mK, in the phonon-drag regime, S behaves similarly to ρ: it increases monotonically with $B_\parallel$ for both crystallographic directions. On the other hand, at 120 mK where the diffusion contribution dominates, S has a small positive value at low-$B_\parallel$ and it is constant up to $\sim B_\parallel^c$. Interestingly, between $B_\parallel^c$ and $B_\parallel^d$, S drops to zero along the high-μ direction, while for the low-μ direction it decreases more dramatically and reverses its sign. For $B_\parallel \gtrsim B_\parallel^d$, S remains constant for both crystallographic directions.

5.5 Discussion

None of the models developed for 2D insulators can succesfully describe the intriguing behavior of S observed for $B_{\parallel} \gtrsim B_{\parallel}^{c}$. First, the vanishing S as $T \to 0$ is not consistent with the presence of an energy gap in the ground state. Second, the difference observed between the two crystallographic directions cannot be described within theories developed for Mott or Efros-Shklovskii VRH. Moreover, for VRH transport, S^{g} has been predicted to be equal to zero [215], contradictory to our results. On the other hand, the behavior of S^{d} above $B_{\parallel}^{c}$, *i.e.* the sign anomaly and the anisotropy, can be explained using Eq. (5.1) provided that $B_{\parallel}$ induces a dramatic change in the dominant scattering mechanism. As illustrated in the lower panel of Fig. 5.4, the deduced $\alpha \sim -0.8$ at low $B_{\parallel}$ decreases to ~ -1 and ~ -1.7 along the high-μ and low-μ directions, respectively.

Sign anomalies of the diffusion thermopower have also been reported at $B = 0$ in high-density electron GaAs/AlGaAs heterojunctions and Si inversion layers [75, 169], as well as in the metallic-like phase of p-type GaAs quantum wells [137] and Si/SiGe heterostructures [159] in the vicinity of the MIT. They have been attributed to the onset of the second subband population or to interface roughness scattering. In particular, the diffusion thermopower of dilute p-type GaAs quantum wells has been addressed theoretically within the screening theory [125]. In this work, the effect of several scattering mechanisms, including scattering by charged and neutral impurities, alloy disorder, interface-roughness as well as electron-phonon scattering, have been carefully considered. It has been shown that interface-roughness scattering with long range interface layer-fluctuations is the only scattering mechanism with an energy dependence that can explain the sign reversal of S observed in p-type GaAs quantum wells close to the MIT. Similar arguments could be invoked to interpret the behaviour of S observed in our heterojunction for $B_{\parallel} \gtrsim B_{\parallel}^{c}$. The in-plane magnetic field can modify the scattering through two different mechanisms. First, it pulls the hole's wave function closer to the interface, thereby making roughness scattering more efficient. Second, $B_{\parallel}$ depopulates the minority spin subband and, as a result, modifies intersubband scattering. Moreover, the origin of the sign reversal of S as stemming from an increased strength of interface roughness scattering is consistent with the weaker effect observed along the high-μ direction.

Our thermopower data seem consistent with the screening model [48, 47] and suggest that the system's ground state is not modified across the MIT: the 2D system behaves as a degenerate hole gas both in the metallic and in the insulating states. Moreover, our results indicate that

at the MIT, $B_{\parallel}$ induces a dramatic change in the dominant scattering mechanism. However, due to the lack of theoretical calculations for the thermopower in strongly interacting systems, we can not exclude that hole-hole interaction may also play a significant role [209]. Within this context, additional experimental investigations on comparable 2D systems with less interface roughness scattering, like (100) C-doped p-type GaAs/AlGaAs heterostructures, could determine the importance of hole-hole interaction across the $B_{\parallel}$-induced MIT.

5.6 Heterojunction vs quantum well

To further illustrate the role of the interface scattering mechanism in the present measurements, we compare, in Fig. 5.5, S along the high-μ direction at ~ 100 mK and at $B = 0$ as a function of the carrier density for the heterojunction investigated here and for the quantum well studied in Ref. [137]. At high densities, the measured values of S are similar for both samples and increase monotonically when p is reduced. Between $p = 2$ and 3×10^{14} m^{-2}, S shows a sign anomaly in the quantum well, while for the heterojunction it remains positive and increases steadily. The solid line in Fig. 5.5 shows the value of S^d vs p calculated for a 2D degenerate hole gas using Eq. (5.1). The calculation was performed with $\alpha = 0.76$ and $m^* = 0.38\ m_e$. The measured S is in excellent agreement with the calculation down to $p \sim 3.5 \times 10^{14}$ m^{-2} for the quantum well and down to $p \sim 2 \times 10^{14}$ m^{-2} for the heterojunction. For $p \lesssim 2 \times 10^{14}$ m^{-2}, where the systems approach the MIT, the measured thermopower strongly increases for both samples.

Assuming that interface roughness scattering is the mechanism reponsible for the sign change of S at low T, the difference observed between the heterojunction and the quantum well at $B = 0$ can possibly be ascribed to the confinement of the holes' wave function. Indeed, the confinement is stronger in the quantum well and the holes' wave function is closer to the interface, making interface roughness scattering more dominant. Moreover, in quantum well structure there is an additional GaAs/AlGaAs interface in comparison to the case of the heterojunction. Figure 5.6 presents the mobilities and the T-dependencies of ρ as a function of p along the high-μ direction for both the heterojunction and the quantum well samples. The heterojunction sample has a much higher mobility than the quantum well sample (Fig. 5.6(a)), resulting in a stronger metallic behavior and a lower density for the MIT (Fig. 5.6(b) and (c)). This lower mobility measured for the quantum well seems consistent with a stronger interface roughness scattering. However, the

simple explanation given here has to be considered carefully. Indeed, it is not clear whether the differences observed in the electrical transport only stem from an increased strength of the interface-roughness scattering for the quantum well samples or if other parameters have to be accounted for. Further investigations are needed to clarify the problem.

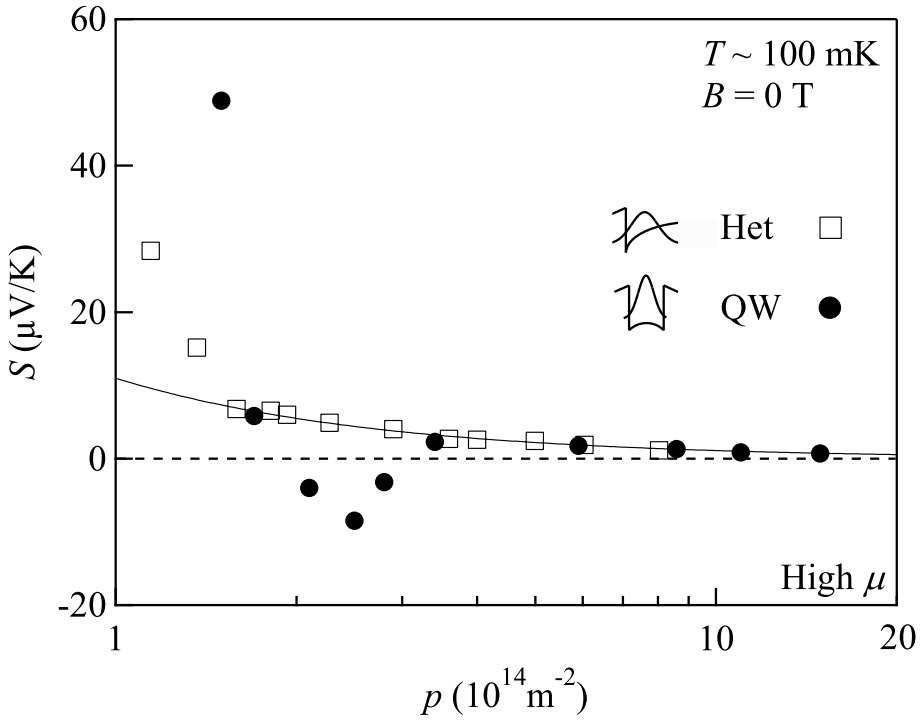

Figure 5.5: Thermopower as function of p along the high-μ direction at ~ 100 mK and at $B = 0$ for the heterojunction (Het) investigated in this chapter and for the quantum well (QW) studied in Ref. [137]. The solid line shows the expected value of S^d for a degenerate hole gas (Eq. (5.1)) at 100 mK with $\alpha = 0.76$.

Finally, we comment on the strong increase of S observed for $p \lesssim 2 \times 10^{14}$ m^{-2} for both samples. At these carrier densities, the measured behavior of S strongly deviates from what is extected from a degenerate hole gas using Eq. (5.1) (see Fig. 5.5). It is worth noting here that the thermopower signal was particularly noisy for data recorded at these densities, most probably because our low-f technique is not adapted to very low-p regime where the samples are strongly inhomogenous. However, the results seem consistent with data reported in the metallic phase of Si-MOSFETs [69] where similar increase of the diffusion thermopower was observed at densities just above the MIT. In that work, an upturn

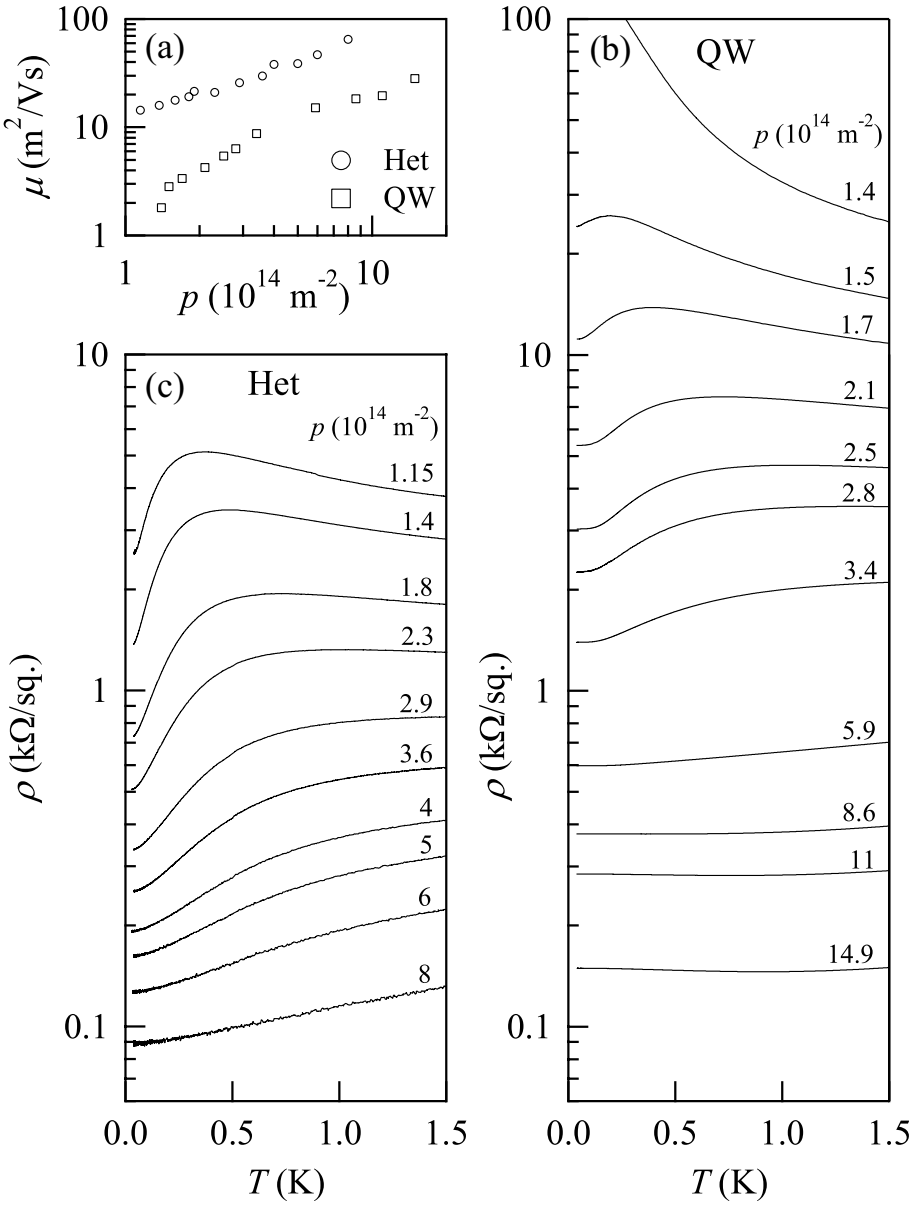

Figure 5.6: (a) Mobility determined at 1.5 K as a function of p along the high-μ direction for the heterojunction (Het) investigated in this chapter and for the quantum well (QW) studied in Ref. [137]. Panels (b) and (c) show the T-dependence of ρ at various carrier densities for the quantum well and the heterojunction, respectively.

to a T^{-1} dependence of S^d in the insulating phase was also measured down to the lowest investigated T (~ 300 mK). Such a T-dependence of S^d could be explained as stemming from thermally activated transport through an energy gap or a mobility gap. However, very low-T measurements are still required two distiguish between these to cases. Indeed S^d is expected to be constant or to behaves as $T^{1/3}$ at low-T for a mobility gap with and without carrier-carrier interaction, respectively. On the other hand, it should diverge as $T \to 0$ for an energy gap. It is also worth noting that no change in the behaviour of the phonon-drag thermopower has been observed across the MIT, inconsistent with a transition to VRH transport. However, these results are only reported for densities close to the MIT. More thermopower data deep in the insulating regime could certainly help determine the nature of the insulating phase.

5.7 Conclusion

In this chapter, we studied high mobility, dilute p-type (311)A GaAs heterojunctions subjected to an in-plane magnetic field. The resistivity of these samples first strongly increases as function of $B_\parallel$ and a MIT is observed at a critical magnetic field $B_\parallel^c$. Above $B_\parallel^d$ that corresponds to the depopulation of the minority spin subband, ρ saturates and increases linearly with $B_\parallel$.

We report thermopower measurements in the $B_\parallel$-induced MIT. The diffusion thermopower is a very suitable tool to investigate such MIT as it is directly sensitive to the system's ground state and the dominant scattering mechanism. For $B_\parallel \lesssim B_\parallel^c$, the low-$T$ thermopower, dominated by the diffusion contribution, behaves as expected for a degenerate hole gas and decreases linearly with T. However, S^d changes dramatically around the MIT. Along the high-μ direction S drops to zero, while for the low-μ direction it changes sign. This remarkable behavior indicates that the apparent MIT does not originate from a modification of the system's ground state. Instead, the MIT appears to be accompanied by a dramatic change in interface roughness and intersubband scattering mechanisms. These conclusions are strengthened by the results obtained in the phonon-drag regime that do not exhibit any change of S across the MIT.

Chapter 6

Reentrant insulating phase in bilayer hole systems

> La vraie science est une ignorance qui se sait.
>
> *Montaigne*

6.1 Introduction

In chapter 1, we described 2D carrier systems as degenerate Fermi gases of non-interacting particles. However, the realization of 2D systems with extremely low disorder has allowed the Coulomb interaction between carriers to become a major parameter in the determination of the system's ground state. With the emergence of the carrier-carrier interaction, many peculiar many-body ground states have been observed experimentally and were described theoretically as arising from the subtle interplay between Coulomb interaction, disorder, and magnetic field [49].

The signatures of several many-body states, generally observed in clean 2D carrier systems, are observed in Fig. 6.1 that shows the longitudinal resistivity of a 2D GaAs hole system[1] with $p = 4.2 \times 10^{-14}$ m^2 as a function of a perpendicular B. Quantum Hall states (QHSs) are observed at fractional filling factors like $\nu = \frac{2}{3}$, $\frac{3}{5}$, $\frac{2}{5}$ and $\frac{1}{3}$. Such states are not expected for non-interacting systems. The first observation of a QHS at fractional ν was performed in 1982 at $\nu = \frac{1}{3}$ in a 2D GaAs electron system [185]. Since then, many other QHSs have been reported

[1] The traces presented in Fig. 6.1 were measured from the M230 heterostructure (see Appendix C).

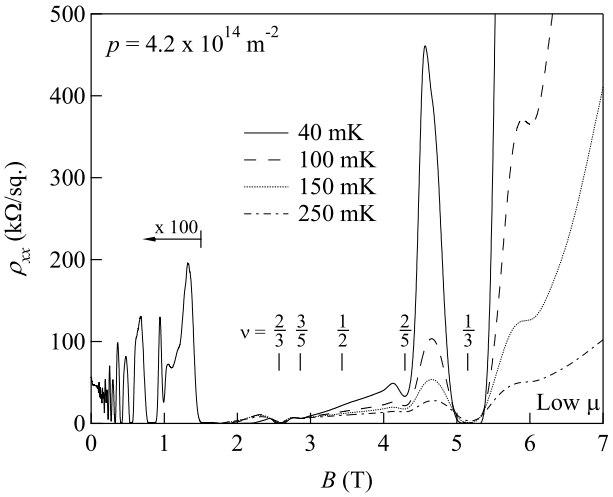

Figure 6.1: Longitudinal magnetoresistivity of a 2D GaAs hole system with $p = 4.2 \times 10^{-14}$ m^2. Below $B = 1.5$ T, the data are multiplicated by 100 for clarity. The various T traces plotted for $B > 1.5$ T illustrate the reentrant insulating phase around the fractional QHS at $\nu = 1/3$.

at fractional filling factors with odd denominators [49]. At these particular ν's, the carriers have been shown to condense into a liquid-like state that presents an energy gap in its excitation spectrum. Contrary to the case of the integer QHE, this gap does not stem from the quantization into LLs, but rather originates in the Coulomb interaction between the carriers[2].

A second intriguing feature illustrated in Fig. 6.1 is the insulating (IP) phase observed around the fractional QHS at $\nu = \frac{1}{3}$. Wigner predicted that interacting carriers in metals should crystallize if they have no kinetic energy [200]. In low-disorder 2D systems, a sufficiently large perpendicular B is expected to quench the kinetic energy of the carriers, leading to the formation of a Wigner crystal [49]. The reentrant IPs observed at low-T in GaAs 2D electron single-layers [49, 81, 104] around the fractional QHS at $\nu = \frac{1}{5}$ and electron bilayers [126] in the vicinity of total filling factor $\nu = \frac{1}{2}$, as well as in dilute, single-layer, GaAs 2D hole systems [171] near $\nu = \frac{1}{3}$ have been attributed to the formation of pinned

[2]Theoretically, the fractional quantum Hall effect was first described using a set of non-interacting quasi-particles with fractional charges [117]. More recently, a second description of the effect was proposed, where the interacting carriers are replaced by non-interacting quasi-particles made of a carrier attached to an even number of quantum magnetic fluxes - the composite fermions [87, 101].

Wigner crystals. Several experimental phenomena, including non-linear $I-V$ characteristics [81, 171] and thermopower measurements [19], have linked these insulating phases to a B-induced 2D pinned Wigner crystal.

Recently, a similar reentrant IP was observed in interacting GaAs bilayer hole systems around the QHS at total filling factor $\nu = 1$ [187]. It was suggested in Ref. [187] that this IP signals a bilayer Wigner crystal, stabilized at such high ν by strong Landau level mixing due to higher effective mass of holes, and by the interlayer Coulomb interaction in the bilayer system.

The QHS at $\nu = 1$, flanked by the IP, has also attracted much attention over the past decade. Let's consider a bilayer system made of two 2D systems with the same carrier density and separated by a distance d in the limit of no interlayer tunneling. If d is large, the interlayer Coulomb interaction is negligible and the two layers behave independently. In this case, no QHS is expected at total filling factor $\nu = 1$ since it corresponds to $\nu = \frac{1}{2}$ in each layer[3]. Once the two 2D systems are brought into close proximity, the interlayer Coulomb interaction becomes a prominant parameter leading to the observation of a many-body QHS at total filling factor $\nu = 1$. This many-body state, described as a quantum Hall ferromagnet [108] or as a Bose-Einstein condensate of excitons [57, 138], exhibits many peculiar properties, including Josephson-like tunneling behavior [180], superfluidity in counterflow transport [110, 189] and quantized Hall Coulomb drag [111].

While magnetotransport studies in bilayer systems have intensified in recent years [109], little attention was paid to their thermoelectric properties. Thermopower coefficients are unique tools to study the electronic properties of 2D systems as they are sensitive to the density of states at the Fermi level. In particular, for a 2D insulating system, the diffusion thermopower S_{xx}^d can distinguish between a mobility gap and an energy gap. In the first case, S_{xx}^d should vanish as $S_{xx}^d \propto T^{1/3}$ or be constant at low T, for Mott and Efros-Shklovskii VRH, respectively. In the latter case, when an energy gap E_g separates the ground state from its excitations, S_{xx}^d is expected to diverge at low T as:

$$S_{xx}^d \cong \frac{k_B}{2e}\frac{E_g}{k_B}\, T^{-1}. \tag{6.1}$$

Hence, S_{xx}^d can critically test if the IP results from the strong localization

[3] In the composite fermion description of the fractional QHE, $\nu = \frac{1}{2}$ corresponds to the zero effective magnetic field configuration for composite fermions made of a carrier attached to two quantum magnetic fluxes. The LL filling factor $\nu = \frac{1}{2}$ is shown in Fig. 6.1 for a 2D single-layer hole system. As expected, no QHS is observed at this ν.

of the carriers (mobility gap) or from the formation of a pinned Wigner crystal (energy gap).

We study here the thermopower of interacting GaAs bilayer hole systems around $\nu = 1$. When the hole densities in the two layers are equal, at filling factors near $\nu = 1$, our measurements show that the diffusion thermopower diverges as T^{-1} when the temperature is lowered below ~ 100 mK. This behavior corroborates the magnetotransport [187] and the non-linear $I-V$ results. The T dependence of the thermopower indicates the opening of an energy gap, consistent with the formation of a pinned, bilayer Wigner crystal near the QHS at $\nu = 1$, and allows us to extract an estimation of the Wigner crystal melting temperatures as a function of ν [64].

6.2 Sample description

Two-dimensional bilayer systems can be realized by two distinct means, using double quantum well or wide quantum well structures. First, in wide quantum well structures [127], filling the quantum well with carriers bends the flat potential inside the well. This bent potential acts as a barrier and splits the carrier distribution to two coupled electron layers. In these samples, the splitting of the carrier distribution in two layers increases with the carrier density (see Fig. 6.2(a)). Second, in double quantum well structure, the carriers are simply confined to two narrow quantum wells separated by a barrier (see Fig. 6.2(b)).

Two parameters are of particular interest in bilayer systems at $\nu = 1$. The first is the d/l_B ratio, where d is the distance between the two layers and l_B is the magnetic length at $\nu = 1$. This parameter measures the ratio of the interlayer Coulomb interactions and the intralayer Coulomb interactions. The second is the interlayer tunneling. The magnitude of this tunneling determines energy gap Δ_{SAS} between the two lowest, symmetric and antisymmetric, double quantum well subbands. The subbands' splitting Δ_{SAS} then provides a useful tool to probe the importance of the interlayer tunneling. It is obvious that double quantum well structures provides more controllable bilayer systems since both the strength of the interlayer carrier-carrier interaction, as well as the interlayer tunneling can be determined through the height and the width of the barrier. Note that the many-body QHS at $\nu = 1$ has been shown to develop in bilayers with $d/l_B \lesssim 1.8$ [111, 139] and with extremely small interlayer tunneling [49].

The samples we have studied are Si modulation-doped p-type GaAs double quantum wells grown by molecular beam epitaxy on undoped

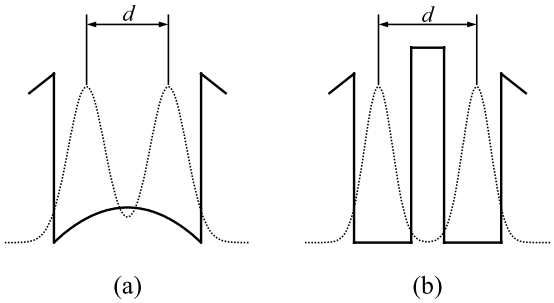

Figure 6.2: Schematic representation of the band structure and carrier distribution in 2D bilayer systems built from (a) wide quantum well and (b) double quantum well structure.

GaAs (311)A wafers. The two samples consist of two 15 nm wide GaAs quantum wells separated by an AlAs barrier with a thickness of 11 nm (sample A) and 7.5 nm (sample B). The growth of the double quantum wells has been performed at Princeton University in the group of Prof. M. Shayegan. A schematic layout of the quantum well structures can be found in Appendix C, where they are referred to as M417 (sample A) and M440 (sample B). The width of the AlAs barrier and the large effective mass of the holes assure a weak interlayer tunneling [4]. Two 8×2 mm^2 rectangular pieces of wafer were cut with their length along the $[01\bar{1}]$ (sample A) and $[\bar{2}33]$ (sample B) crystallographic directions. On both specimens, we patterned 400 μm wide Hall bars in order to reduce density inhomogeneities. Ohmic contacts (alloyed InZn) were made to both layers. A back-gate was used to tune the charge distribution of the two layers. The charge imbalance is denoted by $\Delta p = (p_T - p_B)/2$, where p_B and p_T are the hole densities of the bottom and the top layer, respectively. For balanced charge distributions ($\Delta p = 0$), the total hole density for both samples is close to $p = 5 \times 10^{14}$ m^{-2}.

6.3 Magnetotransport measurements

We first summarize the magnetotransport results for our samples. In Fig. 6.3, we illustrate for sample A the longitudinal resistivity ρ_{xx} as a function of B at low T for a balanced configuration $\Delta p = 0$. Consistent with the sample's extremely small interlayer tunneling, at low B the

[4] A simple band calculation yields a tunneling energy Δ_{SAS} less than 1 μV for the bilayer systems studied here.

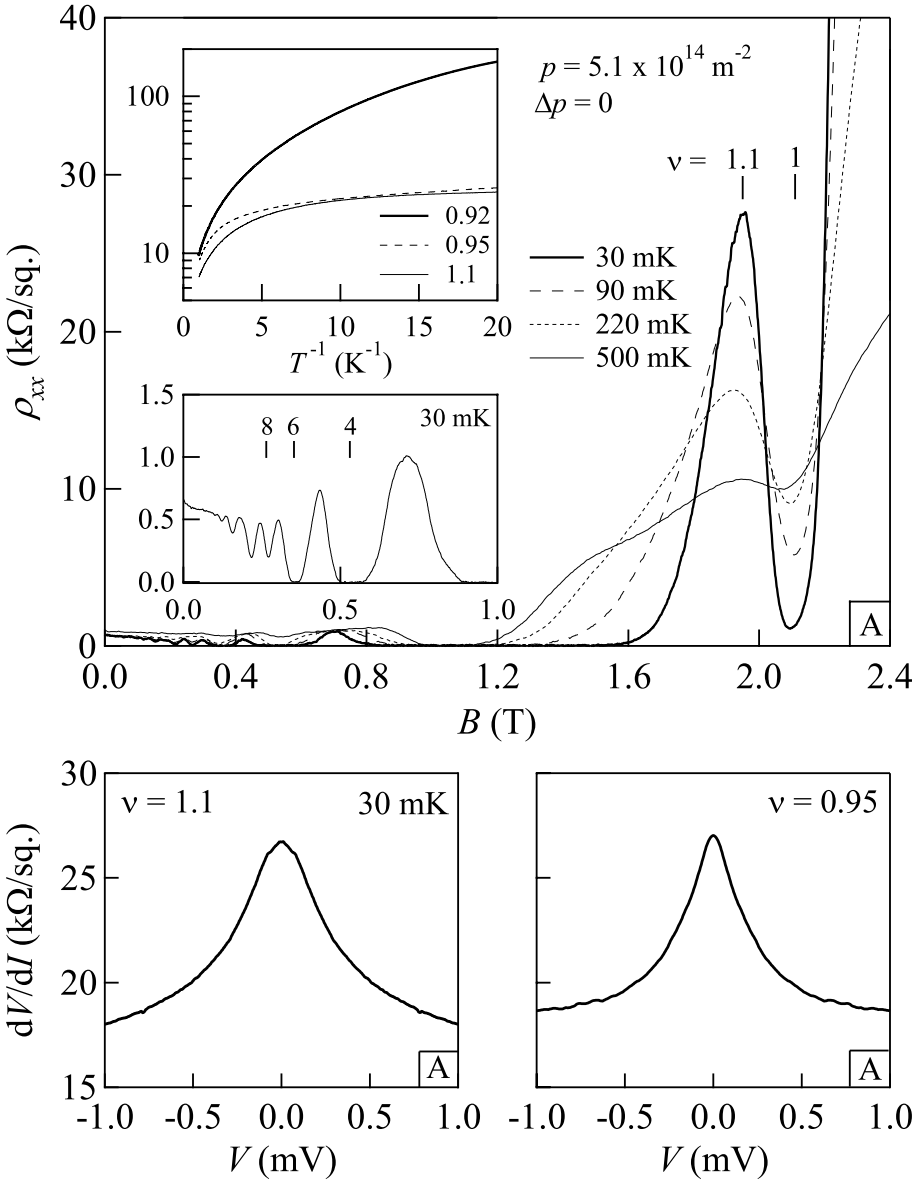

Figure 6.3: Upper panel: longitudinal resistivity ρ_{xx} as a function of B at the indicated temperatures for sample A at a total density $p = 5.1 \times 10^{14}$ m^{-2}. For the data in the figure, the densities of the individual layers are equal ($\Delta p = 0$). Top inset: The T dependence of ρ_{xx} at $\nu = 0.92$, 0.95, and 1.1. Bottom inset: A magnified view of the low-B ρ_{xx} trace at 30 mK. Lower panels: differential resistance in the insulating phase of sample A as a function of the dc bias for $\nu = 1.1$ (left panel) and 0.95 (right panel) at 30 mK.

ρ_{xx} trace exhibits minima only at even integer fillings $\nu = 2$, 4, 6, etc. The strong interlayer interaction, however, leads to a many-body QHS at $\nu = 1$ [109]. Similar magnetotransport data were obtained for sample B. The ratio of intralayer and interlayer energies d/l_B is 1.47 for sample A and 1.29 for sample B, close to value of d/l_B for which the many-body $\nu = 1$ QHS has been previouly observed in GaAs bilayer systems [99, 109, 180, 187]. The measured QHS excitation gaps ${}^1\Delta$, extracted from the T dependence of ρ_{xx} at $\nu = 1$, are 0.13 and 0.67 K, respectively. The larger ${}^1\Delta$ for sample B is consistent with its smaller d/l_B ratio, *i.e.* stronger interlayer Coulomb interaction.

The many-body QHS at $\nu = 1$ is flanked by reentrant IP's [187] as illustrated by the magnetoresistivity traces at various T's. The resistivity strongly increases when $T \to 0$, for B's between ~ 1.8 T ($\nu = 1.17$) and ~ 2 T ($\nu = 1.05$) and for $B \gtrsim 2.2$ T ($\nu = 0.96$). The T-dependence of ρ_{xx} at $\nu = 0.92$, 0.95, and 1.1 is displayed in the top inset to Fig. 6.3 and further reveals the insulating behavior of the resistivity at these fillings. This reentrant insulating phase and termination of the quantum Hall effect is reminiscent of that reported in single-layer systems around $\nu = \frac{1}{5}$ for electrons and $\nu = \frac{1}{3}$ for holes, as well as in the vicinity of $\nu = \frac{1}{2}$ in electron bilayer systems. Both the larger hole effective mass that induces stronger Landau level mixing and the additional Coulomb interaction of a bilayer system have been shown to displace the B-induced Wigner crystal to higher ν's. As suggested in Ref. [187] it is then tempting to attribute the reentrant IP observed in our samples to the formation of a hole bilayer Wigner crystal.

Finally, in the bottom panels of Fig. 6.3 we show $I-V$ characteristics at filling factors near $\nu = 1$ for sample A, exhibiting a strongly non-linear behavior. The differential resistance measurements were performed by applying a current made of a dc and a small ac components to the sample and measuring the ac voltage drop using a lock-in amplifier. The distance between the voltage probes used to measure these $I - V$ characteristics was 1.2 mm. Non-linear $I - V$ traces have been reported in the IP of electron single layer around $\nu = \frac{1}{5}$, where a threshold voltage was needed to generate a decrease of the differential resistance [81]. This electric field threshold was interpreted as a critical value necessary to induce a depinning of the Wigner crystal. While we do not observe any sharp threshold voltage in our data, our non-linear $I - V$ characteristics are very similar to previous measurements reported for the IP near $\nu = \frac{1}{3}$ in single-layer GaAs 2D hole systems [171].

6.4 Magnetothermopower measurements

6.4.1 Thermopower in the insulating phase

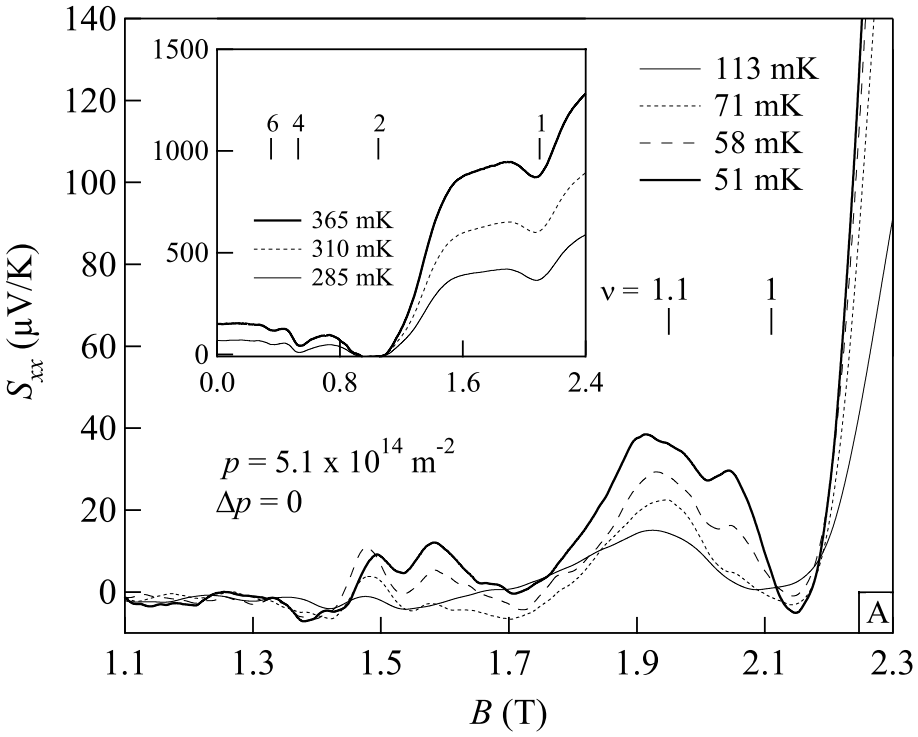

Figure 6.4: S_{xx} as a function of B at four temperatures below 120 mK for sample A. Inset: S_{xx} vs B is displayed at T = 285, 310, and 365 mK in the phonon-drag regime.

We now present the results of our S_{xx} measurements, summarized in Figs. 6.4 and 6.5, and consider first the phonon-drag regime. Figure 6.4 shows S_{xx} vs B traces for sample A at various temperatures. The curves at T = 285, 310, and 365 mK, where the phonon-drag is dominant, are displayed in the Fig. 6.4 inset. Similar to ρ_{xx} data, we observe minima at even filling factors (ν = 2, 4, and 6) and at ν = 1 consistent with a vanishing density of states at the Fermi level [74] and with previous measurements of thermopower in the phonon-drag regime in GaAs bilayer systems [100]. In the phonon-drag regime, a dramatic decrease of S_{xx} is found in the entire investigated B range as T diminishes. This is clearly indicated by the T evolution of S_{xx} at various fillings shown in Fig. 6.5 for both samples.

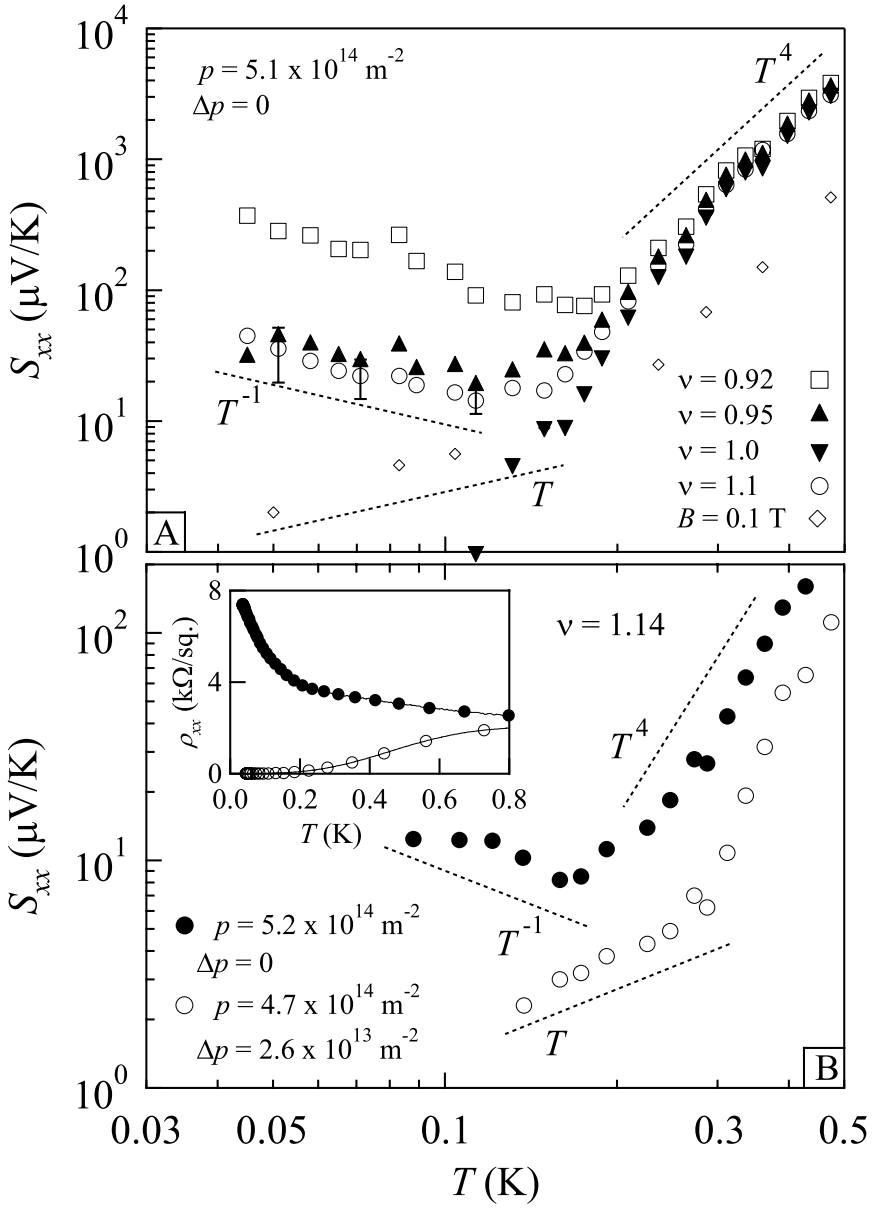

Figure 6.5: Top panel (sample A): T dependence of S_{xx} at different filling factors when the bilayer is balanced. Bottom panel (sample B): T dependence of S_{xx} at $\nu = 1.14$ for balanced (•) and imbalanced (○) charge distributions. Inset: ρ_{xx} vs T at $\nu = 1.14$ for the balanced and the imbalanced configurations. The dotted lines indicate various T dependencies. The error bars are given by the noise of the lock-in amplifier, the magnitude of the applied thermal gradient, and the accuracy of the thermometers' calibration.

In the top panel of Fig. 6.5, S_{xx} vs T is displayed for sample A at $\nu =$ 1.1, 1, 0.95, 0.92 and for $B = 0.1$ T when the bilayer system is balanced. In the bottom panel of the figure, we show S_{xx} vs T for sample B. Data points are presented at $\nu = 1.14$ for a balanced and a slightly imbalanced charge distribution. At high T, $S_{xx} \cong S^g_{xx}$ follows the well known T^4 law [124] for all the experimental configurations shown in Fig. 6.5 [5].

At low temperatures, where the thermopower is dominated by the diffusion contribution, S_{xx} increases with decreasing T in the IP's reentrant around $\nu = 1$. The main result of this chapter is illustrated in Fig. 6.4 by the S_{xx} vs B traces at $T = 113$, 71, 58, and 51 mK [6]. The divergence of S_{xx} at low T in the IP is further illustrated in Fig. 6.5. Focusing on the data shown in the top panel of Fig. 6.5, we observe that at $\nu = 1$, S_{xx} rapidly approaches zero as expected for a QHS with no entropy [36] and S_{xx} at $B = 0.1$ T is proportional to T below 200 mK as expected for a diffusion-dominated thermopower in a metallic system. However, at $\nu = 1.1$, 0.95, and 0.92, $S_{xx} \propto T^{-1}$ as $T \to 0$. This divergence of S_{xx} in the reentrant IP's at very low T is very similar to that observed in the reentrant IP around $\nu = \frac{1}{3}$ in 2D single-layer hole systems [19]. It indicates the opening of an energy gap and suggests the formation of a pinned bilayer Wigner crystal near $\nu = 1$.

Sample B exhibits qualitatively the same behavior. In the lower panel of Fig. 6.5 we show S_{xx} vs T data for sample B at $\nu = 1.14$ where magnetotransport reveals an IP. The S_{xx} data show a divergence at low T when the bilayer system is balanced (closed circles, $\Delta p = 0$). In the same panel we also show data (open circles, $\Delta p = 2.6 \times 10^9$ cm^{-2}) for sample B when charge distribution is imbalanced, *i.e.*, when charge is removed from the the bottom layer via the application of positive backgate bias. For the imbalanced state, S_{xx} at $\nu = 1.14$ turns from a T^{-1} to an approximately linear temperature dependence. This observation is in agreement with magnetotransport results showing that the insulating behaviour for $\nu > 1$ disappears for small charge imbalance between the two layers [187]. The disappearance of the IP for $\nu > 1$ is illustrated in the inset of Fig. 6.5, where the longitudinal resistivity at $\nu = 1.14$ is plotted as a function of T for both balanced and imbalanced config-

[5] We note that S^g_{xx}, for $T > 200$ mK, is one order of magnitude larger in sample A than in sample B. The difference likely results from different values of Λ, which depends on the specimens' macroscopic properties such as thickness and surface roughness [18, 74].

[6] In the field range $1.3 < B < 1.7$ T, we observe a weak (non-zero), oscillating S_{xx} signal. We do not know the origin of these features. We speculate that they may be signaling the presence of fractional QHS's (e.g. at $\nu = \frac{4}{3}$), and a competition between such states and the engulfing IP. Note that, interestingly, ρ_{xx} in this field range is rather featureless and shows a deep minimum ($\rho_{xx} > 0$).

urations. However, the imbalanced configuration measurement has to be considered carefully as the two layers are not probed equally [199]. For a better understanding of the thermopower properties of imbalanced bilayer systems, experiments with independent contacts to each layer would be more appropriate.

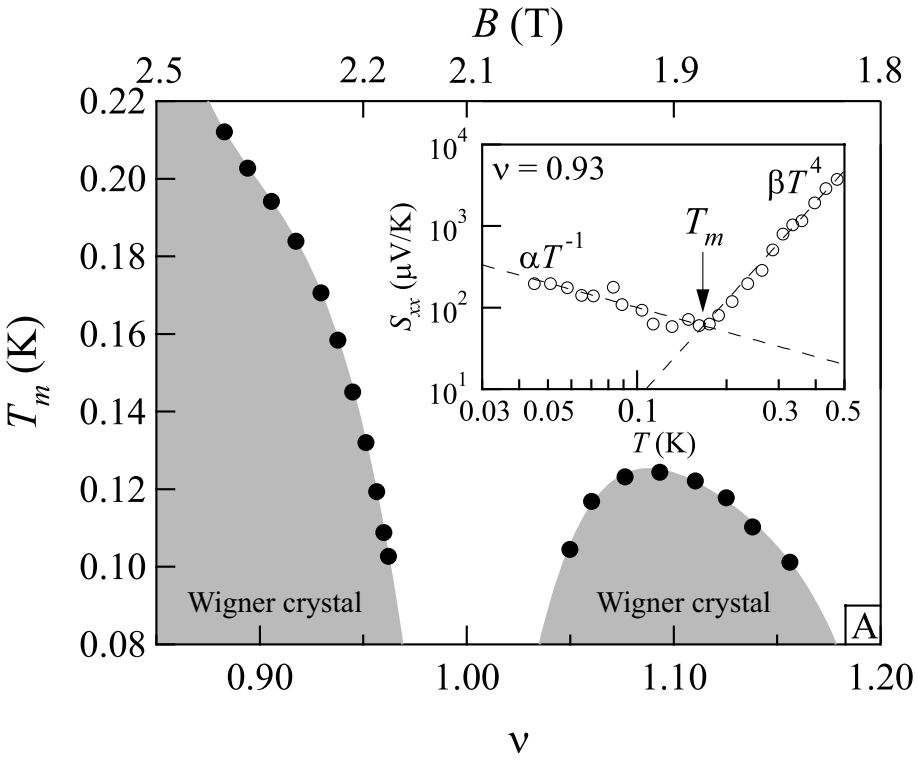

Figure 6.6: Evolution of the melting temperature T_m as a function of ν of the pinned, bilayer Wigner crystal in sample A. The top axis shows the corresponding magnetic fields. Inset: T_m is extracted from the T dependence of S_{xx} by assuming that the rise in S_{xx} signals the melting of the Wigner crystal.

We now turn to a more quantitative discussion of our thermopower data. From the T-dependence of S_{xx}, shown in Fig. 6.5 and the inset to Fig. 6.6, we can extract an estimation of the Wigner crystal melting temperatures as a function of ν using a phenomenological approach. To estimate the melting temperature T_m, we assume that the solid-to-liquid transition occurs when S_{xx} starts to rise as T is lowered. As illustrated in the inset to Fig. 6.6 for $\nu = 0.93$, we have fitted at fixed filling factors the phonon-drag thermopower with a T^4 law for $T \gtrsim 200$ mK and the

diffusion thermopower with a T^{-1} law for $T \lesssim 100$ mK. The intersection of these two fits determines $T_m(\nu)$. In Fig. 6.6, T_m vs ν is shown for sample A. The reentrant behavior of the IP is illustrated by the evolution of T_m; T_m is finite in a small filling range centered near $\nu = 1.1$ and at $\nu \gtrsim 0.95$, but is vanishingly small near $\nu = 1$ ($B = 2.1$ T) where the quantum Hall ground state is present. The magnitude of the estimated T_m in our sample is similar to the reported values of the Wigner crystal melting temperature in single-layer 2D hole [19] and electron [81, 146] systems around $\nu = \frac{1}{3}$ and $\frac{1}{5}$, respectively. Using Eq. (6.1) and the $S_{xx} = \alpha T^{-1}$ fit to the diffusion regime, an estimate of the energy gap associated with the pinned Wigner crystal can be made when $E_g \gg k_{\rm B}T$ [19]. This energy gap likely corresponds to the creation energy of thermally activated defects (such as bound pairs of dislocations), which may be responsible for electrical conduction in the pinned Wigner crystal [60]. For example, at $\nu = 0.92$, $E_g/k_{\rm B} = 0.34$ K in sample A. This value is of the same order of magnitude as the activation energy $E_A/k_{\rm B} = 0.15$ K determined from fitting ρ_{xx} in the low-T range to $\ln(\rho_{xx}) \propto E_A/2k_{\rm B}T$, and compares well with the Wigner crystal melting temperature $T_m = 0.18$ K at this filling.

6.4.2 Thermopower at $\nu = 1$

We finally focus on the T-dependence of S_{xx} at $\nu = 1$ presented in Fig. 6.7 for samples A and B. Interestingly, the phonon-drag thermopower deviates from the usual T^4 dependence below ~ 300 mK for sample A and below ~ 400 mK for sample B. The phonon-drag thermopower then vanishes around $T \approx 300$ mK for sample B, while for sample A, S_{xx} is non-zero down to $T \approx 100$ mK. These results corroborate the magnetotransport data. Indeed, as deduced from the resistivity measurements, sample B has a stronger many-body QHS at $\nu = 1$, in agreement with its smaller d/l_B ratio. No sign of diffusion thermopower is observed in the entire investigated T-range as expected for a QHS with no entropy [36].

6.5 Conclusion

In this chapter we investigate interacting 2D GaAs bilayer hole system in the limit of weak interlayer tunneling. Magnetotransport data show that these systems exhibit a many-body QHS at total filling factor $\nu = 1$. When the bilayer is balanced, this peculiar QHS is flanked by a reentrant IP. It has been suggested that this IP could result from the formation of a pinned bilayer Wigner crystal, stabilized at such high ν's

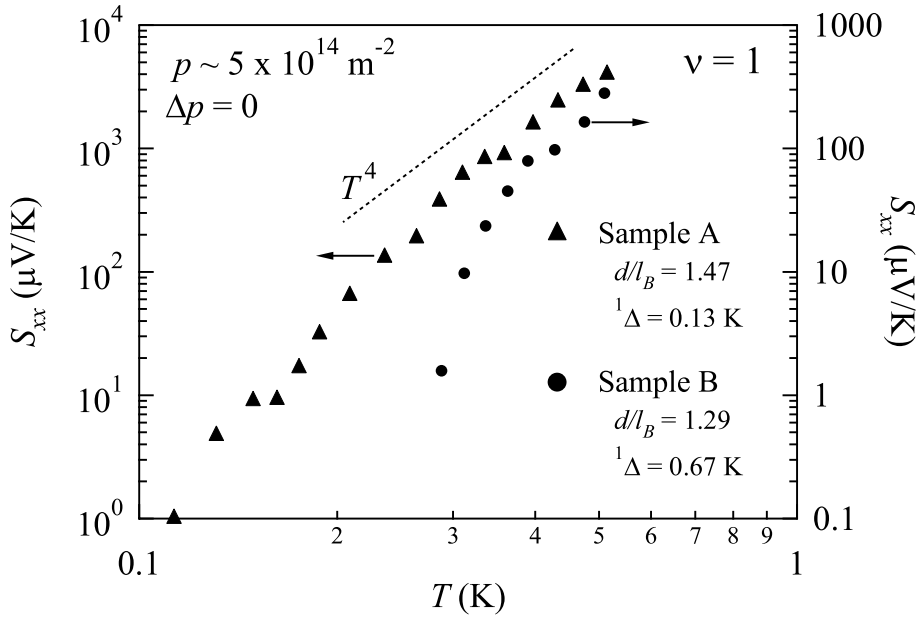

Figure 6.7: T-dependence of S_{xx} at $\nu = 1$ for samples A and B. The hole density is 5.1×10^{14} m^{-2} for sample A and 5.2×10^{14} m^{-2} for sample B.

by strong LLs mixing due to the large effective mass of holes and by the additional interlayer Coulomb interaction of the bilayer system.

We report thermopower measurements in the reentrant IP around the QHS at $\nu = 1$. The diffusion thermopower is a very useful tool to study such IP as it can distinguish between a mobility gap (strong localization) and an energy gap (Wigner crystal). Indeed, when $T \to 0$, S_{xx}^{d} is expected to vanish or be constant for the former, while it should diverge for the latter. For $T \gtrsim 200$ mK, in the phonon-drag regime, our results show that S_{xx} decreases as T^4 in the entire investigated B-range. This behavior of the phonon-drag thermopower is similar to that predicted and observed in GaAs single-layer systems. At very low T, when the diffusion thermopower dominates, S_{xx} diverges as T^{-1} in the IP's reentrant around $\nu = 1$. This behavior clearly indicates the opening of an energy gap and suggests the presence of a pinned hole bilayer Wigner crystal. Interpreting our thermopower data in terms of a Wigner crystal melting, we have extracted an estimation of T_m vs ν.

Conclusions and perspectives

> Dans les sciences, le chemin est plus important que le but. Les sciences n'ont pas de fin.
>
> *Erwin Chargaff*

The main scientific outcomes of this thesis are various findings in two-dimensional (2D) GaAs holes systems, including open quantum dots (QDs), the parallel magnetic field ($B_{\parallel}$) induced metal-insulator transition (MIT) and the reentrant insulating phase (IP) around Landau level filling factor $\nu = 1$ in bilayer systems. The study of open hole QDs was the first purpose of this thesis. The diversity of the subjects approached here originates from the initial difficulties encountered to realize exploitable GaAs open hole QDs. Indeed, numerous attempts to study holes QDs led to devices with an extremely noisy conductivity, making the observation of coherent transport impossible. Ironically, it is after we started the thermopower studies of 2D insulating systems, and at the moment when our initial goal was almost abandonned that we succeed in fabricating measurable open hole QDs. Obviously, this highly *non-linear* history has led to the somewhat disparate manuscript presented here. The most significant results of this work can therefore be separated in three distinct parts.

Here we report for the first time the fabrication as well as low temperature T magnetotranport measurements of open hole QDs. Beyond the development of an adapted fabrication process, it was brought to light that the heterostructure used as substrate for the QDs' realization plays a major role for the production of devices exempt of noise. The quantum well structure used to fabricate the QDs presented in Chapter 3 is, at the moment, the only structure that provided quiet devices. Nevertheless, the application of a top gate voltage still introduced noise in the transport data. The understanding of the parameters that generates the noise in the low-T conductivity of open QDs is then particularly important for future realization of more flexible QD devices using the top

gate technique. In particular, as the presence of switching impurities in the doped layer is a possible source of noise, the fabrication of QDs using the combination of shallow etching and top gates should be investigated.

The magnetotransport traces measured on our hole quantum dots revealed signatures of coherent transport, namely magnetoconductance fluctuations (MCFs) and weak anti-localization (WAL), below 500 mK. We used arrays of QDs to average out the MCFs and access the WAL correction to the conductivity. These coherent effects were analyzed using an extended random matrix theory (RMT) that includes spin-orbit interaction. We extracted a T-dependence for the dephasing time τ_ϕ together with an upper limit for spin-orbit scattering time τ_{so}. The deduced τ_ϕ exhibits a T-dependence that lies between T^{-1} and T^{-2}. While this T-dependence resembles that measured in similar electron QDs, the value of τ_ϕ is found to be one order of magnitude smaller for holes than for electrons. On the other hand, the value of τ_ϕ extracted from our samples is consistent with that reported for various p-type 2D systems, indicating that the small value of τ_ϕ observed here is likely related to scattering mechanisms in the 2D hole system.

The analysis of the WAL peak in the QDs' magnetoconductivity provides the upper limit for τ_{so} and tells us that our open QDs are in the strong spin-orbit interaction regime. The original interest for open hole QDs was the production of devices with controlable spin-orbit coupling, that are potentially attractive for the field of spintronics. Indeed, 2D GaAs holes are subject to stronger spin-orbit interaction than 2D GaAs electron systems where it can generally be neglected. Moreover, the structure inversion asymmetry contribution to the total spin-orbit interaction can be significantly tuned through a modification of the quantum well symmetry by means of top and back gates. However, from the analysis of the WAL peak, we determined that $\tau_{so} \lesssim 10^{-11}$ s, independent of the shape of the vertical confining potential. This indicates that the bulk inversion asymmetry (BIA) contribution to the spin-orbit interaction is large enough to induce a strong spin-orbit regime in our micrometer-sized QDs. The production of p-type GaAs-based systems with controlable spin-orbit interaction through a modification of the vertical confining potential can, therefore, only be performed by decreasing the devices' size or by reducing the BIA contribution to the spin-orbit interaction. The reduction of the BIA contribution could possibly be performed by changing the total hole sheet density.

Our work also highlights the lack of adapted theory for both the analysis of the magnetotransport measurements in open hole QDs and the prediction of the hole dephasing time's in 2D systems or in QDs. The analysis was performed here using theories developed for electron

systems that do not account for the complex band structure of GaAs holes. In particular, the extended RMT does not take the spin-orbit induced zero magnetic field spin-splitting into account. In electron QDs, the Zeeman-induced spin splitting has been shown to reduce the MCFs' variance by a factor of 2. Further investigations on our holes QDs with an additional parallel magnetic field or at tilted angles could tell us if the spin-orbit-induced spin-splitting has a similar effect on the MCFs' variance.

The second part of this work focused on the $B_{\|}$-induced MIT in dilute 2D hole systems. Since the early 90s, the observation of a striking metallic T-dependence of the conductivity in dilute 2D systems, as well as transitions to insulating behavior at lower carrier densities or in a $B_{\|}$ have generated a lot of controversy. Several ground states have been proposed to explain the experimental behavior of the conductivity. Here, we have studied the longitudinal thermopower S across the $B_{\|}$-induced MIT in a dilute (311)A 2D hole heterojunction. At low-$B_{\|}$, in the metallic regime, the low-T thermopower, dominated by the diffusion contribution, behaves as expected for a degenerate hole gas and decreases linearly with T. However, the diffusion thermopower S^d changes dramatically around the MIT. Along the high mobility direction S drops to zero, while for the low mobility direction it changes sign.

A similar sign reversal of the diffusion thermopower was previously observed in a 2D (311)A GaAs quantum well in the vicinity of the p-induced MIT. This effect has been adressed theoretically within the screening theory and was attributed to interface roughness scaterring. Similar arguments can be invoked to explain the behavior of S in our samples. The in-plane magnetic field can modify the scattering through two different mechanisms. First, it pulls the hole's wave function closer to the interface, thereby making roughness scattering more efficient. Second, $B_{\|}$ depopulates the minority spin subband and, as a result, suppresses intersubband scattering. The origin of the sign reversal of S as stemming from an increased strength of interface roughness scattering is consistent with the weaker effect observed along the high mobility direction. The remarkable behavior of S^d then seems to indicate that the apparent $B_{\|}$-induced MIT does not originate from a modification of the system's ground state but is rather accompanied by a dramatic change in interface roughness and intersubband scattering mechanisms. These conclusions are strengthened by the results obtained in the phonon-drag regime which do not exhibit any change of S across the MIT.

While our results are in agreement with the screening theory, they cannot definitively refute that carrier-carrier interaction plays a role. Nevertheless, our work provides thermopower measurements that could

be used, beyond the usual conductivity data, to critically test the different proposed theories. Experimentally, the interpretation given here could be further tested by performing similar measurements in comparable systems with smoother GaAs/AlGaAs interfaces like C-doped (100) 2D hole systems or (100) 2D electron systems. Also, thermopower measurements in the p-induced MIT could provide valuable informations on both the insulating and metallic regimes.

Finally, the third part of this work deals with the IP observed in bilayer hole systems around the many body quantum Hall state (QHS) at $\nu = 1$. Bilayer systems, where two 2D carrier gases are brought into close proximity, have been shown to exhibit a rich physics arising from the new, layer degree of freedom. In interacting bilayer systems with weak interlayer tunneling, a peculiar many-body QHS is observed at $\nu = 1$. In GaAs bilayer hole systems, the $\nu = 1$ QHS is flanked by a reentrant IP. It has been suggested that this IP could signal the formation of a pinned bilayer Wigner crystal, stabilized at such high ν's by strong LLs mixing due to the large effective mass of holes and by the additional interlayer Coulomb interaction of the bilayer system.

We report thermopower measurements in the reentrant IP observed in GaAs bilayer hole systems around the QHS at $\nu = 1$. At very low T, when the diffusion thermopower dominates, S_{xx} diverges as T^{-1} in the IP's reentrant around $\nu = 1$. This behavior clearly indicates the opening of an energy gap and suggests the presence of a pinned hole bilayer Wigner crystal. From the thermopower data, we extracted an estimation of the Wigner crystal melting temperatures as a function of ν using a phenomenological approach.

Further thermopower investigations on bilayer systems with separate contacts to each layer would also be of great interest. Ideed, this particular configuration would allow the measurement of the thermopower in each layer independently. While for balanced systems, it should provide similar results as those described in Chapter 6, it would further allow to unambiguously study the evolution of the reentrant IP as well as of the $\nu = 1$ QHS as a function the density imbalance Δp.

Appendix A

The extended RMT conductance correlator

Within the extended random matrix theory (RMT) that includes the Zeeman splitting and the spin-orbit interaction [7, 32, 43], the conductance correlator $cov(E, E')$ writes as

$$cov(E, E') = \left(\frac{e^2}{h}\right)^2 \left(\frac{N_1 N_2}{N_1 + N_2}\right)^2 (V_C + V_D), \tag{A.1}$$

where

$$V_D = \frac{\Xi_D}{\Upsilon_D}, \tag{A.2}$$

$$V_C = \frac{\Xi_C}{\Upsilon_C}. \tag{A.3}$$

Here we abbreviated

$$\begin{aligned}
\Xi_D = 2\left|K_D(4a^4 - L_D^2) + 4a^2 bb' - L_D(b^2 + b'^2)\right|^2 \\
+ 2\left|K_D(b^2 + b'^2) + K_D^2 L_D - 4a_\perp^2 L_D (x - x')^2\right|^2 \\
+ 8a_\perp^2 (x - x')^2 \left[\left(b + b'\right)^2 + \left|L_D + 2a^2\right|^2\right] \\
\left[\left(b - b'\right)^2 + \left|L_D - 2a^2\right|^2\right] \\
+ 8\left|K_D bb' + a^2\left[K_D^2 - 4a_\perp^2 (x - x')^2\right]\right|^2 \\
+ 4\left|b(b^2 - b'^2) - K_D(2a^2 b' - bL_D)\right|^2 \\
+ 4\left|b'(b'^2 - b^2) - K_D(2a^2 b - b' L_D)\right|^2 \\
+ 8\left|a^2(b^2 + b'^2) - bb' L_D\right|^2 \ ,
\end{aligned} \tag{A.4}$$

$$
\begin{aligned}
\Xi_C = 2\left|K_C(4a^4 - L_C^2) - 4a^2bb' - L_C(b^2 + b'^2)\right|^2 \\
+ 2\left|K_C(b^2 + b'^2) + K_C^2 L_C - 4a_\perp^2 L_C(x + x')^2\right|^2 \\
+ 8a_\perp^2(x + x')^2\left[\left(b - b'\right)^2 + \left|L_C + 2a^2\right|^2\right] \\
\left[\left(b + b'\right)^2 + \left|L_C - 2a^2\right|^2\right] \\
+ 8\left|K_C bb' + a^2\left[-K_C^2 + 4a_\perp^2(x + x')^2\right]\right|^2 \\
+ 4\left|b(b^2 - b'^2) + K_C(2a^2 b' + bL_C)\right|^2 \\
+ 4\left|b'(b'^2 - b^2) + K_C(2a^2 b + b'L_C)\right|^2 \\
+ 8\left|a^2(b^2 + b'^2) + bb'L_C\right|^2 \ ,
\end{aligned}
\tag{A.5}
$$

$$
\begin{aligned}
\Upsilon_D = \left|(b^2 - b'^2)^2 + 2K_D(-4a^2bb' + (b^2 + b'^2)L_D)\right. \\
\left. +(L_D^2 - 4a^4)(K_D^2 - 4a_\perp^2(x - x')^2)\right|^2 \ ,
\end{aligned}
\tag{A.6}
$$

$$
\begin{aligned}
\Upsilon_C = \left|(b^2 - b'^2)^2 + 2K_C(4a^2bb' + (b^2 + b'^2)L_C)\right. \\
\left. +(L_C^2 - 4a^4)(K_C^2 - 4a_\perp^2(x + x')^2)\right|^2 \ ,
\end{aligned}
\tag{A.7}
$$

and

$$
\begin{aligned}
K_D &= N + \frac{2\pi i(\varepsilon - \varepsilon')}{\Delta} + \frac{1}{2}\left(x - x'\right)^2 + 2\left(a^2 + a_\perp^2\right) + \frac{1}{2}\left(b_\perp + b'_\perp\right)^2, \\
L_D &= N + \frac{2\pi i(\varepsilon - \varepsilon')}{\Delta} + \frac{1}{2}\left(x - x'\right)^2 + 2a^2 + \frac{1}{2}\left(b_\perp - b'_\perp\right)^2, \\
K_C &= N + \frac{2\pi i(\varepsilon - \varepsilon')}{\Delta} + \frac{1}{2}\left(x + x'\right)^2 + 2\left(a^2 + a_\perp^2\right) + \frac{1}{2}\left(b_\perp - b'_\perp\right)^2, \\
L_C &= N + \frac{2\pi i(\varepsilon - \varepsilon')}{\Delta} + \frac{1}{2}\left(x + x'\right)^2 + 2a^2 + \frac{1}{2}\left(b_\perp + b'_\perp\right)^2.
\end{aligned}
$$

The dimensionless parameters x^2, a^2, $a_\perp^2$, b, $b_\perp^2$ correspond to the energy scales ε_B, $\varepsilon_\perp^{\rm so}$, $\varepsilon_\parallel^{\rm so}$, $\varepsilon^{\rm Z}$, $\varepsilon_\perp^{\rm Z}$ rescaled with respect to the mean level spacing Δ, and are given by

$$
\begin{aligned}
x^2 &= \pi\varepsilon_B/\Delta, \\
a_\perp^2 &= \pi\varepsilon_\perp^{\rm SO}/\Delta, \\
a^2 &= \pi\varepsilon_\parallel^{\rm SO}/\Delta, \\
b &= \pi\varepsilon^{\rm Z}/\Delta, \\
b_\perp^2 &= \pi\varepsilon_\perp^{\rm Z}/\Delta,
\end{aligned}
\tag{A.8}
$$

where the characteristic energy scales of the systems write as

$$\begin{aligned}
\varepsilon_B &= \kappa E_{\mathrm{Th}} \left(eB_3 L^2/2\hbar\right)^2, \\
\varepsilon_{\perp}^{\mathrm{so}} &= \kappa E_{\mathrm{Th}} \left(L^2/4\lambda^2\right)^2, \\
\varepsilon_{\parallel}^{\mathrm{so}} &= \kappa' \left(L^2/4\lambda^2\right) \varepsilon_{\perp}^{\mathrm{so}}, \\
\varepsilon^{\mathrm{Z}} &= \mu_B g B, \\
\varepsilon_{\perp}^{\mathrm{Z}} &= \frac{\kappa''(\varepsilon^{\mathrm{Z}})^2}{E_{\mathrm{Th}}} \left(L^2/4\lambda^2\right).
\end{aligned} \tag{A.9}$$

Here, $E_{\mathrm{Th}} = \hbar v_F l_m/2L^2$ is the Thouless energy, with v_F the Fermi velocity, l_m the mean free path and L the size of the QD, $\lambda^2 = \lambda_1\lambda_2$, and κ, κ', and κ'' are coefficients of order unity. The two length scales λ_1 and λ_2 are associated with spin-orbit coupling along the two directions in the plane of the quantum dot. The coefficients κ' and κ'' depend on the sample geometry and on the ratio λ_1/λ_2 of the spin-orbit lengths. The coefficient κ'' also depends on the direction of the magnetic field. The coefficient κ depends on the sample geometry only.

Finaly, note that the corresponding quantities x', b', $b'_{\perp}$ are defined when calculating the parameters at a different value of the magnetic field B'.

Appendix B

Process sheet

The Table presented here below provides the detailed process sheet we used to fabricate our hole open QDs from GaAs heterostructures. The etching times given here are those used for the M439 wafer (see Appendix C).

Step description	Products	Parameters
Sample cutting	GaAs/AlGaAs heterostructure	size: 3×3 mm
Standard cleaning	- trichloroethylene - acetone - methanol - dried with N_2	5 min boiling 5 min ultrasonic bath 5 min boiling 5 min ultrasonic bath 5 min
Sample sticking	onto a 2 inch Si wafer using carbon paint	10 min on a hot plate at 100°C
Resist spin coating	6% PMMA 950K in chlorobenzene	5000 rpm 6000 rpm/s 1 min
Resist backing		10 min on a hot plate at 160°C
E-beam lithography		magnification: ×400 dose: 250 μC/cm^2 $I_{beam} \sim 670$ pA
Development	- MIBK/iso (1/3) - isopropanol - DI H_2O - dried with N_2	1min 30 sec 30 sec 5 min

Metallization	13 nm Ni 30 nm Be 100 nm Au 15 nm Ni 50 nm Au	deposition rate: $\sim$ 0.1 nm/s
Lift-off	acetone	ultrasonic bath or bath heating can be used
Standard cleaning	- trichloroethylene - acetone - methanol - dried with N_2	5 min boiling 5 min ultrasonic bath 5 min boiling 5 min ultrasonic bath 5 min
Rapid thermal annealing	atmosphere: 95% N_2 / 5% H_2	1 min at 450°C
Standard cleaning	- trichloroethylene - acetone - methanol - dried with N_2	5 min boiling 5 min ultrasonic bath 5 min boiling 5 min ultrasonic bath 5 min
Sample sticking	onto a 2 inch Si wafer using carbon paint	10 min on a hot plate at 100°C
Oxyde removal	- $H_2SO_4/H_2O(1/240)$ - DI H_2O - dried with N_2	15 sec 5 min
Sample degazing		overnight under vacuum in an oven at 140°C
Resist spin coating	6% PMMA 950K in chlorobenzene	5000 rpm 6000 rpm/s 1 min
Resist backing		10 min on a hot plate at 160°C
E-beam lithography		magnification: $\times$400 dose: 250 μC/cm^2 $I_{beam} \sim$ 670 pA

Development	- MIBK/iso (1/3) - isopropanol - DI H_2O - dried with N_2	1min 30 sec 30 sec 5 min
Wet etching	- $H_3PO_4/H_2O_2/H_2O$ (1/1/25) - DI H_2O - dried with N_2	1 min 30 sec 5 min
Standard cleaning	- trichloroethylene - acetone - methanol - dried with N_2	5 min boiling 5 min ultrasonic bath 5 min boiling 5 min ultrasonic bath 5 min
Sample sticking	onto a 2 inch Si wafer using carbon paint	10 min on a hot plate at 100°C
Oxyde removal	- H_2SO_4/H_2O(1/240) - DI H_2O - dried with N_2	15 sec 5 min
Sample degazing		overnight under vacuum in an oven at 140°C
Resist spin coating	3% PMMA 950K in chlorobenzene	6000 rpm 6000 rpm/s 1 min
Resist backing		10 min on a hot plate at 160°C overnight in a oven at 140°C
E-beam lithography		magnification: ×2000 dose: 190 $\mu C/cm^2$ $I_{beam} \sim 25$ pA
Development	- MIBK/iso (1/3) - isopropanol - DI H_2O - dried with N_2	1min 30 sec 30 sec 5 min
Wet etching	- $H_3PO_4/H_2O_2/H_2O$ (1/1/25) - DI H_2O - dried with N_2	45 sec 5 min

Standard cleaning	- trichloroethylene - acetone - methanol - dried with N_2	5 min boiling 5 min ultrasonic bath 5 min boiling 5 min ultrasonic bath 5 min
Sample sticking	onto a 2 inch Si wafer using carbon paint	10 min on a hot plate at 100°C
Resist spin coating	6% PMMA 950K in chlorobenzene	5000 rpm 6000 rpm/s 1 min
Resist backing		10 min on a hot plate at 160°C
E-beam lithography		magnification: ×400 dose: 250 μC/cm^2 $I_{beam} \sim 670$ pA
Development	- MIBK/iso (1/3) - isopropanol - DI H_2O - dried with N_2	1min 30 sec 30 sec 5 min
Metallization	10 nm Ti 50 nm Pt	deposition rate: ~ 0.1 nm/s
Lift-off	acetone	ultrasonic bath or bath heating can be used
Standard cleaning	- trichloroethylene - acetone - methanol - dried with N_2	5 min boiling 5 min ultrasonic bath 5 min boiling 5 min ultrasonic bath 5 min

Table B.1: Process sheet for the fabrication of hole open QDs from 2D GaAs heterostructures.

Appendix C

Heterostructures layout

In this Appendix, schematic representations of the growth sequences of the heterostrutures used in this work are presented. All the heterostructures used in this thesis are high-mobility p-type GaAs 2D systems fabricated by MBE on (311)A GaAs wafers.

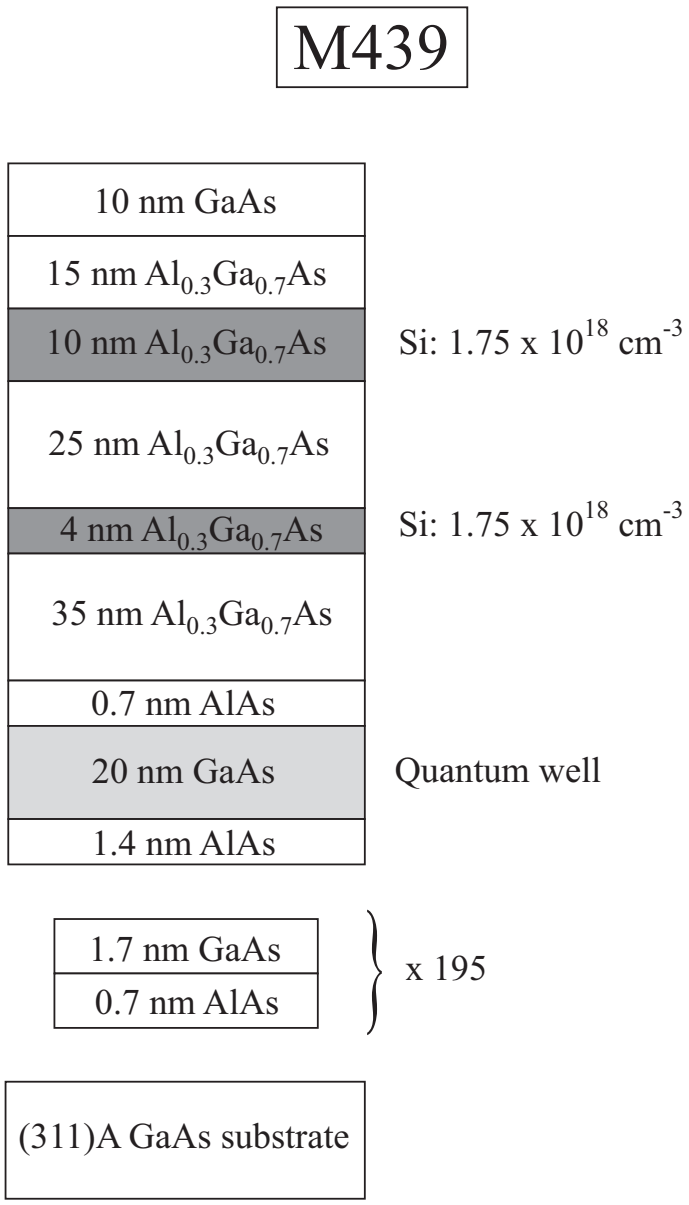

Figure C.1: M439 - growth structure. This quantum well was used for the fabrication of the open hole QDs presented in Chapter 3.

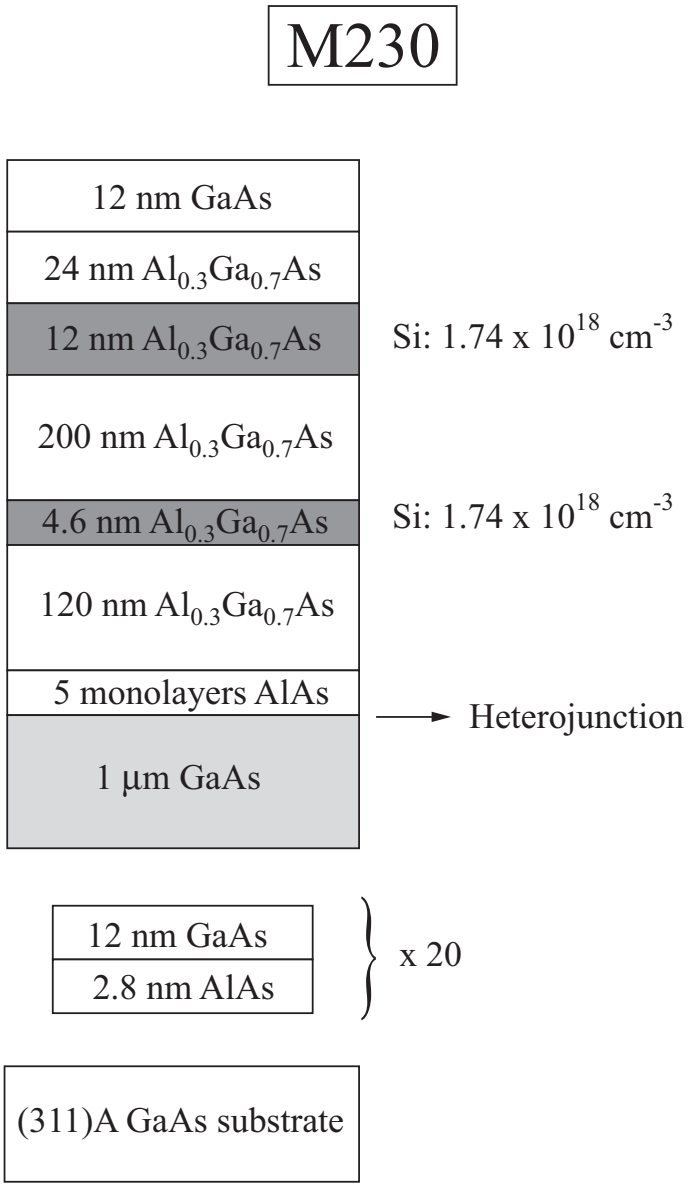

Figure C.2: M230 - growth structure. This heterojunction was used to study the $B_{\|}$-induced MIT through thermopower measurements (see Chapter 4).

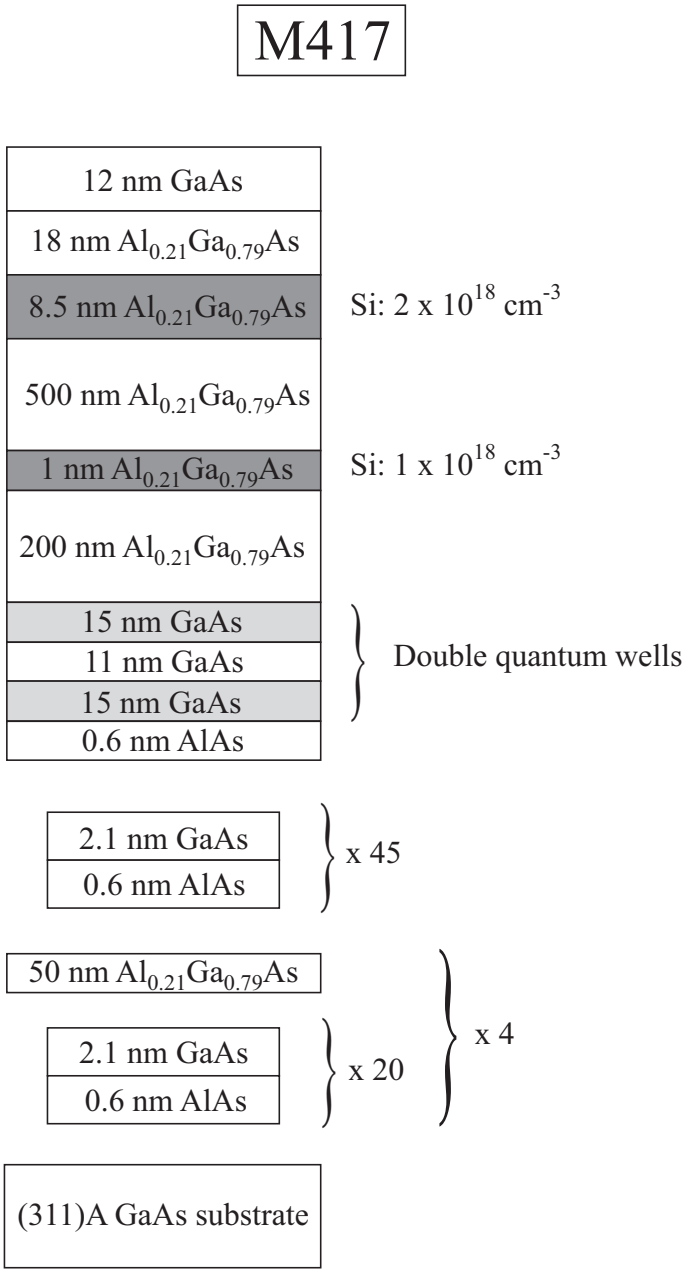

Figure C.3: M417 - growth structure. This double quantum well (sample A) was used to investigate the thermopower in the reentrant insulating phase observed around $\nu = 1$ in 2D bilayer hole systems (see Chapter 6).

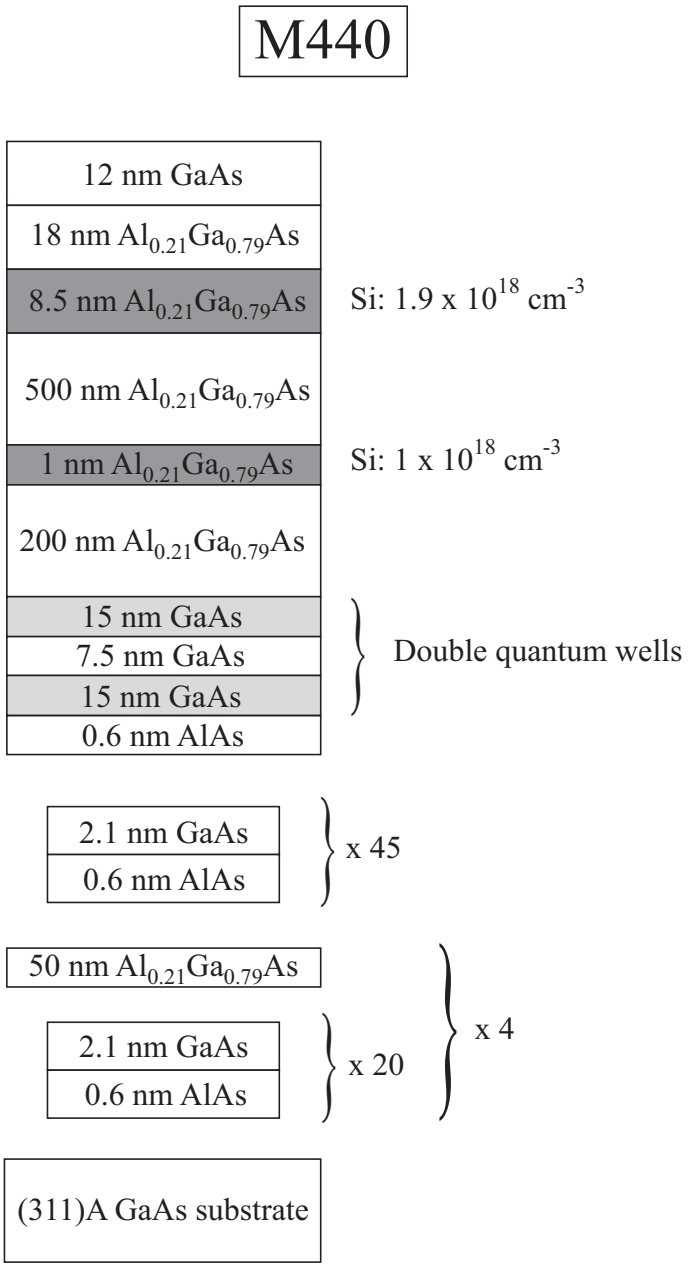

Figure C.4: M440 - growth structure. This double quantum well (sample B) was used to investigate the thermopower in the reentrant insulating phase observed around $\nu = 1$ in 2D bilayer hole systems (see Chapter 6).

Bibliography

[1] E. Abrahams, P. Anderson, D. Licciardello and T. Ramakrishnan, *Scaling Theory of Localization: Absence of Quantum Diffusion in Two Dimensions*. Phys. Rev. Lett. **42**, 673 (1979).

[2] E. Abrahams, S. Kravchenko and M. Sarachik, *Colloquium: Metallic behavior and related phenomena in two dimensions*. Rev. Mod. Phys. **73**, 251 (2001).

[3] S. Adachi, *GaAs, AlAs, $Al_xGa_{1-x}As$: Materials parameters for use in research and device applications*. J. Appl. Phys. **58**, R1 (1985).

[4] Y. Aharonov and D. Bohm, *Significance of Electromagnetic Potentials in the Quantum Theory*. Phys. Rev. **115**, 485 (1959).

[5] R. Akis, D. Ferry and J. Bird, *Magnetotransport fluctuations in regular semiconductor ballistic quantum dots*. Phys. Rev. B **54**, 17705 (1996).

[6] R. Akis, D. Ferry and J. Bird, *Wave function scarring effects in open stadium shaped quantum dots*. Phys. Rev. Lett. **79**, 123 (1997).

[7] I. Aleiner and V. Fal'ko, *Spin-orbit coupling effects on quantum transport in lateral semiconductor dots*. Phys. Rev. Lett. **87**, 256801 (2001).

[8] Y. Alhassid, *The statistical theory of quantum dots*. Rev. Mod. Phys. **72**, 895 (2000).

[9] B. Altshuler, A. Aronov and D. Khmelnitsky, *Effects of electron-electron collisions with small energy transfers on quantum localisation*. J. Phys. C: Solid State Phys. **15**, 7367 (1982).

[10] B. Altshuler, A. Aronov and P. Lee, *Interaction Effects in Disordered Fermi Systems in Two Dimensions*. Phys. Rev. Lett. **44**, 1288 (1980).

[11] B. Altshuler, D. Khmel'nitzkii, A. Larkin and P. Lee, *Magnetoresistance and Hall effect in a disordered two-dimensional electron gas*. Phys. Rev. B **22**, 5142 (1980).

[12] T. Ando, A. Fowler and F. Stern, *Electronic Properties of Two-Dimensional Systems*. Rev. Mod. Phys. **54**, 437 (1982).

[13] N. Averkiev, L. Golub and G. Pikus, *Anomalous magnetoresistance in p-type quantum wells*. Solid. State Commun. **107**, 757 (1998).

[14] D. Awschalom, D. Loss and N. Samarth [editors], *Semiconductor Spintronics and Quantum Computation*, (Springer-Verlag, Berlin Heidelberg New York, 2002).

[15] H. Baranger, R. Jalabert and A. Stone, *Weak Localization and Integrability in Ballistic Cavities*. Phys. Rev. Lett. **70**, 3876 (1993).

[16] H. Baranger and P. Mello, *Effect of Phase Breaking on Quantum Transport through Chaotic Cavities*. Phys. Rev. Lett. **51**, 4703 (1995).

[17] W. Bauer and G. Bertsch, *Decay of Ordered and Chaotic Systems*. Phys. Rev. Lett. **65**, 2213 (1990).

[18] V. Bayot, E. Grivei, H. Manoharan, X. Ying and M. Shayegan, *Thermopower of Composite Fermions*. Phys. Rev. B **52**, R8621 (1995).

[19] V. Bayot, X. Ying, M. Santos and M. Shayegan, *Thermopower in the Reentrant Insulating Phase of a Two-Dimensional Hole System*. Europhys. Lett. **25**, 613 (1994).

[20] C. Beenakker, *Random-matrix theory of quantum transport*. Rev. Mod. Phys. **69**, 731 (1997).

[21] G. Bergmann, *Influence of Spin-Orbit Coupling on Weak Localization*. Phys. Rev. Lett. **48**, 1046 (1982).

[22] G. Bergmann, *Weak anti-localization - An experimental proof for the destructive interference of rotated spin 1/2*. Solid State Commun. **42**, 815 (1982).

[23] G. Bergmann, *Physical interpretation of weak localization: A time-of-flight experiment with conduction electrons*. Phys. Rev. B **28**, 2914 (1983).

[24] J. Bird, K. Ishibashi, D. Ferry, Y. Ochiai, Y. Aoyagi and T. Sugano, *Phase Breaking in Ballistic Quantum Dots: Transition from Two-Dimensional to Zero-Dimensional Behavior*. Phys. Rev. B **51**, 18037 (1995).

[25] J. Bird, K. Ishibashi, M. Stopa, Y. Aoyagi and T. Sugano, *Coulomb-Blockade of the Aharonov-Bohm Effect in $GaAs/Al_xGa_{1-x}As$ Quantum Dots*. Phys. Rev. B **50**, 14983 (1994).

[26] J. Bird, A. Micolich, H. Linke, D. Ferry, R. Akis, Y. Ochiai, Y. Aoyagi and T. Sugano, *Environmental coupling and phase breaking in open quantum dots*. J. Phys. Condens. Matter **10**, L55 (1998).

[27] J. Bird, D. Olatona, R. Newbury, R. Taylor, K. Ishibashi, M. Stopa, Y. Aoyagi, T. Sugano and Y. Ochiai, *Lead-Induced Transition to Chaos in Ballistic Mesoscopic Billiards*. Phys. Rev. B **52**, 14336 (1995).

[28] D. Bishop, D. Tsui and R. Dynes, *Non-Metallic Conduction in Electron Inversion-Layers at Low-Temperatures*. Phys. Rev. Lett. **44**, 1153 (1980).

[29] L. Brey, H. Fertig, R. Cote and A. Macdonald, *Skyrme Crystal in a Two-Dimensional Electron Gas*. Phys. Rev. Lett. **75**, 2562 (1995).

[30] P. Brouwer and C. Beenakker, *Voltage-probe and imaginary-potential models for dephasing in a chaotic quantum dot*. Phys. Rev. B **55**, 4695 (1997).

[31] P. Brouwer and C. Beenakker, *Erratum: Voltage-probe and imaginary-potential models for dephasing in a chaotic quantum dot [Phys. Rev. B 55, 004695 (1997)]*. Phys. Rev. B **66**, 209901(E) (2002).

[32] P. Brouwer, J. Cremers and B. Halperin, *Weak localization and conductance fluctuations of a chaotic quantum dot with tunable spin-orbit coupling*. Phys. Rev. B **65**, 081302(R) (2002).

[33] L. Bürgi, N. Knorr, H. Brune, M. Schneider and K. Kern, *Two-dimensional electron gas at noble-metal surfaces*. Appl. Phys. A **75**, 141 (2002).

[34] M. Burns and P. Chaikin, *Interaction effects and thermoelectric power in low-temperature hopping*. J. Phys. C: Solid State Phys. **18**, L743 (1985).

[35] P. Butcher, N. March and M. Tosi [editors], *Physics of Low-Dimensional Semiconductor Structures*, (Plenum Press, New York and London, 1993).

[36] P.M. Chaikin in *Organic superconductivity*, edited by V.Z. Kresin and W.A. Little, (Plenum Press, New York, 1990).

[37] A. Chang, H. Baranger, L. Pfeiffer and K. West, *Weak-Localization in Chaotic Versus Nonchaotic Cavities: a Striking Difference in the Line-Shape*. Phys. Rev. Lett. **73**, 2111 (1994).

[38] A. Cho, *Growth of Periodic Structures by the Molecular-Beam Method*. Appl. Phys. Lett. **19**, 467 (1971).

[39] K. Choi, D. Tsui and K. Alavi, *Dephasing Time and One-Dimensional Localization of Two-Dimensional Electrons in $GaAs/Al_xGa_{1-x}As$ Heterostructures*. Phys. Rev. B **36**, 7751 (1987).

[40] R. Clarke, I. Chan, C. Marcus, C. Duruoz, J. Harris, K. Campman and A. Gossard, *Temperature-Dependence of Phase Breaking in Ballistic Quantum Dots*. Phys. Rev. B **52**, 2656 (1995).

[41] B. Cole, J. Chamberlain, M. Henini, T. Cheng, W. Batty, A. Wittlin, J. Perenboom, A. Ardavan, A. Polisski and J. Singleton, *Cyclotron resonance in ultra-low-hole-density narrow p-type $GaAs/(Al,Ga)As$ quantum wells*. Phys. Rev. B **55**, 2503 (1997).

[42] P. Coleridge, R. Williams, Y. Feng and P. Zawadzki, *Metal-insulator transition at $B = 0$ in p-type SiGe*. Phys. Rev. B **56**, 12764 (1997).

[43] J.-H. Cremers, P. Brouwer and V. Fal'ko, *Weak localization and conductance fluctuations in a quantum dot with parallel magnetic field and spin-orbit scattering*. Phys. Rev. B **68**, 125329 (2003).

[44] R. Crook, C. Smith, A. Graham, I. Farrer, H. Beere and D. Ritchie, *Imaging fractal conductance fluctuations and scarred wave functions in a quantum billiard*. Phys. Rev. Lett. **91**, 246803 (2003).

[45] M. Cutler and N. Mott, *Observation of Anderson Localization in an Electron Gas*. Phys. Rev. **181**, 1336 (1969).

[46] S. Das Sarma and E. Hwang, *Parallel magnetic field induced giant magnetoresistance in low density quasi-two-dimensional layers*. Phys. Rev. Lett. **84**, 5596 (2000).

[47] S. Das Sarma and E. Hwang, *Similarities and differences in two-dimensional metallicity induced by temperature and a parallel magnetic field: Effect of screening*. Phys. Rev. B **72**, 035311 (2005).

[48] S. Das Sarma and E. Hwang, *The so-called two dimensional metal-insulator transition*. Solid State Commun. **135**, 579 (2005).

[49] S. Das Sarma and A. Pinczuk [editors], *Perspectives in quantum Hall effects: novel quantum liquids in low-dimensional semiconductor structures*, (Wiley, New York, 1997).

[50] S. Datta, *Electronic Transport in Mesoscopic Systems*, (Cambridge University Press, Cambridge, 1997).

[51] J. Davies, *The Physics of Low-dimensional Semiconductors*, (Cambridge University Press, Cambridge, 1997).

[52] R. Dingle, H. Stormer and A. Gossard, *Electron mobilities in modulation-doped semiconductor heterojunction superlattices*. Appl. Phys. Lett. **33**, 665 (1978).

[53] M. Dresselhaus, G. Chen, M. Tang, R. Yang, H. Lee, D. Wang, Z. Ren, J. Fleurial and P. Gogna, *New directions for low-dimensional thermoelectric materials*. Adv. Mater. **19**, 1043 (2007).

[54] S.C. Dultz and H.W. Jiang, *Thermodynamic Signature of a Two-Dimensional Metal-Insulator Transition*. Phys. Rev. Lett. **84**, 4689 (2000).

[55] K. Efetov, *Temperature Effects in Quantum Dots in the Regime of Chaotic Dynamics*. Phys. Rev. Lett. **74**, 2299 (1995).

[56] E. Eisenberg, K. Held and B. Altshuler, *Dephasing times in closed quantum dots*. Phys. Rev. Lett. **88**, 136801 (2002).

[57] J. Eisenstein and A. MacDonald, *Bose-Einstein condensation of excitons in bilayer electron systems*. Nature **432**, 691 (2004).

[58] J.P. Eisenstein, L.N. Pfeiffer and K.W. West, *Compressibility of the two-dimensional electron gas: Measurements of the zero-field exchange energy and fractional quantum Hall gap*. Phys. Rev. B **50**, 1760 (1994).

[59] M. Elhassan, J. Bird, R. Akis, D. Ferry, T. Ida and K. Ishibashi, *Dephasing due to coupling to the external environment in open quantum-dot arrays*. J. Phys. Condens. Matter **17**, L351 (2005).

[60] K. Esfarjani, S. Chui and X. Qiu, *Dislocation Waves in a Two-Dimensional Coulomb Lattice*. Phys. Rev. B **46**, 4638 (1992).

[61] A. Facchetti, M. Yoon and T. Marks, *Gate dielectrics for organic field-effect transistors: New opportunities for organic electronics*. Adv. Mater. **17**, 1705 (2005).

[62] S. Faniel, B. Hackens, A. Vlad, L. Moldovan, C. Gustin, B. Habib, S. Melinte, M. Shayegan and V. Bayot, *Dephasing time of two-dimensional holes in GaAs open quantum dots: Magnetotransport measurements*. Phys. Rev. B **75**, 193310 (2007).

[63] S. Faniel, L. Moldovan, A. Vlad, E. Tutuc, N. Bishop, S. Melinte, M. Shayegan and V. Bayot, *In-plane magnetic-field-induced metal-insulator transition in (311)A GaAs two-dimensional hole systems probed by thermopower*. Phys. Rev. B **76**, 161307(R) (2007).

[64] S. Faniel, E. Tutuc, E. De Poortere, C. Gustin, A. Vlad, S. Melinte, M. Shayegan and V. Bayot, *Thermopower of interacting GaAs bilayer hole systems in the reentrant insulating phase near $\nu = 1$*. Phys. Rev. Lett. **94**, 046802 (2005).

[65] S. Faniel, E. Tutuc, E. De Poortere, C. Gustin, A. Vlad, L. Moldovan, S. Melinte, M. Shayegan and V. Bayot, *Thermopower evidence for Wigner crystallization in the insulating phase of two-dimensional GaAs bilayer hole systems*. Physica E **34**, 120 (2006).

[66] R. Fletcher, *Magnetothermoelectric effects in semiconductor systems*. Semicond. Sci. Technol. **14**, R1 (1999).

[67] R. Fletcher, J.C. Mann, K. Ploog, G. Weimann, *Thermoelectric properties of $GaAs-Ga_{1-x}Al_xAs$ heterojunctions at high magnetic fields*. Phys. Rev. B. **33**, 7122 (1986).

[68] R. Fletcher, V. Pudalov, Y. Feng, M. Tsaousidou, P.N. Butcher, *Thermoelectric and hot-electron properties of a silicon inversion layer*. Phys. Rev. B. **56**, 12422 (1997).

[69] R. Fletcher, V. Pudalov, A. Radcliffe and C. Possanzini, *Critical behaviour of thermopower and conductivity at the metal-insulator transition in high-mobility Si-MOSFETs*. Semicond. Sci. Technol. **16**, 386 (2001).

[70] R. Fletcher, M. Tsaousidou, P. Coleridge, Y. Feng and Z. Wasilewski, *Electron-phonon coupling and phonon-drag thermopower of a very low mobility 2DEG*. Physica E **12**, 478 (2002).

[71] J. Folk, S. Patel, K. Birnbaum, C. Marcus, C. Duruoz and J. Harris, *Spin degeneracy and conductance fluctuations in open quantum dots*. Phys. Rev. Lett. **86**, 2102 (2001).

[72] K. Frahm, *Crossover of Magnetoconductance Autocorrelation for a Ballistic Chaotic Quantum Dot*. Europhys. Lett. **30**, 457 (1995).

[73] H. Fukuyama and E. Abrahams, *Inelastic scattering time in two-dimensional disordered metals*. Phys. Rev. B **27**, 5976 (1983).

[74] B. Gallagher and P. Butcher in *Handbook on Semiconductors*, edited by P.T. Landsberg, (North-Holland, Amsterdam New York, 1992).

[75] B. Gallagher, J. Oxley, T. Galloway, M. Smith and P. Butcher, *The Phonon Drag and Diffusion Thermopower of Si Inversion-Layers*. J. Phys. Condens. Matter **2**, 755 (1990).

[76] S. Ilani, A. Yacobi, D. Mahalu and H. Shtrikman, *Unexpected Behavior of the local Compressibility near the $B = 0$ Metal-Insulator Transition*. Phys. Rev. Lett. **84**, 3133 (2000).

[77] S. Ilani, A. Yacobi, D. Mahalu and H. Shtrikman, *Microscopic Structure of the Metal-Insulator transition in Two Dimensions*. Science **292**, 1354 (2001).

[78] M. Gerl and J. Issi, *Traité des matériaux, vol 8: Physique des matériaux*, (Presses Polytechniques Romandes, Lausanne, 1997).

[79] M. Gershenson, V. Podzorov and A. Morpurgo, *Colloquium: Electronic transport in single-crystal organic transistors*. Rev. Mod. Phys. **78**, 973 (2006).

[80] A. Gold and V. Dolgopolov, *Temperature dependence of the conductivity for the two-dimensional electron gas: Analytical results for low temperatures*. Phys. Rev. B **33**, 1076 (1986).

[81] V. Goldman, M. Santos, M. Shayegan and J. Cunningham, *Evidence for Two-Dimensional Quantum Wigner Crystal*. Phys. Rev. Lett. **65**, 2189 (1990).

[82] B. Grbic, R. Leturcq, K. Ensslin, D. Reuter and A. Wieck, *Single-hole transistor in p-type GaAs/AlGaAs heterostructures*. Appl. Phys. Lett. **87**, 232108 (2005).

[83] C. Grimes, *Electrons in surface states on liquid helium*. Surf. Sci. **73**, 379 (1978).

[84] C. Gustin, S. Faniel, B. Hackens, S. Melinte, M. Shayegan and V. Bayot, *Orbital effect, subband depopulation, and conductance fluctuations in ballistic quantum dots under a tilted magnetic field*. Phys. Rev. B **71**, 155314 (2005).

[85] B. Hackens, F. Delfosse, S. Faniel, C. Gustin, H. Boutry, X. Wallart, S. Bollaert, A. Cappy and V. Bayot, *Long dephasing time and high-temperature conductance fluctuations in an open InGaAs quantum dot*. Phys. Rev. B **66**, 241305(R) (2002).

[86] B. Hackens, S. Faniel, C. Gustin, X. Wallart, S. Bollaert, A. Cappy and V. Bayot, *Dwell-time-limited coherence in open quantum dots*. Phys. Rev. Lett. **94**, 146802 (2005).

[87] B. Halperin, P. Lee and N. Read, *Theory of the Half-Filled Landau-Level*. Phys. Rev. B **47**, 7312 (1993).

[88] B. Halperin, A. Stern, Y. Oreg, J. Cremers, J. Folk and C. Marcus, *Spin-orbit effects in a GaAs quantum dot in a parallel magnetic field*. Phys. Rev. Lett. **86**, 2106 (2001).

[89] Y. Hanein, U. Meirav, D. Shahar, C. C. Li, D. Tsui and H. Shtrikman, *The metalliclike conductivity of a two-dimensional hole system*. Phys. Rev. Lett. **80**, 1288 (1998).

[90] Y. Hanein, D. Shahar, J. Yoon, C. Li, D. Tsui and H. Shtrikman, *Observation of the metal-insulator transition in two-dimensional n-type GaAs*. Phys. Rev. B **58**, R13338 (1998).

[91] J. Heremans, M. Santos, K. Hirakawa and M. Shayegan, *Mobility Anisotropy of Two-Dimensional Hole Systems in (311)A $GaAs/Al_xGa_{1-x}As$ Heterojunctions*. J. Appl. Phys. **76**, 1980 (1994).

[92] J. J. Heremans, *Transverse Magnetic Focusing in Two-Dimernsional Systems at GaAs/AlGaAs Heterojunctions*. Ph.D. Thesis, Princeton University (1994).

[93] S. Hikami, A. Larkin and Y. Nagaoka, *Spin-Orbit Interaction and Magnetoresistance in the Two Dimensional Random System*. Prog. Theor. Phys. **63**, 707 (1979).

[94] K. Hirakawa, Y. Zhao, M. Santos, M. Shayegan and D. Tsui, *Anomalous Cyclotron-Resonance Line Splitting of Two-Dimensional Holes in (311)a $Al_xGa_{1-x}As/GaAs$ Heterojunctions*. Phys. Rev. B **47**, 4076 (1993).

[95] J. Huang, J. Xia, D. Tsui, L. Pfeiffer and K. West, *Disappearance of metal-like behavior in GaAs two-dimensional holes below 30 mK*. Phys. Rev. Lett. **98**, 226801 (2007).

[96] A. Huibers, *Electron Transport and Dephasing in Semiconductor Quantum dots*. Ph.D. Thesis, Standford University (1999).

[97] A. Huibers, J. Folk, S. Patel, C. Marcus, C. Duruoz and J. Harris, *Low-temperature saturation of the dephasing time and effects of microwave radiation on open quantum dots*. Phys. Rev. Lett. **83**, 5090 (1999).

[98] A. Huibers, M. Switkes, C. Marcus, K. Campman and A. Gossard, *Dephasing in open quantum dots*. Phys. Rev. Lett. **81**, 200 (1998).

[99] R. Hyndman, T. Ihn, B. Gallagher, P. Rodgers, M. Henini, T. Foster and J. Middleton, *Observation of correlated $\nu = 1$ quantum Hall and insulating states in strongly coupled p-type double quantum wells*. Surf. Sci. **362**, 117 (1996).

[100] R. Hyndman, S. Stoddart, B. Tieke, S. Lok, B. Gallagher, A. Geim, J. Maan and M. Henini, *Magnetothermopower of double p-type quantum wells*. Physica B (Amsterdam) **249-251**, 745 (1998).

[101] J. Jain, *Composite-Fermion Approach for the Fractional Quantum Hall-Effect*. Phys. Rev. Lett. **63**, 199 (1989).

[102] R. Jalabert, H. Baranger and A. Stone, *Conductance Fluctuations in the Ballistic Regime - a Probe of Quantum Chaos*. Phys. Rev. Lett. **65**, 2442 (1990).

[103] R. Jensen, *Chaotic scattering, unstable periodic orbits, and fluctuations in quantum transport*. Chaos **1**, 101 (1991).

[104] H. Jiang, R. Willett, H. Stormer, D. Tsui, L. Pfeiffer and K. West, *Quantum Liquid Versus Electron Solid around $\nu = 1/5$ Landau-Level Filling*. Phys. Rev. Lett. **65**, 633 (1990).

[105] C. Joachim, J. Gimzewski and A. Aviram, *Electronics using hybrid-molecular and mono-molecular devices*. Nature **408**, 541 (2000).

[106] C. Joachim and M. Ratner, *Molecular electronics: Some views on transport junctions and beyond*. Proc. Natl Acad. Sci. **102**, 8801 (2005).

[107] C. Jones, A. Usher, T. Cheng and C. Foxon, *Contactless detection of current breakdown of the quantum Hall effect*. Solid State Commun. **97**, 763 (1996).

[108] T. Jungwirth and A. MacDonald, *Pseudospin anisotropy classification of quantum Hall ferromagnets*. Phys. Rev. B **63**, 035305 (2001).

[109] M. Kellogg, J. Eisenstein, L. Pfeiffer and K. West, *Bilayer quantum hall systems at $\nu_T = 1$: Coulomb drag and the transition from weak to strong interlayer coupling*. Phys. Rev. Lett. **90**, 246801 (2003).

[110] M. Kellogg, J. Eisenstein, L. Pfeiffer and K. West, *Vanishing Hall resistance at high magnetic field in a double-layer two-dimensional electron system*. Phys. Rev. Lett. **93**, 036801 (2004).

[111] M. Kellogg, I. Spielman, J. Eisenstein, L. Pfeiffer and K. West, *Observation of quantized hall drag in a strongly correlated bilayer electron system*. Phys. Rev. Lett. **88**, 126804 (2002).

[112] W. Knap, C. Skierbiszewski, A. Zduniak, E. LitwinStaszewska, D. Bertho, F. Kobbi, J. Robert, G. Pikus, F. Pikus, S. V. Iordanskii, V. Mosser, K. Zekentes *et al.*, *Weak antilocalization and spin precession in quantum wells*. Phys. Rev. B **53**, 3912 (1996).

[113] S. Kravchenko, G. Kravchenko, J. Furneaux, V. Pudalov and M. D'Iorio, *Possible Metal-Insulator-Transition at $B = 0$ in Two Dimensions*. Phys. Rev. B **50**, 8039 (1994).

[114] S. Kravchenko and M. Sarachik, *Metal-insulator transition in two-dimensional electron systems*. Rep. Prog. Phys. **67**, 1 (2004).

[115] K. Lai, W. Pan, D. Tsui, S. Lyon, M. Mühlberger and F. Schäffler, *Two-dimensional metal-insulator transition and in-plane magnetoresistance in a high-mobility strained Si quantum well*. Phys. Rev. B **72**, 081313(R) (2005).

[116] Y. Lai, R. Blumel, E. Ott and C. Grebogi, *Quantum Manifestations of Chaotic Scattering*. Phys. Rev. Lett. **68**, 3491 (1992).

[117] R. Laughlin, *Anomalous Quantum Hall Effect - an Incompressible Quantum Fluid with Fractionally Charged Excitations*. Phys. Rev. Lett. **50**, 1395 (1983).

[118] P. Lee and T. Ramakrishnan, *Disordered electronic systems*. Rev. Mod. Phys. **57**, 287 (1985).

[119] M. Lilly, J. Reno, J. Simmons, I. Spielman, J. Eisenstein, L. Pfeiffer, K. West, E. Hwang and S. Das Sarma, *Resistivity of dilute 2D electrons in an undoped GaAs heterostructure*. Phys. Rev. Lett. **90**, 056806 (2003).

[120] J. Lin and J. Bird, *Recent experimental studies of electron dephasing in metal and semiconductor mesoscopic structures*. J. Phys. Condens. Matter **14**, R501 (2002).

[121] J. Lu, M. Shayegan, L. Wissinger, U. Rössler and R. Winkler, *Spin-resolved commensurability oscillations*. Phys. Rev. B **60**, 13776 (1999).

[122] J. Lu, J. Yau, S. Shukla, M. Shayegan, L. Wissinger, U. Rössler and R. Winkler, *Tunable spin-splitting and spin-resolved ballistic transport in GaAs/AlGaAs two-dimensional holes*. Phys. Rev. Lett. **81**, 1282 (1998).

[123] Y. Lyanda-Geller, *Quantum interference and electron-electron interactions at strong spin-orbit coupling in disordered systems*. Phys. Rev. Lett. **80**, 4273 (1998).

[124] S. Lyo, *Low-Temperature Phonon-Drag Thermoelectric-Power in Heterojunctions*. Phys. Rev. B **38**, R6345 (1988).

[125] S. Lyo, *Anomalous thermopower of a quasi-two-dimensional low-density metallic hole gas*. Phys. Rev. B **70**, 153301 (2004).

[126] H. Manoharan, Y. Suen, M. Santos and M. Shayegan, *Evidence for a bilayer quantum Wigner solid*. Phys. Rev. Lett. **77**, 1813 (1996).

[127] H. C. Manoharan, *New Particles and Phases in Reduced-Dimensional Systems*. Ph.D. Thesis, Princeton University (1998).

[128] C. Marcus, S. Patel, A. Huibers, S. Cronenwett, M. Switkes, I. Chan, R. Clarke, J. Folk, S. Godijn, K. Campman and A. Gossard, *Quantum chaos in open versus closed quantum dots: Signatures of interacting particles*. Chaos, Solitons & Fractals **8**, 1261 (1997).

[129] C. Marcus, A. Rimberg, R. Westervelt, P. Hopkins and A. Gossard, *Conductance Fluctuations and Chaotic Scattering in Ballistic Microstructures*. Phys. Rev. Lett. **69**, 506 (1992).

[130] C. Marcus, R. Westervelt, P. Hopkins and A. Gossard, *Phase Breaking in Ballistic Quantum Dots - Experiment and Analysis Based on Chaotic Scattering*. Phys. Rev. B **48**, 2460 (1993).

[131] A. Matthews, K. Kavokin, A. Usher, M. Portnoi, M. Zhu, J. Gething, M. Elliott, W. Herrenden-Harker, K. Phillips, D. Ritchie, M. Simmons, C. Sorensen *et al.*, *Temperature dependence of the breakdown of the quantum Hall effect studied by induced currents*. Phys. Rev. B **70**, 075317 (2004).

[132] S. McPhail, C. Yasin, A. Hamilton, M. Simmons, E. Linfield, M. Pepper and D. Ritchie, *Weak localization in high-quality two-dimensional systems*. Phys. Rev. B **70**, 245311 (2004).

[133] M.L. Mehta, *Random Matrices*, (Academic, New York, 1991).

[134] J. Miller, D. Zumbuhl, C. Marcus, Y. Lyanda-Geller, D. Goldhaber-Gordon, K. Campman and A. Gossard, *Gate-controlled spin-orbit quantum interference effects in lateral transport*. Phys. Rev. Lett. **90**, 076807 (2003).

[135] G. Minkov, A. Sherstobitov, A. Germanenko, O. Rut, V. Larionova and B. Zvonkov, *Antilocalization and spin-orbit coupling in the hole gas in strained $GaAs/In_xGa_{1-x}As/GaAs$ quantum well heterostructures*. Phys. Rev. B **71**, 165312 (2005).

[136] A. Mittal, R. Wheeler, M. Keller, D. Prober and R. Sacks, *Electron-phonon scattering rates in GaAs/AlGaAs 2DEG samples below 0.5 K*. Surf. Sci. **362**, 537 (1996).

[137] L. Moldovan, S. Melinte, V. Bayot, S. Papadakis, E. De Poortere and M. Shayegan, *Anomalous thermopower in the metalliclike phase of a 2D hole system*. Phys. Rev. Lett. **85**, 4369 (2000).

[138] K. Moon, H. Mori, K. Yang, S. Girvin, A. Macdonald, L. Zheng, D. Yoshioka and S. Zhang, *Spontaneous Interlayer Coherence in Double-Layer Quantum Hall Systems - Charged Vortices and Kosterlitz-Thouless Phase-Transitions*. Phys. Rev. B **51**, 5138 (1995).

[139] S. Murphy, J. Eisenstein, G. Boebinger, L. Pfeiffer and K. West, *Many-Body Integer Quantum Hall-Effect - Evidence for New Phase-Transitions*. Phys. Rev. Lett. **72**, 728 (1994).

[140] K. Nakamura, D. Tsui, F. Nihey, H. Toyoshima and T. Itoh, *Electron Focusing with Multiparallel One-Dimensional Channels Made by Focused Ion-Beam*. Appl. Phys. Lett. **56**, 385 (1990).

[141] F. Nihey, K. Nakamura, M. Kuzuhara, N. Samoto and T. Itoh, *Electron Focusing with Multiparallel GaAs-AlGaAs Wires Defined by Damageless Processing*. Appl. Phys. Lett. **57**, 1218 (1990).

[142] G. Nolas, J. Sharp and H. Goldsmid, *Thermoelectrics - Basic Principles and New Materials Developments*, (Springer-Verlag, Berlin Heidelberg, 2001).

[143] R. Nötzel, N. Ledentsov, L. Daweritz, K. Ploog and M. Hohenstein, *Semiconductor Quantum-Wire Structures Directly Grown on High-Index Surfaces*. Phys. Rev. B **45**, 3507 (1992).

[144] K. Novoselov, A. K. Geim, S. Morozov, D. Jiang, M. Katsnelson, I. Grigorieva, S. Dubonos and A. Firsov, *Two-Dimensional Gas of Massless Dirac Fermions in Graphene*. Nature **438**, 197 (2005).

[145] K. Novoselov, D. Jiang, F. Schedin, T. Booth, V. Khotkevich, S. Morozov and A. K. Geim, *Two Dimensional Atomic Crystals*. Proc. Natl Acad. Sci. **102**, 10451 (2005).

[146] M. Paalanen, R. Willett, R. Ruel, P. Littlewood, K. West and L. Pfeiffer, *Electrical-Conductivity and Wigner Crystallization*. Phys. Rev. B **45**, R13784 (1992).

[147] W. Pan, K. Lai, S. Bayrakci, N. Ong, D. Tsui, L. Pfeiffer and K. West, *Cyclotron resonance at microwave frequencies in two-dimensional hole system in AlGaAs/GaAs quantum wells*. Appl. Phys. Lett. **83**, 3519 (2003).

[148] S. Papadakis, E. De Poortere, H. Manoharan, M. Shayegan and R. Winkler, *The effect of spin splitting on the metallic behavior of a two-dimensional system*. Science **283**, 2056 (1999).

[149] S. Papadakis, E. De Poortere, H. Manoharan, J. Yau, M. Shayegan and S. Lyon, *Low-field magnetoresistance in GaAs two-dimensional holes*. Phys. Rev. B **65**, 245312 (2002).

[150] S. Papadakis, E. De Poortere, M. Shayegan and R. Winkler, *Anisotropic magnetoresistance of two-dimensional holes in GaAs*. Phys. Rev. Lett. **84**, 5592 (2000).

[151] S. Papadakis and M. Shayegan, *Apparent metallic behavior at $B = 0$ of a two-dimensional electron system in AlAs*. Phys. Rev. B **57**, R15068 (1998).

[152] S. Pedersen, C. Sørensen, A. Kristensen, P. Lindelof, L. Golub and N. Averkiev, *Weak localization in $Al_{0.5}Ga_{0.5}As/GaAs$ p-type quantum wells*. Phys. Rev. B **60**, 4880 (1999).

[153] M. Pioro-Ladrière, J. Davies, A. Long, A. Sachrajda, L. Gaudreau, P. Zawadzki, J. Lapointe, J. Gupta, Z. Wasilewski and S. Studenikin, *Origin of switching noise in $GaAs/Al_xGa_{1-x}As$ lateral gated devices*. Phys. Rev. B **72**, 115331 (2005).

[154] M. Pioro-Ladrière, A. Usher, A. Sachrajda, M. Elliott, J. Lapointe, J. Gupta, Z. Wasilewski and S. Studenikin, *Hysteretic effects in lateral nanostructures caused by long-lived quantum-Hall eddy currents*. Physica E **34**, 476 (2006).

[155] M. Pioro-Ladrière, A. Usher, A. Sachrajda, J. Lapointe, J. Gupta, Z. Wasilewski, S. Studenikin and M. Elliott, *Influence of the long-lived quantum Hall potential on the characteristics of quantum devices*. Phys. Rev. B **73**, 075309 (2006).

[156] D. Pivin, A. Andersen, J. Bird and D. Ferry, *Saturation of phase breaking in an open ballistic quantum dot*. Phys. Rev. Lett. **82**, 4687 (1999).

[157] C.E. Porter, *Statistical Theories of Spectra: Fluctuations*, (Academic, New York, 1965).

[158] C. Possanzini, R. Fletcher, P. Coleridge, Y. Feng, R. Williams and J. Maan, *Diffusion thermopower of a two-dimensional hole gas in SiGe in a quantum Hall insulating state*. Phys. Rev. Lett. **90**, 176601 (2003).

[159] C. Possanzini, R. Fletcher, M. Tsaousidou, P. Coleridge, R. Williams, Y. Feng and J. Maan, *Thermopower of a p-type $Si/Si_{1-x}Ge_x$ heterostructure*. Phys. Rev. B **69**, 195306 (2004).

[160] R. Prange and S. Girvin [editors], *The Quantum Hall Effect*, (Springer-Verlag, New York Berlin Heidelberg, 1990).

[161] C. Prasad, D. Ferry, A. Shailos, M. Elhassan, J. Bird, L. Lin, N. Aoki, Y. Ochiai, K. Ishibashi and Y. Aoyagi, *Phase breaking and energy relaxation in open quantum-dot arrays*. Phys. Rev. B **62**, 15356 (2000).

[162] G. Prinz, *Spin-Polarized Transport*. Physics Today **48**, 58 (1995).

[163] Y. Proskuryakov, A. Savchenko, S. Safonov, M. Pepper, M. Simmons and D. Ritchie, *Fermi-liquid behavior of the low-density 2D hole gas in a GaAs/AlGaAs heterostructure at large values of* r_s. Phys. Rev. Lett. **86**, 4895 (2001).

[164] A. Punnoose and A. Finkel'stein, *Dilute electron gas near the metal-insulator transition: Role of valleys in silicon inversion layers*. Phys. Rev. Lett. **88**, 016802 (2002).

[165] P. Rai-Choudhury [editor], *Handbook of Microlithography, Micromachining and Microfabrication*, (SPIE Press Monograph & SPIE Optical Engineering Press, Bellingham London, 1997).

[166] R. Richardson and E. Smith [editors], *Experimental Techniques in Condensed Matter Physics at Low Temperatures*, (Addison-Wesley Publishing Company Inc., Redwood City, 1988).

[167] L. Rokhinson, V. Larkina, Y. Lyanda-Geller, L. Pfeiffer and K. West, *Spin separation in cyclotron motion*. Phys. Rev. Lett. **93**, 146601 (2004).

[168] D.M. Rowe [editor], *Thermoelectrics Handbook: Macro to Nano* (Taylor & Francis group, Boca Raton London New York, 2006).

[169] C. Ruf, M. Brummell, E. Gmelin and K. Ploog, *The Influence of Subband Structure on the Thermoelectric-Power of* $GaAs/Al_xGa_{1-x}As$ *Heterojunctions*. Superlattices Microstruct. **6**, 175 (1989).

[170] A. Salomon, D. Cahen, S. Lindsay, J. Tomfohr, V. Engelkes and C. Frisbie, *Comparison of electronic transport measurements on organic molecules*. Adv. Mater. **15**, 1881 (2003).

[171] M. Santos, Y. Suen, M. Shayegan, Y. Li, L. Engel and D. Tsui, *Observation of a Reentrant Insulating Phase near the 1/3 Fractional Quantum Hall Liquid in a Two-Dimensional Hole System*. Phys. Rev. Lett. **68**, 1188 (1992).

[172] J. Shah, A. Pinczuk, A. Gossard and W. Wiegmann, *Energy-Loss Rates for Hot Electrons and Holes in GaAs Quantum Wells*. Phys. Rev. Lett. **54**, 2045 (1985).

[173] A. Shashkin, *Metal-insulator transitions and the effects of electron-electron interactions in two-dimensional electron systems*. Physics-Uspekhi **48**, 129 (2005).

[174] A. Shashkin, S. Kravchenko, V. Dolgopolov and T. Klapwijk, *Sharp increase of the effective mass near the critical density in a metallic two-dimensional electron system*. Phys. Rev. B **66**, 073303 (2002).

[175] A. Shashkin, M. Rahimi, S. Anissimova, S. Kravchenko, V. Dolgopolov and T. Klapwijk, *Spin-independent origin of the strongly enhanced effective mass in a dilute 2D electron system*. Phys. Rev. Lett. **91**, 046403 (2003).

[176] M. Y. Simmons, A. Hamilton, M. Pepper, E. Linfield, P. Rose and D. Ritchie, *Weak localization, hole-hole interactions, and the "metal"-insulator transition in two dimensions*. Phys. Rev. Lett. **84**, 2489 (2000).

[177] D. Simonian, S. Kravchenko, M. Sarachik and V. Pudalov, *Magnetic field suppression of the conducting phase in two dimensions*. Phys. Rev. Lett. **79**, 2304 (1997).

[178] U. Sivan, Y. Imry and A. Aronov, *Quasi-Particle Lifetime in a Quantum-Dot*. Europhys. Lett. **28**, 115 (1994).

[179] J. Spector, H. Stormer, K. Baldwin, L. Pfeiffer and K. West, *Ballistic electron transport beyond 100 μm in 2D electron systems*. Suf. Sci. **228**, 283 (1990).

[180] I. Spielman, J. Eisenstein, L. Pfeiffer and K. West, *Resonantly enhanced tunneling in a double layer quantum Hall ferromagnet*. Phys. Rev. Lett. **84**, 5808 (2000).

[181] Y. Takane, *Phase relaxation time in open chaotic billiards*. J. Phys. Soc. Jpn. **67**, 3003 (1998).

[182] B. Tanatar and D. Ceperley, *Ground-State of the Two-Dimensional Electron Gas*. Phys. Rev. B **39**, 5005 (1989).

[183] B. Tieke, R. Fletcher, U. Zeitler, M. Henini and J. Maan, *Thermopower measurements of the coupling of phonons to electrons and composite fermions*. Phys. Rev. B **58**, 2017 (1998).

[184] G. Timp, A. Chang, J. Cunningham, T. Chang, P. Mankiewich, R. Behringer and R. Howard, *Observation of the Aharonov-Bohm Effect for $\omega_c\tau > 1$*. Phys. Rev. Lett. **58**, 2814 (1987).

[185] D. Tsui, H. Stormer and A. Gossard, *Two-Dimensional Magnetotransport in the Extreme Quantum Limit*. Phys. Rev. Lett. **48**, 1559 (1982).

[186] E. Tutuc, E. De Poortere, S. Papadakis and M. Shayegan, *In-plane magnetic field-induced spin polarization and transition to insulating behavior in two-dimensional hole systems*. Phys. Rev. Lett. **86**, 2858 (2001).

[187] E. Tutuc, S. Melinte, E. De Poortere, R. Pillarisetty and M. Shayegan, *Role of density imbalance in an interacting bilayer hole system*. Phys. Rev. Lett. **91**, 076802 (2003).

[188] E. Tutuc, S. Melinte, E. De Poortere, M. Shayegan and R. Winkler, *Role of finite layer thickness in spin polarization of GaAs two-dimensional electrons in strong parallel magnetic fields*. Phys. Rev. B **67**, 241309(R) (2003).

[189] E. Tutuc, M. Shayegan and D. Huse, *Counterflow measurements in strongly correlated GaAs hole bilayers: Evidence for electron-hole pairing*. Phys. Rev. Lett. **93**, 036802 (2004).

[190] H. van Houten, C. Beenakker, P. Vanloosdrecht, T. Thornton, H. Ahmed, M. Pepper, C. Foxon and J. Harris, *Four-Terminal Magnetoresistance of a Two-Dimensional Electron-Gas Constriction in the Ballistic Regime*. Phys. Rev. B **37**, R8534 (1988).

[191] H. van Houten, C. Beenakker, J. Williamson, M. Broekaart, P. Vanloosdrecht, B. van Wees, J. Mooij, C. Foxon and J. Harris, *Coherent electron focusing with quantum point contacts in a two-dimensional electron gas*. Phys. Rev. B **39**, 8556 (1989).

[192] B. van Wees, L. Kouwenhoven, E. Willems, C. Harmans, J. Mooij, H. Vanhouten, C. Beenakker, J. Williamson and C. Foxon, *Quantum Ballistic and Adiabatic Electron-Transport Studied with Quantum Point Contacts*. Phys. Rev. B **43**, 12431 (1991).

[193] B. van Wees, H. van Houten, C. Beenakker, J. Williamson, L. Kouwenhoven, D. Vandermarel and C. Foxon, *Quantized Conductance of Point Contacts in a Two-Dimensional Electron-Gas*. Phys. Rev. Lett. **60**, 848 (1988).

[194] S. Vitkalov, H. Zheng, K. Mertes, M. Sarachik and T. Klapwijk, *Small-angle Shubnikov-de Haas measurements in a 2D electron system: The effect of a strong in-plane magnetic field*. Phys. Rev. Lett. **85**, 2164 (2000).

[195] S. Washburn and R. Webb, *Aharonov-Bohm effect in normal metal quantum coherence and transport*. Adv. Phys. **35**, 375 (1986).

[196] S. Washburn and R. Webb, *Quantum Transport in Small Disordered Samples from the Diffusive to the Ballistic Regime*. Rep. Prog. Phys. **55**, 1311 (1992).

[197] M. Wassermeier, J. Sudijono, M. Johnson, K. Leung, B. Orr, L. Däweritz and K. Ploog, *Reconstruction of the GaAs (311)A Surface*. Phys. Rev. B **51**, 14721 (1995).

[198] A. Wennberg, S. Ytterboe, C. Gould, H. Bozler, J. Klem and H. Morkoç, *Eletron heating in a multiple-quantum-well structure below 1 K*. Phys. Rev. B **34**, 4409 (1986).

[199] R. Wiersma, J. Lok, S. Kraus, W. Dietsche, K. von Klitzing, D. Schuh, M. Bichler, H. Tranitz and W. Wegscheider, *Activated transport in the separate layers that form the $\nu_T = 1$ exciton condensate*. Phys. Rev. Lett. **93**, 266805 (2004).

[200] E. Wigner, *On the Interaction of Electrons in Metals*. Phys. Rev. **46**, 1002 (1934).

[201] R. Williams, *Modern GaAs Processing Methods*, (Artech House, Boston London, 1990).

[202] R. Winkler, *Spin-Orbit Coupling Effects in Two-Dimensional Electron and Hole Systems*, (Springer-Verlag, Berlin Heidelberg, 2003).

[203] R. Winkler, S. Papadakis, E. De Poortere and M. Shayegan, *Anomalous magneto-oscillations in two-dimensional systems*. Phys. Rev. Lett. **84**, 713 (2000).

[204] S. A. Wolf, D. Awschalom, R. Buhrman, J. Daughton, S. von Molnar, M. Roukes, A. Chtchelkanova and D. Treger, *Spintronics: A spin-based electronics vision for the future*. Science **294**, 1488 (2001).

[205] C. Yang, J. Carlson-Swindle, S. Lyon and J. Worlock, *Hot-Electron Relaxation in GaAs Quantum Wells*. Phys. Rev. Lett. **55**, 2359 (1985).

[206] J. Yau, E. De Poortere and M. Shayegan, *Aharonov-Bohm oscillations with spin: Evidence for Berry's phase*. Phys. Rev. Lett. **88**, 146801 (2002).

[207] D. Yoshioka, *The Quantum Hall Effect*, (Springer-Verlag, Berlin Heidelberg, 2002).

[208] I. Zailer, J. Frost, C. Ford, M. Pepper, M. Simmons, D. Ritchie, J. Nicholls and G. Jones, *Phase Coherence, Interference, and Conductance Quantization in a Confined Two-Dimensional Hole Gas*. Phys. Rev. B **49**, 5101 (1994).

[209] G. Zala, B. Narozhny and I. Aleiner, *Interaction corrections at intermediate temperatures: Magnetoresistance in a parallel field*. Phys. Rev. B **65**, 020201(R) (2001).

[210] J. Zaumseil and H. Sirringhaus, *Electron and ambipolar transport in organic field-effect transistors*. Chem. Rev. **107**, 1296 (2007).

[211] L. Zheng and S. Das Sarma, *Coulomb scattering lifetime of a two-dimensional electron gas*. Phys. Rev. B **53**, 9964 (1996).

[212] J. M. Ziman, *Electrons and phonons*, (Oxford University Press, Oxford, 1972).

[213] D. Zümbuhl, J. Miller, C. Marcus, K. Campman and A. Gossard, *Spin-orbit coupling, antilocalization, and parallel magnetic fields in quantum dots*. Phys. Rev. Lett. **89**, 276803 (2002).

[214] I. Zutic, J. Fabian and S. Das Sarma, *Spintronics: Fundamentals and applications*. Rev. Mod. Phys. **76**, 323 (2004).

[215] I.P. Zvyagin in *Hopping Transport in Solids*, edited by M. Pollak and B. I. Shklovskii, (North-Holland, Amsterdam, 1991).